A Numerical Study of a Droplet Evaporating in a Turbulent Airflow

By

Maher M. Abou Al-Sood

A DISSERTATION
Submitted to the Faculty of Graduate Studies
In partial fulfillment of the Requirements for the Degree of
DOCTOR OF PHILOSOPHY

Department of Mechanical and Manufacturing Engineering
The University of Manitoba
Winnipeg, Manitoba
Canada

THE UNIVERSITY OF MANITOBA

FACULTY OF GRADUATE STUDIES

*****

COPYRIGHT PERMISSION

A Numerical Study of a Droplet Evaporating in

A Turbulent Airflow

BY

Maher M. Abou Al-Sood

A Thesis/Practicum submitted to the Faculty of Graduate Studies of The University of

Manitoba in partial fulfillment of the requirement of the degree

DOCTOR OF PHILOSOPHY

To whom I love

Specially my family,

my wife and my daughter

TABLES OF CONTENTS

List of Figures.....V

List of Tables.....VIII

Nomenclature.....IX

Acknowledgements XII

Abstract..... XIII

Chapter 1. Motivations and Objectives..... 1

Chapter 2. Literature Review.....4

2.1 Effect of Turbulence on the Drag Coefficient of a Non-Evaporating Droplet..4
2.2 Effect of Turbulence on Droplet (or Sphere) Heat and Mass Transfer 7

Chapter 3. Problem Description and Mathematical Formulation 16

3.1 Description of the Physical Problem 16
3.2 Model Assumptions.....18
3.3 Governing Equations 19
3.3.1 Turbulent Flow over a Sphere..... 19
3.3.2 Turbulent Flow over an Evaporating Droplet.....20
3.3.2.1 Gas-Phase.....20
3.3.2.2 Liquid-Phase.....22
3.5 Turbulence Models 23
3.5.1 Zero-equation Models.....26
3.5.2 One-equation Model..... 27
3.5.3 Two-equation Model.....29
a. Standard k-ε Model..... 30
b. Low-Reynolds Number k-ε Models.....31
c. Low Reynolds number k-ω Model.....32
d. k-ω Baseline (BSL) Model..... 32
e. Shear stress transport (SST) Model.....34
3.6 Freestream and Gas-Liquid Interface Conditions 35
3.7 Wall Boundary Conditions..... 37

Chapter 4. Solution Algorithm.....39

4.1 Solution Approach.....39

4.2 Blocked-off Technique.....46
4.3 Treatment of a Droplet (or a Sphere) in the Calculation Domain..... 47
4.4 Solution Procedure.....48

Chapter 5. Results and Discussions.....54

5.1 Introduction.....54
5.2 Sphere Drag coefficient..... 55
5.2.1 Sphere Drag coefficient in a Laminar Flow.....56
5.2.2 Sphere Drag coefficient in a Turbulent Flow..... 59
5.3 Freestream Turbulence Effect on the Evaporation of a Droplet 64
5.3.1 Turbulence Effect under Standard Freestream Pressure and Temperature Conditions 66
5.3.2 Turbulence Effect in Hot Airstream Conditions..... 76

Chapter 6. Conclusions and Future Work..... 87

6.1 Conclusions.....87
6.2 Future Work.....89

References.....90

Appendix A. Discretization of the Governing Equations.....101

Appendix B. Solving Approach for a System of Algebraic Equations.....111

B.1 Point Successive Over Relaxation Method (SOR).....112
B.2 Line Successive Over Relaxation Method (LSOR).....113
B.3 Strongly Implicit Procedure (SIP).....114

Appendix C. Thermodynamic Properties.....118

Appendix D. Blocked-off Based Calculation of the Droplet's Volume and Surface Area 122

Appendix E. Evaporation Rate of *n*-heptane and *n*-decane Droplets 127

LIST OF FIGURES

2.1 Drag coefficient of a sphere (or a particle) in turbulent flows.....7

2.2 Turbulent droplet (or sphere) heat and mass transfer correlations.....9

2.3 Variation of the droplet turbulent evaporation rate normalized by its counterpart's laminar value versus the vaporization Damköhler number (Wu *et al.*, 2003).....14

3.1 Schematic of the physical problem; i.e., a droplet (or a sphere) exposed to freestream of air.....17

3.2 Time history of the droplet squared normalized diameter.....18

4.1 Central control volume P with its neighborhood control volumes.....42

4.2 Faces of the central control volume P.....43

4.3 Iterative procedure for solving both the gas-phase and liquid-phase governing equations.....45

4.4 The Cartesian-based blocked-off treatment of a spherical object (a droplet or a sphere) immersed in the computational domain.....51

4.5 Illustration of the computational domain and boundary conditions for a flow over a droplet (or a sphere).....52

4.6 Schematic diagram of the computational grid.....53

5.1 Comparison of the predicted local wall pressure coefficient against published numerical data for a typical Reynolds number.....57

5.2 Variation of the predicted wall pressure coefficient around the sphere for different Reynolds numbers.....58

5.3 Comparison of the predicted drag coefficient of a sphere exposed to a laminar freestream of air against its counterpart's experimental published data for various Reynolds numbers.....58

5.4 SST model based predictions of pressure coefficient contours in the x-y plane for Re=186 and I_∞ = 60%.....61

5.5 Variation of the local wall pressure coefficient around the sphere for various freestream turbulence intensities and a typical Reynolds number.....61

5.6 Variation of the laminar and turbulent (based on LRN k-ε model) predicted drag coefficient versus the freestream turbulence intensity for different Reynolds numbers.....62

5.7 Variation of the laminar and turbulent (based on Menter's SST model) predicted drag coefficient versus the freestream turbulence intensity for different Reynolds numbers.....62

5.8 Comparison of the sphere drag coefficient predicted by using different turbulence closure models against its counterpart experimental laminar "standard" drag in the Reynolds number range between 10 and 250.....63

5.9 Magnification of the comparison presented in Figure 5.9 for Reynolds number ranging between 10 and 100.....63

5.10 Time-history of n-heptane droplet's volume and evaporating surface area for typical test conditions.....66

5.11 Time-history of the squared normalized diameter for n-heptane droplet in a laminar flow.....67

5.12 Time-history of n-heptane and n-decane droplets surface temperature for different airstream turbulence intensities.....68

5.13 SST turbulence closure model based predictions of time-history of the squared normalized diameter of n-decane droplet 70

5.14 SST turbulence closure model based predictions of time-history of the squared normalized diameter of n-heptane droplet.....70

5.15 Variation of the evaporation rates of n-heptane and n-decane droplets versus freestream turbulence intensity.....71

5.16 SST model-based calculation of turbulent viscosity contours over a sphere for freestream mean-velocity of 2 m/s and turbulence intensity of 60%.....72

5.17 LRN k-ε model-based calculation of turbulent viscosity contours over a sphere for freestream mean-velocity of 2 m/s and turbulence intensity of 60%.....72

5.18 Normalized evaporation rate of n-heptane and n-decane droplets versus the vaporization Damköhler number.....75

5.19 Time-history of n-decane normalized squared diameter.....78

5.20 Time-history of the normalized squared diameter of *n*-heptane droplet at $T_\infty = 1273$ K and $U_\infty = 2$ m/s for various freestream turbulence intensities.....79

5.21 Time-history of the surface temperature for *n*-heptane and *n*-decane droplets at different turbulence intensities.....79

5.22 Normalized evaporation rate of *n*-heptane and *n*-decane droplets versus the freestream turbulence intensity at a typical freestream mean velocity $U_\infty = 2$ *m/s* and various freestream temperatures.....80

5.23 Vaporization Damköhler number versus the freestream temperature for typical turbulence intensities..... 81

5.24 Droplet evaporation characteristic time versus the freestream temperature for typical turbulence intensity.....82

5.25 Fuel mole and mass fractions versus the freestream temperature for various turbulence intensities..... 82

5.26 Predicted laminar Sherwood number for *n*-heptane and *n*-decane droplets versus Reynolds number for freestream temperature ranging between 300 K and 1273 K.....85

5.27 Predicted Sherwood number for *n*-heptane and *n*-decane droplets versus Re_M for different turbulence intensities.....85

5.28 Comparison of the predicted turbulent Sherwood number for *n*-heptane and *n*-decane droplets with the experimental data of Yearling (1995).....86

5.29 Yearling (1995) Laminar and turbulent Sherwood number data versus Reynolds number.....86

A.1 Mass flow through a typical control volume..... 101

D. 1 Simulated and real droplet surface as seen from top view (i.e., *x-z* planes).....122

D.2 Front view of the simulated droplet (i.e., *x-y* planes)..... 122

D.3 Control volumes and their corresponding surfaces for each plane of the droplet..... 124

LIST OF TABLES

2.1 Summary of published sphere (or droplet) heat and mass transfer correlations ...10

3.1 Length scale equations.....29

4.1 Summary of governing equations in terms of Φ, Γ_Φ and S_Φ..... 41

4.2 Grid sensitivity to the present model predictions..... 50

5.1 Test conditions.....64

C.1 Air properties at different temperatures.....120

D.1 Blocked-off technique based calculation of the control volumes and surfaces for each plane of the droplet.....125

E.1 Turbulent evaporation rates of *n*-heptane and *n*-decane droplets.....127

NOMENCLUTURE

ROMAN LETTERS

A	cross section area or evaporating surface area
$A^{'}, B^{'}$	constants
A_d	droplet surface area
B_M	mass transfer number
B_T	heat transfer number
C_p	pressure coefficient
C_D	drag coefficient
C_T	turbulence term in Eqs 2.1 and 2.2
C_μ	constant
d	diameter
D	diffusion conductance
D_{AB}	diffusion coefficient
Da_v	Damköhler number
D_m	molecular diffusivity
D_t	turbulence diffusivity of fuel vapor
f_t	weighting factor
f_μ	damping function
h_{evap}	latent heat of vaporization
I	turbulence intensity ($u^{'}/U_\infty$)
k	turbulence kinetic energy
K	evaporation rate
L	length of the computational domain
L_i	integral length scale
l_m	mixing length scale
M	molecular weight
$m^{''}_{evap}$	evaporated mass flux
$\dot{m}$	mass flow rate
Nu	Nusselt number
p	pressure
Pe	Peclet number
Pr	Prandtl number
q	turbulence kinetic energy in case of zero-mean velocity
r	radius
$\dot{r}$	regression rate of a spherical droplet radius
Re	Reynolds number
S_Φ	source term ($S_\Phi = S_C + S_P\Phi$)
Sc	Schmidt number
Sh	Sherwood number

T	temperature
t	time
T'	temperature fluctuation
T_t	turbulence time scale
T_v	vaporization time scale
U	mean-velocity component in x-direction
u'	fluctuation velocity component in x-direction
$\overline{u_i u_j}$	Reynolds stresses
V	mean-velocity component in y-direction
V	volume
V_d	droplet volume
V_r	vapor blowing velocity
V_t	turbulence velocity
W	mean-velocity component in z-direction
We	Weber number
x	coordinate
X_F	fuel mole fraction
Y_F'	fluctuation of fuel mass fraction
Y_F	fuel mass fraction

GREEK LETTERS

O	order of magnitude
X	an iteration parameter in the Stone's solver
ϕ	azimuthal angle
α	convection weighting factor
ρ	density (kg/m^3)
Φ	diffusion parameter (U, V, W, p,T,Y_F, k, ε and ω)
β	diffusion weighting factor
ω	dissipation per unit turbulence kinetic energy, ε / k
Γ	generalized diffusion coefficient
ν	kinematics viscosity
ν_t	eddy viscosity
μ	molecular viscosity
χ	relaxation factor
τ	shear stress
γ	surface tension
λ	thermal conductivity
ε	turbulence dissipation rate
μ	turbulence viscosity
σ_h	turbulence Prandtl number
σ_t	turbulence Schmidt number
δ_{ij}	Kronecker delta
δ_M	vapor film thickness

Δx control volume length in x-direction
Δy control volume length in y-direction
Δz control volume length in z-direction
δx distance between centers of two adjacent control volumes in direction of x-axis
δy distance between centers of two adjacent control volumes in direction of y-axis
δz distance between centers of two adjacent control volumes in direction of z-axis
Θ_{Φ} very small quantities, 10^{-4}

SUBSCRIPTS

∞ freestream value
0 initial, stagnant
a air
b bottom face of control volume
B bottom node
d droplet
E east node
e east face of control volume
eff effective
f film, friction
g ga-phase side
i x-, y-or z-coordinates if (i=1, 2, or 3)
L laminar
l liquid-phase side
M modified
m mixture
N north node
n north face of control volume
nor normal
P center node
p pressure
S south node
s south face of control volume, sphere, surface
T top node
t top face of control volume, turbulence
tan tangent
w west face of control volume, wall
W west node

ACKNOWLEDGEMENTS

I would like to thank all of those who supported me throughout the course of this thesis. First of all, I would like to express my sincere thanks and appreciations to my supervisor, Dr. Madjid Birouk, for his guidance of this work, stimulating suggestions and encouragements which made it possible to achieve the objectives of this research as well as the write-up of this thesis.

My thanks go also to the members of my advisory committee: Dr. Jay Doering, professor of Civil Engineering and Dean of the Faculty of Graduate Studies, and Dr. Vijay Chatoorgoon, professor of Mechanical and Manufacturing Engineering, as well as the external examiner, Dr. Gregory Jackson, professor of Mechanical Engineering at the University of Maryland, USA.

I thank my family for providing me with love, encouragement, and support that helped me throughout the course of this thesis.

Finally, I would like to acknowledge the financial support provided by the Natural Sciences and Engineering Research Council (NSERC) of Canada, and the University of Manitoba Graduate Fellowship (UMGF).

ABSTRACT

The effect of turbulence intensity on the drag coefficient of a sphere immersed in a turbulent airstream with Reynolds number, $\mathrm{Re} = U_\infty d / \nu_\infty$, ranging between 10 and 250 and freestream* turbulence intensity, u'_∞ / U_∞, of up to 60% is investigated numerically. Three-dimensional Reynolds-Averaged Navier-Stokes (RANS) equations along with mass conservation equation are solved in Cartesian coordinates by using a blocked-off technique in conjunction with a finite volume scheme. Closure for the turbulence stress term is accomplished by testing four different turbulence closure models. The predictions of the sphere drag coefficient in laminar flow conditions compare well with numerical and experimental published data. However, predictions of the sphere drag coefficient in turbulent airstream show that different turbulence closure models produce different trends in the range of Reynolds number up to Re =100, and this difference is demarcated by the non-agreement between the turbulent predictions and the well known sphere "standard"† drag coefficient. However, the results obtained by using Menter's SST turbulence model show fair agreement with the sphere "standard" drag coefficient over the range of test conditions explored here. Thus, the present results confirm recently published findings, which suggest that the freestream turbulence intensity does not have a significant effect on the sphere mean drag.

* In the present manuscript, the word "freestream" means "airstream"

† Standard drag coefficient refers to the well established sphere drag coefficient by Roos and Willmarth (1971) in laminar flow condition

The three-dimensional numerical model used for predicting sphere drag coefficient is extended to investigate the effect of turbulence on mass transfer from a single droplet exposed to a freestream of air. The governing equations for the gas-phase are mass, momentum (i.e., Reynolds-Averaged Navier-Stokes), energy and fuel mass fraction, whereas the governing equations for the liquid-phase (droplet) are mass, momentum and energy. Turbulence terms in the conservation equations of the gas-phase are modeled by using only the shear-stress transport (SST) model for the case of elevated temperature of freestream conditions and by using both the SST and LRN k-ε models in the case of freestream standard[‡] pressure and temperature conditions. The freestream temperature, turbulence intensity and Reynolds number are varied to provide a wide range of test conditions while the ambient pressure is kept atmospheric. The set of governing equations of the gas- and liquid-phases are solved by using the same technique as in the case of the sphere drag coefficient. The numerical results obtained at ambient standard pressure and temperature conditions show that the predictions based on the SST model agree reasonably well with published data. Furthermore, the vaporization Damköhler number proposed in the literature to correlate the effect of turbulence on the droplet's vaporization rate is found to be invalid at airstream temperatures higher than room temperature. Finally, a turbulent droplet's mass transfer correlation expressed in terms of Sherwood number is proposed.

[‡] standard conditions mean room temperature and atmospheric pressure conditions

Chapter

1

MOTIVATIONS AND OBJECTIVES

Many engineering power devices are liquid-fuelled combustion, such as diesel engines, rocket engines, ramjets/scramjets, and jet engines. In the combustion chamber of these devices fuel is injected as a spray or a jet. The liquid jet, for example, disintegrates into droplets of varying sizes (i.e., becomes a spray) which then vaporize and mix with the oxidizer inside the chamber forming a combustible mixture. This mixture eventually ignites when appropriate conditions are reached. The time required for achieving a combustible mixture of air and fuel vapor represents a significant fraction of the total time available for complete combustion. For example, in lean premix-prevaporized combustor a failure to quickly and fully vaporize the liquid fuel may lead to high levels of NO_x emissions. Therefore, the rate of fuel evaporation versus combustion time represents a key parameter in optimizing the level of NO_x emissions as well as the minimum length of a combustion chamber (Lefebvre, 1989). To improve the design and performance of these systems it is necessary to study and understand spray combustion.

One simplistic approach is by investigating an isolated droplet assuming that spray is made up of droplets of different sizes. Therefore, studying and understanding the vaporization of a droplet may provide a useful guidance for understanding and simulating the complex spray combustion.

Although a liquid fuel is injected as a spray (or a jet) into a high pressure, hot and turbulent gas flow environment, most of the previous studies on the evaporation of a droplet did not examine seriously the effect of turbulence. Their focus was more on the effect of ambient pressure and temperature, as well as laminar flow. This is driven by the belief that droplets forming a spray are always smaller than the most energetic eddies of the turbulent flow surrounding them and hence, the droplet is insensitive to turbulence as long as its size is smaller than that of the turbulence energetic eddies. However, recent investigations showed that even the smallest turbulence scales (i.e., the less energetic) may affect significantly the droplet evaporation (Ohta *et al.*, 1975; Park, 1987; Gökalp *et al.* 1992; Hiromitsu and Kawaguchi, 1995; Birouk, 1996; Birouk *et al.*, 1996; Birouk and Gökalp, 2002; Wu *et al.*, 2001 and 2003; Birouk and Gökalp, 2006). Most of these recent investigations did not study the effect of turbulence on droplet's evaporation at ambient high-pressure and high-temperature conditions. Indeed, almost all of these studies were performed under standard pressure and temperature flow conditions (Abou Al-Sood and Birouk, 2005c and 2006a)

Therefore the primary aim of the work presented in this thesis was to investigate numerically the effect of turbulence on a droplet evaporating under standard as well as hot freestream conditions. It was also the aim of this thesis to verify the sensitivity of the

mean (standard) drag coefficient of a constant-size droplet to the same freestream conditions of an evaporating droplet. Indeed, the present study is one of several research projects launched in the combustion laboratory to better understand the role of turbulence on droplet evaporation under realistic ambient pressure and temperature conditions.

The thesis consists of six chapters with five appendices. The motivations and objectives of the present study are outlined, here, in Chapter 1. The relevant literature review is reported in Chapter 2. The problem description and mathematical formulation of the numerical model are described in Chapter 3. The numerical approach and solution employed for solving the governing equations are reported in Chapter 4. The results and their discussions, which consist of two parts: the drag coefficient of a sphere exposed to a turbulent freestream and, the effect of a turbulence on droplet's evaporation under standard as well as hot freestream conditions, are presented in Chapter 5. Conclusions and suggestions for future work are summarized in Chapter 6. Appendix A gives details about the discretization of the governing equations. Methods for solving a systrem of linearized equations, which is resulted from discretizing the governing equations, are reported in Appendix B. Thermophysical properties of the liquid- and vapor-phases of *n*-heptane and *n*-decane, as well as those of the carrier gas (air) and the gas-fuel vapor mixing rules are given in Appendix C. Methodology for calculating the volume and surface area of the droplet by using the Blocked-off technique is briefly discussed in Appendix D. Finally, the evaporation rate of *n*-heptane and *n*-decane droplets in stagnant, laminar and turbulent freestream conditions are tabulated in Appendix E.

Chapter 2

LITERATURE REVIEW

Although the main focus of this review is on the effect of turbulence on droplet evaporation, the effect of turbulence on sphere drag coefficient is also reviewed due to its importance for droplets motion in a spray flow.

2.1 EFFECT OF TURBULENCE ON DRAG COEFFICIENT OF A NON-EVAPORATING DROPLET

Knowledge about drag coefficient of a sphere or a particle (a non-evaporating) or even an evaporating droplet is one of the most important hydrodynamic parameter for several industrial applications, which include particle mechanics, air cleaning devices, centrifugal or sedimentation separators, fluidized-bed reactors and, chemical and physical processes involving gas-bubbles or droplets (i.e., spray). The effect of laminar flow on sphere drag coefficient has been studied significantly in the open literature. Numerous studies have been devoted to this issue which led to the development of well accepted

correlations (See, for example, Roos and Willmarth, 1971; Schlichting, 1979; Clift *et al.*, 1978; Clift and Grace, 1989; and Warnica *et al.*, 1995a). However, the effect of turbulence on sphere drag coefficient is still not completely resolved.

Studies at high Reynolds numbers (Torobin and Gauvin, 1961; Clamen and Gauvin, 1969; Anderson and Uhlherr, 1970; Clift and Gauvin, 1971; and Sankagiri and Ruff, 1997) claimed that turbulence might increase or decrease the drag coefficient depending on the sphere (or particle) Reynolds number and flow turbulence intensities. These studies suggested that at low levels of turbulence intensity, an increase in drag coefficient was observed because of the interaction between turbulence and wake region, while at high levels of turbulence intensity, a sharp reduction in drag coefficients was observed sometimes because of the laminar-turbulent transition in the attached boundary layer. This phenomenon appeared to be similar to that under laminar flow at critical Reynolds numbers but turbulence forces this transition to happen at smaller Reynolds numbers (Brucato *et al.*, 1998). Neve (1986) and Neve *et al.* (1982, 1989) investigated the effect of turbulence intensity and macroscales on sphere drag where Reynolds number ranged between 2×10^3 and 2×10^5. They reported significant effects of turbulence macroscales as well as turbulence intensity when these scales were in the order of sphere diameter. They observed also that once the magnitude of theses scales reached approximately four times the sphere diameter, the sphere drag coefficient became almost equal to the standard drag coefficient.

For moderate to low ranges of Reynolds number the previous studies reported conflicting results. Experimental studies of Uhlherr and Sinclair (1970), Gore and Growe

(1990), Brucato *et al.* (1998), and a recent numerical study by Yusof (1996) reported an increase in the drag coefficient due to turbulence intensity. Whereas others (Petrak, 1976; Lee, 1987; Rudoff and Bachalo, 1988; Gore and Growe, 1990) claimed that turbulence intensity led to a decrease in the drag coefficient. Zarin and Nichols (1977) found that, for relative turbulence intensities less than 4%, the sphere drag coefficient is approximately similar to the standard drag coefficient. Recently, Warnica *et al.* (1995b) experimentally investigated the effect of turbulence intensity on a non-evaporating droplet in turbulent gas environment. Although they observed great scatter in their data, they suggested that their turbulence results did not show significant deviation from the standard drag coefficient obtained under laminar flow at similar Reynolds number. More recently, Bagchi and Balachandar (2003) conducted a direct numerical simulation (DNS) to determine the effect of turbulence on the drag of a particle and confirmed the suggestions made by Warnica *et al.* (1995b).

The literature survey above revealed that the effect of turbulence on sphere drag coefficient ranges between negligible to dramatic changes as compared to "standard" drag coefficient depending upon Reynolds number and turbulent flow conditions as shown in Figure 2.1. However, recent studies (Warnica *et al.*, 1995b; Bagchi and Balachandar, 2003) seemed to agree that there is a negligible effect of turbulence intensity on the non-evaporating droplet drag coefficient in the range of flow conditions pertinent to spray combustion. On the other hand these studies tested only low to moderate flow turbulence intensities. Hence one objective of the present numerical study was to shed more light on the effect of turbulence intensity on sphere drag coefficient

over a wider range of turbulence intensity and thus verify the conclusions of Bagchi and Balachandar (2003).

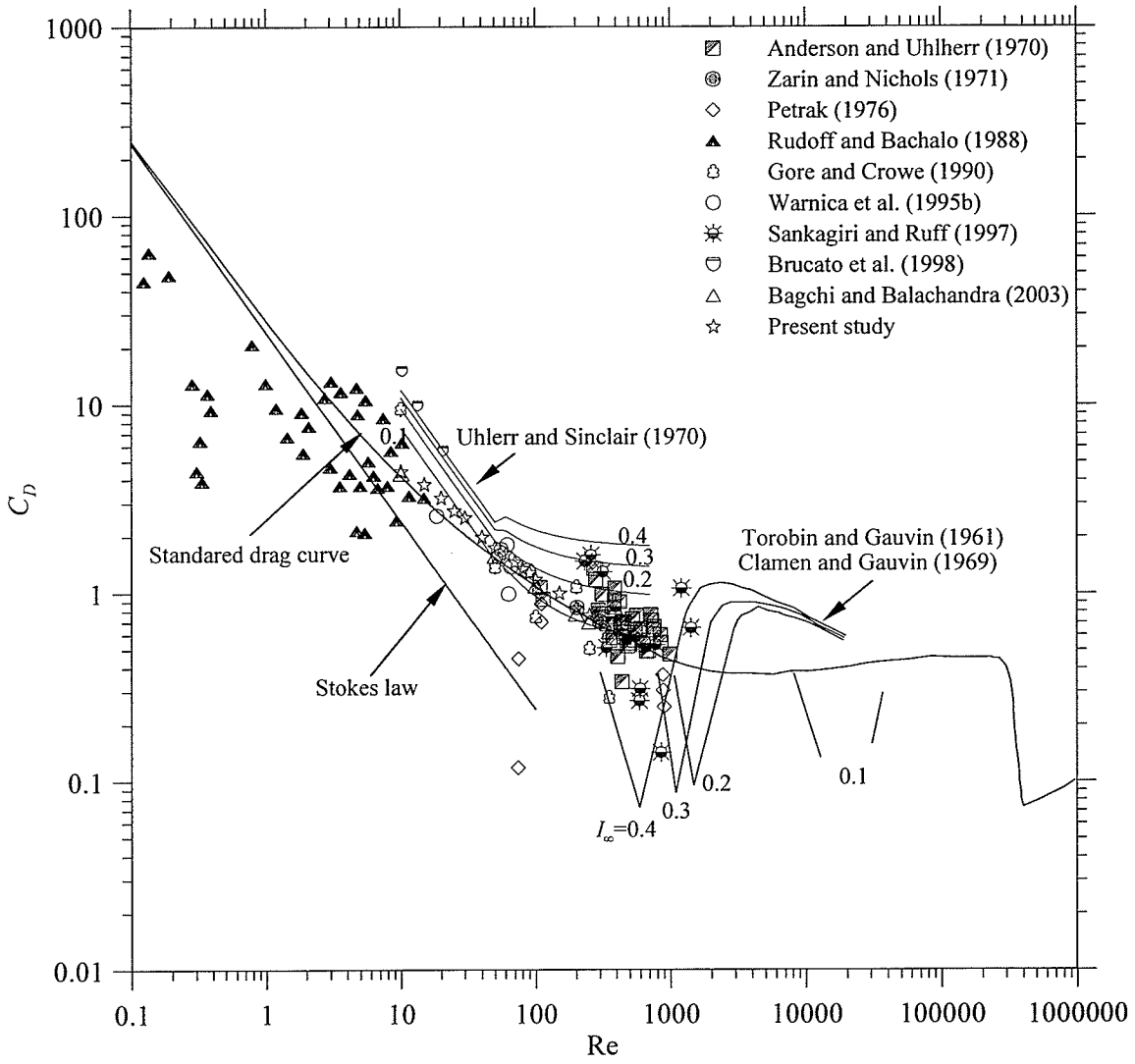

Figure 2.1 Drag coefficient of a sphere (or a particle) in turbulent flows

2.2 EFFECT OF TURBULENCE ON DROPLET (OR SPHERE) HEAT AND MASS TRANSFER

The effect of freestream turbulence on sphere heat and mass transfer was investigated first by Maisel and Sherwood (1950), and then followed by others (e.g. Hsu

and Sag, 1957; Brown *et* al., 1958; Yuge, 1959 and 1960; Venezian *et al.*, 1962; Galloway and Sage; 1964 and 1967; Lavender and Pei, 1967; Raithby and Eckert, 1968; Gostkowski and Costello, 1970; Hayward and Pei, 1978; Sandoval-Robles *et al.*, 1981; Yearling, 1995; Refai-Ahmed *et al.*, 1997). All these studies showed an increase in heat and mass transfer due to turbulence except Hsu and Sage (1957) and Yuge (1959 and 1960) who claimed that turbulence had a negligible effect especially at low Reynolds number. In addition, with the exception of Raithby and Eckert (1968), most of these early studies did not investigate the effect of turbulence length scale on sphere heat and mass transfer. Raithby and Eckert (1968) predicted an increase in transfer rate due to a decrease in the ratio of the sphere diameter over the integral length scale. Briefly, most of these studies correlated the effect of turbulence on sphere (or droplet) heat and mass transfer by using Nusselt (*Nu*) and Sherwood (*Sh*) numbers. These numbers were expressed in terms of Reynolds (Re), Prandtl (Pr) and Schmidt (*Sc*) numbers as well as turbulence quantities as follows (Birouk and Gökalp, 2006)

$$Nu = A' + B' \mathrm{Re}^{1/2} \mathrm{Pr}^{1/3} (C_T) \tag{2.1}$$

$$Sh = A' + B' \mathrm{Re}^{1/2} Sc^{1/3} (C_T), \tag{2.2}$$

where C_T is a turbulent term and, A' and B' are constants. For droplet heat and mass transfer, Nusselt and Sherwood numbers are to be corrected by $(1+B_T)^{0.7}$ and $(1+B_M)^{0.7}$, respectively (Renksizbulut and Yuen, 1983b) where B_M and B_T are the mass and heat transfer numbers, respectively. The different values of A', B' and C_T are given in Table 2.1. In addition, a comparison between these correlations is shown in Figure 2.2 where $(Nu - A')/\mathrm{Re}^{1/2} \mathrm{Pr}^{1/3}$ or $(Sh - A')/\mathrm{Re}^{1/2} Sc^{1/3}$ are plotted versus C_T for 17≤ Re ≥ 186

and $0 \leq I_\infty \geq 0.6$, which are the ranges of the present study. This figure shows that C_T varies between 1.127 and 2.022 for mass transfer and between 1.075 and 1.524 for heat transfer. The present study predicts the highest value of C_T, i.e., 2.022, for mass transfer and Yearling (1995) predicts the highest value of C_T, i.e., 1.524, for heat transfer. However, a close examination of Yearling (1995) laminar and turbulent data shows no marked effect of turbulence on heat and mass transfer.

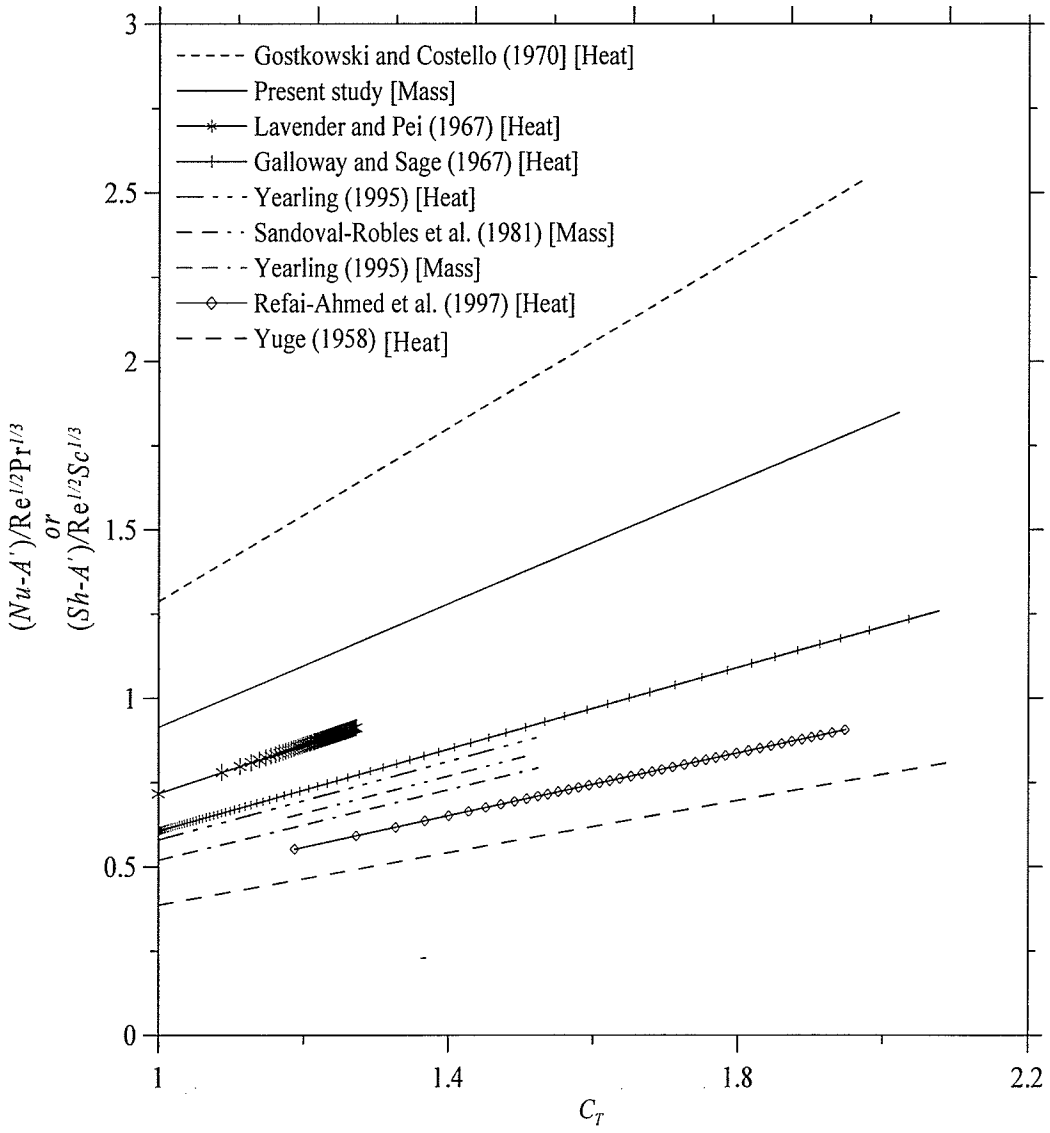

Figure 2.2 Turbulent droplet (or sphere) heat and mass transfer correlations

Table 2.1 Summary of published sphere (or droplet) heat and mass transfer correlations

Ref.	*Nu* or *Sh*	A'	B'	C_T	Validity	Error*
Galloway and Sage (1967)	*Nu* or *Sh*	2	1.0	$0.562+0.1807d^{1/2}+0.0672I_\infty$ $(I_\infty+0.05)\mathrm{Re}_\infty^{1/2}$	$0.01 \le I_\infty \le 0.15$ $2 \le \mathrm{Re}_\infty \le 1.33\mathrm{X}10^6$ $0.02'' \le d \le 12''$	4.2%
Galloway and Sage (1967)	*Nu*	2	1.0	$0.538+0.1807d^{1/2}+0.328I_\infty$ $(I_\infty+0.0405)\mathrm{Re}_\infty^{1/2}$	$0.01 \le I_\infty \le 0.15$ $2 \le \mathrm{Re}_\infty \le 1.33\mathrm{X}10^6$	14.6%
Galloway and Sage (1967)	*Sh*	2	1.0	$0.439+0.1807d^{1/2}+0.234I_\infty$ $(I_\infty+0.0500)\mathrm{Re}_\infty^{1/2}$	$0.01 \le I_\infty \le 0.15$ $2 \le \mathrm{Re}_\infty \le 1.33\mathrm{X}10^6$	6.6%
Lavender and Pei (1967)	*Nu* *Nu*	2 2	0.717 0.165	$(\mathrm{Re}\, I_\infty)^{0.035}$ $(\mathrm{Re}\, I_\infty)^{0.250}$	$\mathrm{Re}\, I_\infty < 1000$ $\mathrm{Re}\, I_\infty > 1000$	10% 10%
Yuge (1959) correlated by Lavender and Pei (1967)	*Nu*	2	0.387	$(\mathrm{Re}\, I_\infty)^{0.085}$	$\mathrm{Re}\, I_\infty < 7000$	
Gostkowski and Costello (1970)	*Nu* *Nu*	0 0	1.431 1.287	$(\mathrm{Re}\, I_\infty)^{0.0214}$ $(\mathrm{Re}\, I_\infty)^{0.2838}$	$\mathrm{Re}\, I_\infty < 7000$ $\mathrm{Re}\, I_\infty > 7000$	
Sandoval-Robles (1981)	*Sh*	0	0.549	$(\mathrm{Re}\, I_\infty)^{0.066}$	$12 < \mathrm{Re}\, I_\infty < 600$	10%
Yearling (1995)	$Nu(1+B_T)^{0.7}$ $Sh(1+B_M)^{0.7}$	2 2	0.58 0.52	$1+3.397I_\infty^{0.843}$ $1+3.397I_\infty^{0.843}$	$0.01 \le I_\infty \le 0.11$ $50 < \mathrm{Re} < 1500$	
Refai-Ahmed *et al.* (1997)	*Nu*	0	0.465	$\mathrm{Re}^{0.109} I_\infty^{0.174}$	$0.012 \le I_\infty \le 0.049$ $5642 < \mathrm{Re} < 56420$	6.6%
Present Study	$\mathrm{Sh}(1+B_M)^{0.7}$	2	0.914	$1+1.235I_\infty^{0.372}$	$0.01 \le I_\infty \le 0.6$ $17 < \mathrm{Re} < 186$	

* Error=[(Experimental data-Best fit)×100]/best fit

It is important to note that these studies did not investigate sufficiently high turbulence intensity levels. However, recent published works (Gökalp *et al.*, 1992; Hiromitsu and Kawaguchi 1995; Birouk *et al.*, 1996; Birouk and Gökalp, 2002 and Wu *et al.* 2001 and 2003) investigated high levels of turbulence intensity.

Ohta *et al.* (1975) studied the vaporization and combustion of a fuel droplet in a turbulent gas environment with zero mean-velocity. Their experimental study was performed at room temperature and atmospheric pressure. They showed that the evaporation rate increased by about 67% due to an increase in velocity fluctuation from 25 cm/s to 120 cm/s. Gökalp *et al.* (1992) studied experimentally the effect of turbulence on the evaporation rates of *n*-heptane and *n*-decane droplets at atmospheric pressure and room temperature conditions. Gökalp *et al.* (1992) reported that turbulence intensity was varied up to 44 % and the integral length scale was several times greater than the initial droplet (i.e., $L_i/d_0 \leq 5$). Their results showed a weak effect of turbulence intensity on the evaporation rate of *n*-heptane droplet. However, the same turbulence showed significant influence on *n*-decane droplet. They proposed an effective vaporization Damköhler number Da_v to explain the effect of turbulence on droplet mass transfer. This number was defined as a competition between the turbulence characteristic time scale, T_t, and the vaporization characteristic time scale, T_v, (i.e., $Da_v = T_t / T_v$). They predicted that turbulence is effective only when $Da_v << 1$.

Hiromitsu and Kawaguchi (1995) measured the droplet evaporation rate in hot airflow of a mean-velocity of 2 m/s for several liquids including *n*-hexane, *n*-heptane, *n*-octane, distilled water and ethanol. Their temperature ranged between 323 and 423 K,

and turbulence intensity was varied in the range between 3% and 20%. They found that the effect of turbulence intensity on the droplet turbulent evaporation rate, K_t, depends also on the physical properties of the droplet and atmosphere conditions. Furthermore, they tested the vaporization Damköhler number correlation developed by Gökalp *et al.* (1992) and claimed that this correlation was invalid when the ambient gas temperature exceeds the droplet boiling temperature.

Birouk (1996) and Birouk *et al.* (1996) developed an apparatus capable of generating a zero-mean velocity, isotropic and homogenous flow with varying turbulence kinetic energy. The apparatus (i.e., a cubic chamber) was used to study the effects of turbulence on droplet vaporization at standard temperature and pressure conditions. The ratio between turbulence integral length scale and droplet initial diameter was found to be around 5. The results of Birouk (1996) and Birouk *et al.* (1996) showed that the presence of turbulence speeds up the droplet average evaporation rate as compared to its counterpart under stagnant flow conditions. For a given turbulent kinetic energy, it was also found that the droplet evaporation rate is higher for the less volatile fuel. Phenomenological model for the effect of turbulence on the vaporization of a single fuel droplet was suggested and discussed in terms of turbulence diffusivity ($D_t = \sqrt{k} d_0$) and molecular diffusivity of the fuel vapor (($D_m = \nu / D_{AB}$), where k is the turbulence kinetic energy, d_0 is the initial droplet diameter, υ is the kinematics viscosity and D_{AB} is the molecular diffusion coefficient. Birouk and Gökalp (2002) proposed an empirical correlation as a function of turbulence Reynolds number ($\mathrm{Re}_t = k^{1/2} d_0 / \nu$) and Schmidt number ($Sc = \nu / D_{AB}$), which has the following form

$$K/K_0 = 1 + 0.02\,\mathrm{Re}_t^{2/3}\,Sc^2\,, \tag{2.3}$$

where K_0 is the stagnant vaporization rate. Schmidt number for *n*-heptane and *n*-decane were calculated at ambient standard conditions, and Schmidt number for bi-component droplets was calculated as

$$Sc_A = X_A Sc_A + (1 - X_A) Sc_B, \tag{2.4}$$

where X_A is the mole fraction of component A.

Recently, Wu *et al.* (2001 and 2003) studied experimentally the effect of turbulence and fuel properties on the vaporization of a liquid fuel droplet suspended in quasi-laminar and turbulent environments at Reynolds number in the range $72 \leq \mathrm{Re}_d \leq 333$) at standard temperature and pressure conditions. Reynolds number, Re_d, definition was based on the initial droplet diameter and freestream conditions. Turbulence conditions included turbulence intensity in the range between 1% and 60%, the ratio of the turbulence integral length scale to initial droplet diameter, L_t/d_0, in the range between 0.5 and 20 and, the ratio of Kolmogorov length scale to the initial droplet diameter in the range from 0.02 to 0.13. Their experimental data were used to suggest the following correlation

$$K/K_L = 0.771 Da_v^{-0.111}, \tag{2.5}$$

which confirmed Gökalp *et al.* (1992) conclusion that the effect of ambient turbulence on droplet vaporization is negligible for a Damköhler number larger than 0.1, as shown in Figure 2.3.

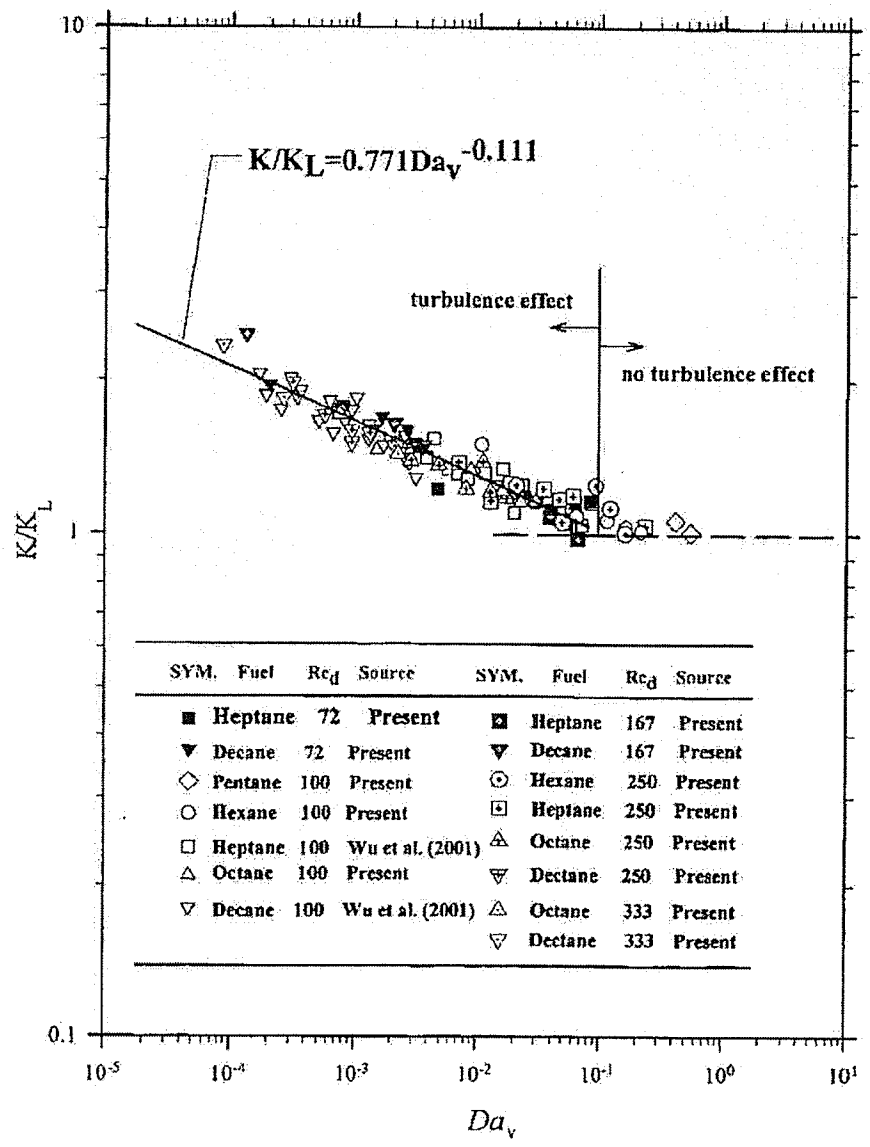

Figure 2.3 Variation of the droplet turbulent evaporation rate normalized by its counterpart's laminar value versus the vaporization Damköhler number (Wu *et al.*, 2003)

Numerical studies of the effect of turbulence on droplet vaporization are almost nonexistent. The exception concerns Park (1987) who developed a 2D numerical model to investigate the effect of turbulence on *n*-hexane droplet having an initial diameter ranging between 100 and 400 μm. Park's test conditions included also Reynolds number in the range between 20 and 200, and turbulence intensity in the range between 0% and

50%. In addition, the ambient temperature was also varied (700 K and 1000 K) and the ambient pressure was kept constant. The main conclusion of this numerical study was that turbulence enhances the droplet evaporation rate. It is important to notice that this model was a two-dimensional (2D) model which obviously cannot represent the characteristics of a turbulent flow over a droplet (or a sphere).

The literature survey above revealed that although great progress was made in the last decade on advancing our understanding of the effect of turbulence on droplet evaporation, more experimental and numerical studies are needed especially under realistic conditions. For example, Gökalp and his co-workers (Gökalp *et al.*, 1992) introduced an interesting approach for correlating turbulence and droplet evaporation. They employed a non-traditional method by introducing a non-dimensional number (i.e., vaporization Damköhler number). This non-dimensional number was used to explain the effect of turbulence on droplet's evaporation in terms of a competition between the characteristic times of turbulence and evaporation. Recent experimental studies by Wu *et al.* (2001 and 2003) led to the establishment of Gökalp et *al.*'s approach.

However, the studies by Gökalp *et al.* (1992) and Wu *et al.* (2001 and 2003) were carried out at ambient standard pressure and temperature conditions. On the other hand, Hiromitsu and Kawaguchi (1995) tested the aforementioned Damköhler correlation at ambient temperatures of up to 423K and claimed that this correlation would not work for a droplet evaporating in a turbulent hot environment.

Therefore, the primary objective of this study was to examine the validity of this correlation over a wide range of turbulent intensity and ambient temperature conditions and, thus to verify the view of Hiromitsu and Kawaguchi (1995) discussed above.

Chapter

3

PROBLEM DISCRIPTION AND MATHEMATICAL FORMULATION

This chapter discusses theoretical analysis of a stationary sphere (or fuel droplet) immersed in a turbulent freestream. Details are provided about the physical problem, model assumptions and governing equations, as well as different turbulence closure models tested in this study. Freestream conditions, gas-liquid interface conditions and wall boundary conditions, which are used in the numerical model, are also presented.

3.1 DESCRIPTION OF THE PHYSICAL PROBLEM

Consider a stationary droplet (or a sphere) with initial radius r_0 and initial uniform temperature T_0 immersed into a turbulent inert freestream of infinite expanse. The freestream initial conditions are: mean-velocity, U_∞, pressure, p_∞, temperature, T_∞, fuel mass fraction, $Y_{F\infty}$ (only for the case of droplet), turbulence intensity, I_∞, and turbulence dissipation rate, ε_∞, or turbulence dissipation per unit of turbulence kinetic energy, ω_∞.

A stationary droplet (or a sphere) exposed to turbulent airstream is schematically shown in Figure 3.1.

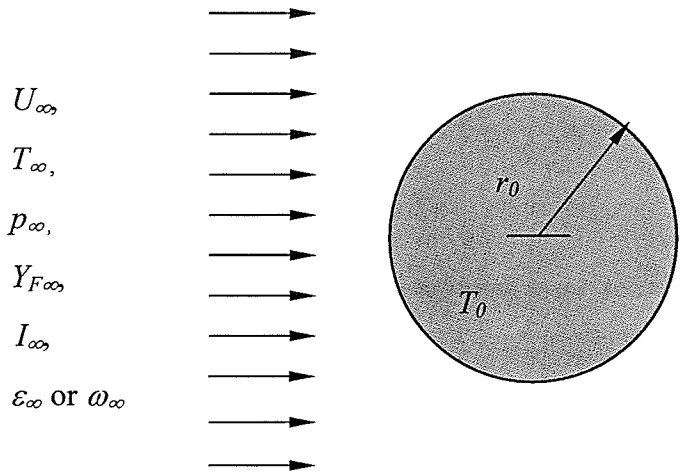

Figure 3.1 Schematic of the physical problem; i.e., a droplet (or a sphere) exposed to freestream of air

Droplet's temperature is generally less than that of the freestream (gas-phase), therefore, energy is transferred from the gas-phase to the liquid-phase (droplet). Initially, part of this energy is used to heat-up the interior of the droplet, and the rest is used for the droplet's evaporation. This scenario continues until the droplet surface temperature reaches a certain value, i.e., wet bulb temperature, beyond which all the transferred energy is used for droplet evaporation only. Consequently the droplet evaporation leads to a decrease in the droplet diameter as shown in Figure 3.2. The steady-state droplet's evaporation is characterised by a linear slope, i.e., the squared droplet diameter, d^2, which decreases linearly with time, t. The slope of the droplet's steady-state evaporation curve represents the evaporation rate, K, where $(d/d_0)^2 = 1\text{-}K\ (t/d_0^2)$, as shown in Figure 3.2. The evaporating fuel is then diffused and convected away from the droplet surface and the gas-phase becomes a mixture of air and fuel vapour.

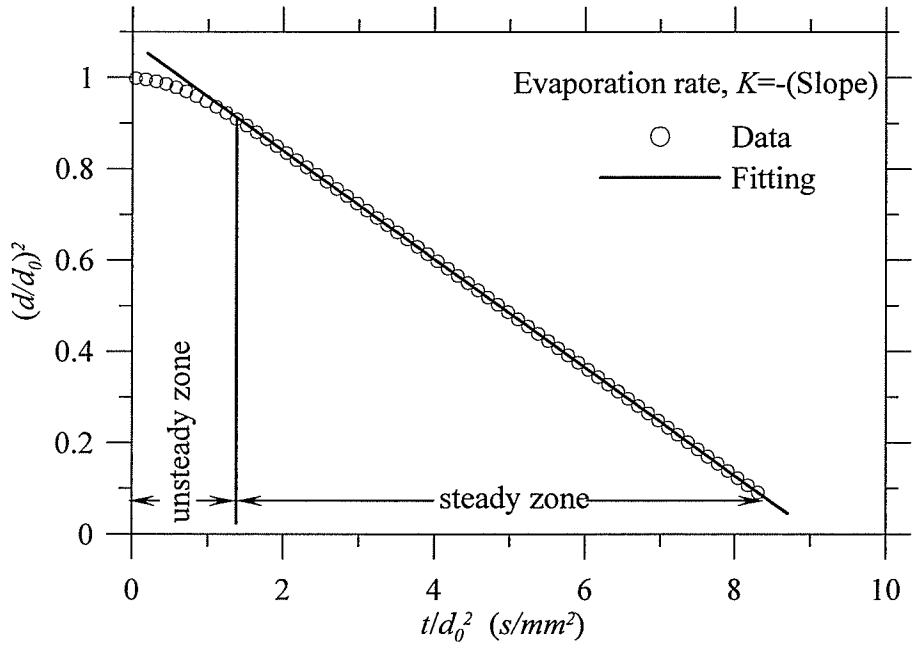

Figure 3.2 Time history of the droplet squared normalized diameter

3.2 MODEL ASSUMPTIONS

The flow over a sphere is assumed steady, turbulent with no heat transfer from/to the sphere. The sphere remains stationary all time. However, for flow over an evaporating droplet, the following assumptions are employed: (i) the droplet is composed of a single hydrocarbon component with no chemical reaction with the surrounding gas; (ii) the droplet shape remains spherical, as the Weber number ($We = \rho U_\infty^2 d / \gamma_d$) is assumed to be much less than unity; (iii) the gas-phase is turbulent with predefined freestream turbulence intensity; (iv) radiation is negligible;(v) second order effects, such as Dufour (energy flux due to mass concentration) and Soret (mass diffusion due to temperature) effects are not considered and (vi) the solubility of the ambient gas into liquid-phase is generally important at high pressure and, therefore, it is not considered in this study, as the pressure is kept atmospheric .

3.3. GOVERNING EQUATIONS

3.3.1 TURBULENT FLOW OVER A SPHERE

The governing equations for a turbulent flow over a sphere are: steady state, three dimensional, mass conservation and Reynolds-Averaged Navier-Stokes (RANS), which are

$$\frac{\partial}{\partial x_i}(\rho U_i) = 0, \tag{3.1}$$

$$\frac{\partial}{\partial x_j}(\rho U_i U_j) = -\frac{\partial p}{\partial x_i} + \frac{\partial}{\partial x_j}\left(\mu \frac{\partial U_i}{\partial x_j} - \overline{\rho u_i' u_j'}\right), \tag{3.2}$$

where ρ , μ, U_i, p are density, dynamics viscosity, mean-velocity components, and pressure, respectively. Whereas u_i' is the fluctuating velocity component. The "bar" denotes the average value and the subscripts i and j, which can be 1, 2 or 3, denote the three instantaneous velocity components in the three directions (x_i or x_j).

Averaging Navier-Stokes equations results in six new unknowns, i.e., Reynolds stresses, in addition to original three velocity components and pressure. Consequently, the number of unknowns exceeds the number of equations. Solving these averaged equations can only be possible by adding additional equations, which is termed as "*closure problem*". Turbulent stresses, $\overline{u_i' u_j'}$, are assumed to act like viscous stresses that are proportional to the mean velocity gradient. This assumption is made by Boussinesq who introduced "*turbulence*" or "*eddy*" viscosity, ν_t, as

$$-\overline{u_i' u_j'} = \nu_t\left(\frac{\partial U_i}{\partial x_j} + \frac{\partial U_j}{\partial x_i}\right) - \frac{2}{3}\left(k + \nu_t \frac{\partial U_i}{\partial x_i}\right)\delta_{ij}, \tag{3.3}$$

where δ_{ij} is the Kronecker delta (which equal to 0 if $i \neq j$ and 1 if $i=j$) . The eddy viscosity is modeled as

$$\nu_t = C_\mu f_\mu \frac{k^2}{\varepsilon}, \tag{3.4a}$$

or

$$\text{or } \nu_t = \frac{k}{\omega}, \tag{3.4b}$$

where C_μ is a constant that depends on the turbulence model used, f_μ is a damping function employed to compensate for low Reynolds number effect in the near wall regions, k is the turbulence kinetic energy, ε is the dissipation rate of turbulence kinetic energy, and ω is the dissipation rate per unit of turbulence kinetic energy.

Turbulence terms, i.e., k and ε or ω, may be obtained by introducing turbulence closure models. In the present study, the following models are employed: low-Reynolds number (LRN) k-ε of Jones and Launder (1973), low-Reynolds number (LRN) k-ω of Wilcox (1992), as well as the baseline (BSL) and shear stress transport (SST) blended k-ε / k-ω models of Menter's (1994). Details about these models are reported in Section 3.5 below.

3.3.2 TURBULENT FLOW OVER AN EVAPORATING DROPLET

3.3.2.1 GAS-PHASE

The conservation equations for a turbulent flow over an evaporating droplet are unsteady, three dimensional, mass conservation and Reynolds-Averaged Navier-Stokes (RANS), as well as energy and fuel mass fraction, which are

$$\frac{\partial \rho}{\partial t}+\frac{\partial}{\partial x_i}(\rho U_i)=0, \tag{3.5}$$

$$\frac{\partial}{\partial t}(\rho U_i)+\frac{\partial}{\partial x_j}(\rho U_i U_j)=-\frac{\partial p}{\partial x_i}+\frac{\partial}{\partial x_j}\left(\mu\frac{\partial U_i}{\partial x_j}-\overline{\rho u_i' u_j'}\right), \tag{3.6}$$

$$\frac{\partial}{\partial t}(\rho T)+\frac{\partial}{\partial x_j}(\rho U_i T)=\frac{\partial}{\partial x_j}\left(\frac{\mu}{\Pr}\frac{\partial T}{\partial x_j}-\overline{\rho u_i' T'}\right), \tag{3.7}$$

$$\frac{\partial}{\partial t}(\rho Y_F)+\frac{\partial}{\partial x_j}(\rho U_i Y_F)=\frac{\partial}{\partial x_j}\left(\frac{\mu}{Sc}\frac{\partial Y_F}{\partial x_j}-\overline{\rho u_i' Y_F'}\right), \tag{3.8}$$

where Pr and Sc are Prandtl and Schmidt numbers, respectively, T and Y_F are the mean values of temperature and fuel mass fraction, respectively. Whereas T', and Y_F' are the fluctuating components of temperature and fuel mass fraction, respectively.

The heat and mass flux terms of Eqs. (3.7) and (3.8), which are due to turbulence, can be handled by using Jones and Launder (1973) assumption of laminar heat and mass transfer and introducing turbulence Prandtl or Schmidt number as

$$-\overline{\rho u' T'}=\lambda_t\frac{\partial T}{\partial x_j}=\frac{\mu_t}{\sigma_h}\frac{\partial T}{\partial x_j}, \tag{3.9}$$

$$-\overline{\rho u' Y_f'}=D_{ABt}\frac{\partial Y_f}{\partial x_j}=\frac{\mu_t}{\sigma_t}\frac{\partial Y_f}{\partial x_j}, \tag{3.10}$$

where σ_h and σ_t are the turbulent Prandtl and Schmidt numbers, respectively. These numbers are assumed constants (i.e., 0.9 and 0.85, respectively) and independent of Reynolds number (Jones and Launder, 1973).

In the present work, closure of turbulence terms are accomplished by testing low-Reynolds number (LRN) model developed by Jones and Launder (1973) and shear stress transport (SST) blended k-ε / k-ω model developed by Menter (1994). Note that the LRN k-ε model can be applied directly to both viscous sublayer and fully turbulent regions. The SST model is a combination of k-ε and k-ω models. It uses k-ω model near the wall (sub- and log-layer) and k-ε model away from the wall, which is made possible by introducing a blending function, as discussed in Section 3.5 below.

The characteristic time for changes in the gas-phase, which is the residence time in the boundary layer of the droplet ($r/U_\infty = O(10^{-3})$ sec), is much smaller than the droplet lifetime ($t_{evap} = O(10)$ sec). Therefore, the quasi-steady gas-phase assumption can be employed (Prakash and Sirginano, 1980). The unsteady term can be cancelled by taking a time interval in the discretisation equation of the order 10^{30} seconds. In this study, the unsteady terms in the conservation equations are cancelled at room temperature while they are considered in the case of higher temperature.

3.3.2.2 Liquid-PHASE

Most of airflows in practical combustion chambers are characterized by high Reynolds numbers. High Reynolds numbers cause high shear stresses at the interface between the droplet and the gas-phase. Therefore, the shear stresses are high enough to cause internal circulations inside the droplet, which is important for heat transfer inside

the droplet (Parakash and Sirginano, 1978). Therefore, it is important to include the convective motion inside the droplet by solving the liquid-phase unsteady conservation of mass and momentum equations together with energy equation. Since in this study the droplet is composed of a single fuel component, the species equation is not introduced in the liquid-phase as its solution is unity in the liquid-phase. The governing equations are then

$$\frac{\partial \rho_l}{\partial t} + \frac{\partial}{\partial x_i}\left(\rho_l U_{i,l}\right) = 0, \tag{3.11}$$

$$\frac{\partial}{\partial t}\left(\rho U_{i,l}\right) + \frac{\partial}{\partial x_j}\left(\rho U_{i,l} U_{j,l}\right) = -\frac{\partial p_l}{\partial x_i} + \frac{\partial}{\partial x_j}\left(\mu_l \frac{\partial U_{i,l}}{\partial x_j}\right), \tag{3.12}$$

$$\frac{\partial}{\partial t}\left(\rho_l T_l\right) + \frac{\partial}{\partial x_j}\left(\rho_l U_{i,l} T_l\right) = \frac{\partial}{\partial x_j}\left(\frac{\mu_l}{\mathrm{Pr}_l}\frac{\partial T_l}{\partial x_j}\right), \tag{3.13}$$

where subscript *l* denotes liquid-phase.

3.5 TURBULENCE MODELS

Turbulence is a very complicated state of fluid motion. Although the equations governing turbulent flows (i.e., Navier-Stokes equations) are well known, their numerical solution is still not easy, even with today's computers technology. In fact, the simulation and modeling of turbulent flows require far too much memory and time to be practically realizable. The area of "Turbulence Modeling" combines the experimental knowledge of turbulence with the mathematical character of the equations to develop closures for the unknown parameters at a statistical level. These closures make the prediction of turbulence feasible with a reasonable accuracy and computer execution time.

The starting point in turbulence modeling is the Reynolds decomposition. It is assumed that all flow quantities, $f_i(x_i,t)$, can be decomposed into a mean-component and a fluctuating component as

$$f_i(x_i,t) = \underbrace{F_i(x_i,t)}_{Mean} + \underbrace{f_i'(x_i,t)}_{Fluctuation}, \tag{3.14}$$

where $F_i(x_i,t)$ is the time-averaged (mean) component, and $f_i'(x_i,t)$ is the fluctuating component. The time-averaged quantity is defined as (Hinze, 1959; Tennekes and Lumley, 2001)

$$F_i(x_i,t) = \lim_{T\to\infty} \frac{1}{T} \int_{t_o}^{t_o+T} f_i(x_i,t)dt\,. \tag{3.15}$$

Diffusion equations for the mean values of these quantities in tensor form are derived by substituting the decomposed form into any diffusion equation as follow

$$\frac{D\rho F_i}{Dt} = \frac{\partial}{\partial x_j}\left(\Gamma_{F_i}\frac{\partial F_i}{\partial x_j} - \overline{\rho u_j' F_i'}\right) + S_{F_i}, \tag{3.16}$$

where *D/Dt* represents the total derivatives as

$$\frac{DF_i}{Dt} = \frac{\partial F_i}{\partial t} + \frac{\partial(U_j F_i)}{\partial x_j}\,. \tag{3.17}$$

However, this introduces new variables without adding extra equations. The aim is to model these new variables in terms of the mean values of the original variables as a set of partial differential equations making the prediction of turbulence possible. The degree of accuracy of each turbulence model depends on the validity of the assumptions being used. Turbulence models can be classified into: (i) Eddy viscosity models, (ii) Reynolds stress models and, (iii) Large-Eddy Simulation (LES) models. Since the present study deals with mass, momentum, energy and fuel mass fraction equations, eddy

viscosity models are chosen for modelling the turbulence terms in these equations because they are economical in terms of the required memory and time.

There are several levels of eddy viscosity models. The simplest level is that of the Boussinesq approximation. This model uses an analogy between the Reynolds' stresses and the mean flow gradient (see Eq. (3.3)).

Eddy viscosity, ν_t, is proportional to the mean velocity field. The concept of eddy viscosity is phenomenological and has no mathematical basis. Molecular viscosity, ν, is a fluid property, but eddy viscosity is a flow property that changes from one point to another in the flow and from one flow to another. It depends strongly on the state of turbulence. Hence, the eddy viscosity is likely to be a function of the flow properties (Robert and Desiraju, 1976)

. The eddy viscosity can be algebraically formulated in terms of quantities derived from partial differential equations. These quantities may be k, ε, or ω depending on the type and number of equations, which then called, zero, one- or two-equation models. The zero-equation model is widely used in practical engineering CFD codes. The one-equation model is widely employed in early stages of turbulence modeling and it is still in use but for limited flow regions such as the near-wall sublayer. In these regions, the one-equation model is much simpler to use than the other more complicated models. The two-equation model is employed when additional details of turbulence quantities are required.

3.5.1 ZERO-EQUATION MODELS

Zero-equation models do not involve the transport equation for turbulence quantities. These relatively simple models employ the eddy viscosity concept which can be obtained directly from experiments, trial and error through empirical formulas, or from relating it to the mean-velocity distribution (Reynolds, 1976). Examples of such models include the constant eddy viscosity model and mixing-length models. One of the most famous mixing length models is that of Prandtl (1925) who suggested that the eddy viscosity is proportional to the mixing length, l_m, and the characteristic velocity of turbulence, V_t, as

$$\nu_t \propto l_m V_t \tag{3.18}$$

$$V_t \propto l_m \left|\frac{\partial U}{\partial y}\right| \tag{3.19}$$

$$\nu_t \propto l_m^2 \left|\frac{\partial U}{\partial y}\right| \tag{3.20}$$

The mixing length models are not suitable when the process of convective or diffusive transport of turbulence is important, i.e., rapidly developing flows and recirculating flows. In general, these models are of little use in complex flows because of the great difficulties in specifying the mixing length l_m. However, for many simple shear flows where l_m can be specified empirically, the mixing length models are a very useful and a popular tool.

3.5.2 ONE - EQUATION MODEL

In order to overcome the limitations of the mixing length hypothesis, turbulence models are developed to account for the transport of turbulence quantities by solving transport equations for these quantities. An important step in the development is to yield a direct link between the fluctuating velocity scale and the mean-velocity gradients and thus determine this scale from a transport equation. If the velocity fluctuations are to be characterized by only one turbulence scale, then the physically meaningful scale is $\sqrt{k}$, where k is the turbulence kinetic energy. Because the energy k is contained mainly in the large-scale fluctuations, $\sqrt{k}$ is a velocity scale for the large-scale turbulence motion. When this scale is used in the eddy viscosity model relation, the equation (3.20) becomes that of Kolmogorov-Prandtl expressed as follows (Tennekes and Lumley, 2001)

$$\nu_t = c_\mu L_i \sqrt{k}\,, \tag{3.21}$$

where, c_μ is an empirical constant, L_i is the turbulence integral length scale, and k is the turbulence kinetic energy that can be obtained by solving the transport equation for k. The exact transport equation for k can be obtained from the Navier-stokes equation by setting i=j for the Reynolds stress, $\overline{u_i u_j}$, as

$$\frac{\partial k}{\partial t} = \underbrace{-\frac{\partial}{\partial x_j}\left\{ kU_j + \overline{u_j\left(\frac{u_i u_i}{2}+\frac{p}{\rho}\right)} - \nu\overline{u_i\left(\frac{\partial u_i}{\partial x_j}+\frac{\partial u_j}{\partial x_i}\right)}\right\}}_{\text{Diffusion term}} \underbrace{-\overline{u_i u_j}\left\{\frac{\partial U_i}{\partial x_j}\right\}}_{\text{Production term}} - \underbrace{\varepsilon.}_{\text{Dissipation term}} \tag{2.22}$$

The k-equation alone is of no use in turbulence modeling because new unknown correlations appear in the diffusion and dissipation terms. To obtain a closed set of equations, model assumptions must, therefore, be introduced for these terms. In analogy to the diffusion expression for scalar quantities, the diffusion flux of k is often assumed proportional to the gradient of k as follows (Hinze, 1959).

$$\overline{u_j\left(\frac{u_i u_i}{2}+\frac{p}{\rho}\right)}=\frac{\nu_t}{\sigma_k}\frac{\partial k}{\partial x_j}, \tag{3.23}$$

where σ_k is an empirical diffusion constant. The dissipation is usually modeled by the following expression

$$\varepsilon = C'\frac{k^{3/2}}{L_i}, \tag{3.24}$$

where C' is an empirical constant. With the above model assumptions and the eddy viscosity expression, the modeled k-equation becomes

$$\frac{\partial k}{\partial t}+U_j\frac{\partial k}{\partial x_j}=\frac{\partial}{\partial x_j}\left(\frac{\nu_t}{\sigma_k}\frac{\partial k}{\partial x_j}\right)+\nu_t\left(\frac{\partial U_i}{\partial x_j}+\frac{\partial U_j}{\partial x_i}\right)\frac{\partial U_j}{\partial x_i}-C'\frac{k^{3/2}}{L_i}\,. \tag{3.25}$$

Equation (3.25) is the high Reynolds number form of the transport equation for k used in most one-equation models. The last term in this equation (dissipation term) contains the length scale L_i which requires to be specified to complete the turbulence model, which is distinguished as the various one-equation models. In most cases, the length scale L_i is determined from empirical relations similar to mixing length l_m. The results obtained with these kinds of models are satisfactory but not much better than zero-

equation models. The exception concerns the one-equation model developed by Spalart and Allmaras (1992) for high speed external flow applications (De Kock, 2005)..

3.5.3 TWO-EQUATION MODEL

The shortcoming of the one-equation models is the difficulty to specify empirically the length scale L_i in the case of more complex flows. In an attempt to eliminate the need for specifying L_i as a function of position throughout the flow, the two-equation models are produced. The length scale L_i characterizing the large eddies contains much of the turbulence energy that is subjected to transport processes in a manner similar to k. Two of the most important processes that influence this length scale are the dissipation and the vortex stretching and their interaction with the energy cascade. The balance between these processes can be expressed by using a transport equation for L_i to find its distribution throughout the flow. The L_i transport equation must be solved alongside a transport equation for the velocity scale V, i.e., k-equation. The length scale equations are a combination in the form (Kantha, 2004)

$$Z = k^m L_i^n . \tag{3.26}$$

The most common combinations are listed in Table 3.1

Table 3.1 Length scale equations

1.	Frequency (Kolmogorov, 1942)	$\omega = k^{1/2} L_i^{-1}$
2.	Rotta (1951)	kL_i
3.	Dissipation rate (Harlow and Nakayama, 1967)	$\varepsilon \propto k^{3/2} L_i^{-1}$
4.	Turbulence vorticity (Spalding, 1972)	$\varpi = kL_i^{-2}$

The transport equations for some of the above quantities can be obtained by manipulating Navier-Stokes equations with additional assumptions associated for each model. The general transport equation for all variables can be written as (Mathieu and Scott, 2000)

$$\underbrace{\frac{\partial Z}{\partial t}}_{\text{Rate of change}} + \underbrace{U_i \frac{\partial Z}{\partial x_i}}_{\text{Convection}} = \underbrace{\frac{\partial}{\partial x_i}\left(\frac{\sqrt{k} L_i}{\sigma_z}\frac{\partial Z}{\partial x_i}\right)}_{\text{Diffusion}} + \underbrace{c_{z1}\frac{Z}{k}P}_{\text{Production}} - \underbrace{c_{z2} Z \frac{\sqrt{k}}{L_i}}_{\text{Destruction}} + S, \tag{3.27}$$

where σ, c_{z1}, and c_{z2} are empirical constants, P is the production term and S is the secondary source term depending on the choice of Z. The different two-equation models can be presented as following:

a. STANDARD k-ε MODEL

The transport equations for the turbulent quantities are

$$\frac{D\rho k}{Dt} = \frac{\partial}{\partial x_j}\left[\left(\mu + \frac{\mu_t}{\sigma_k}\right)\frac{\partial k}{\partial x_j}\right] + \mu_t \frac{\partial U_i}{\partial x_j}\left(\frac{\partial U_i}{\partial x_j} + \frac{\partial U_j}{\partial x_i}\right) - 2\mu\left(\frac{\partial k^{1/2}}{\partial x_j}\right)^2 - \rho\varepsilon, \tag{3.28}$$

$$\left.\begin{aligned}\frac{D\rho\varepsilon}{Dt} = \frac{\partial}{\partial x_j}\left[\left(\mu + \frac{\mu_t}{\sigma_\varepsilon}\right)\frac{\partial \varepsilon}{\partial x_j}\right] + f_1 C_{\varepsilon 1}\mu_t \frac{\varepsilon}{k}\frac{\partial U_i}{\partial x_j}\left(\frac{\partial U_i}{\partial x_j} + \frac{\partial U_j}{\partial x_i}\right)\\ - C_{\varepsilon 2} f_2 \rho \frac{\varepsilon^2}{k} + \rho E\end{aligned}\right\}, \tag{3.29}$$

and the eddy viscosity is defined as

$$\nu_t = C_\mu f_\mu \frac{k^2}{\varepsilon} \tag{3.30}$$

where the model constants are given as

$$\left.\begin{aligned} C_\mu = 0.09 \quad \sigma_k = 1.0 \quad \sigma_\varepsilon = 1.3\\ C_{\varepsilon 1} = 1.44 \quad C_{\varepsilon 2} = 1.92\end{aligned}\right\}, \tag{3.31}$$

with the damping functions as

$$\left.\begin{aligned} f_\mu = f_1 = f_2 = 1 \\ E = 0 \end{aligned}\right\}. \tag{3.32}$$

b. LOW –REYNOLDS NUMBER k-ε MODELS

The standard k-ε model is formulated for high Reynolds number flows and it is not valid for near wall regions or interfaces where the viscous effects are comparable in magnitude to that of turbulence. Many attempts are made to modify the standard k-ε model to be applicable for low-Reynolds number regions by adjusting the damping functions introduced in the standard model (Jones and Launder 1973; Launder and Sharma, 1974; Lam and Bremhorst model, 1981; Chien, 1982; Yang and Shih, 1993; Fan *et al.*, 1993). Different versions of low-Reynolds number k-ε model have different values of damping functions f_μ , f_1, f_2 and E. Most of the damping functions depend on the dimensionless parameter $\mathrm{Re}_t = k^2/\nu\varepsilon$. For example, Jones and Launder (1973) low-Reynolds number model is one of these modifications. Jones and launder (1973) model differs from the standard k-ε model in the values/expressions of the damping functions f_μ, f_2, and E, as well as the constants $C_{\varepsilon 1}$ and $C_{\varepsilon 2}$, which are given as

$$f_\mu = \exp\left[-2.5/(1+\mathrm{Re}_t/50)\right], \tag{3.33}$$

$$f_2 = 1.0 - 0.3\exp(-\mathrm{Re}_t^2), \tag{3.34}$$

$$E = 2\nu\nu_t\left(\frac{\partial^2 U_i}{\partial x_j \partial x_i}\right)^2, \tag{3.35}$$

$$C_{\varepsilon 1} = 1.45 \quad C_{\varepsilon 2} = 2.0. \tag{3.36}$$

C. LOW-REYNOLDS NUMBER k-ω MODEL

The k-ω model is developed by Wilcox (1988) based on the original transport equation developed by Kolmogorov (1942) who proposed that the energy dissipation rate per unit of turbulence kinetic energy, ω, which has the dimension of $time^{-1}$, as an alternative to ε. The transport equations of k-ω are

$$\frac{D\rho k}{Dt} = \mu_t \frac{\partial U_i}{\partial x_j}\left[\frac{\partial U_i}{\partial x_j} + \frac{\partial U_j}{\partial x_i}\right] + \frac{\partial}{\partial x_j}\left[(\mu + \sigma_{k1}\mu_t)\frac{\partial k}{\partial x_j}\right] - \beta^* \rho\omega k, \tag{3.37}$$

$$\frac{D\rho\omega}{Dt} = \rho\gamma_1 \frac{\partial U_i}{\partial x_j}\left[\frac{\partial U_i}{\partial x_j} + \frac{\partial U_j}{\partial x_i}\right] + \frac{\partial}{\partial x_j}\left[(\mu + \sigma_{\omega 1}\mu_t)\frac{\partial \omega}{\partial x_j}\right] - \beta_1 \rho\omega^2. \tag{3.38}$$

The eddy viscosity is defined as

$$\nu_t = \alpha^* \frac{k}{\omega}. \tag{3.39}$$

The model constants for low-Reynolds number version are given by (Wilcox 1992) as

$$\alpha^* = \frac{\alpha_0^* + \mathrm{Re}_t / R_k}{1 + \mathrm{Re}_t / R_k}, \tag{3.40}$$

$$\gamma_1 = \frac{5}{9}\frac{\alpha_0 + \mathrm{Re}_t / R_\omega}{1 + \mathrm{Re}_t / R_\omega}(\alpha^*)^{-1}, \tag{3.41}$$

$$\beta^* = \frac{9}{100}\frac{5/18 + (\mathrm{Re}_t / R_\beta)^4}{1 + (\mathrm{Re}_t / R_\beta)^4}, \tag{3.42}$$

$$\left.\begin{array}{llll} \sigma_{k1} = \sigma_{\omega 1} = 0.5 & \beta_1 = 0.075 & \alpha_0^* = 0.025 & \alpha_0 = 0.1 \\ R_\beta = 8 & R_k = 6 & R_\omega = 2.7 & \mathrm{Re}_t = k/\omega\nu \end{array}\right\}. \tag{3.43}$$

d. k-ω BASELINE (BSL) MODEL

The k-ω model developed by Wilcox (1988) has the disadvantage of being highly sensitive to ω specified in the freestream. For this reason, Menter (1994) proposed the

k-ω baseline (BSL) model, which is basically a combination of the k-ω model to be used in the inner region of the boundary layer, and the standard k-ε to be used in the outer region as well as the free stream. Development of this model (the k-ε model is transformed into k-ω formulation) is made possible by introducing the blending function F_1. The blending function is unity near the wall and zero away from the wall. The difference between the BSL model and k-ω model comes essentially from the appearance of a cross-diffusion term in the ω-equation and also the values of the constants. The transport equations for the baseline model (Menter, 1994) are:

$$\frac{D\rho k}{Dt} = \mu_t \frac{\partial U_i}{\partial x_j}\left(\frac{\partial U_i}{\partial x_j} + \frac{\partial U_j}{\partial x_i}\right) + \frac{\partial}{\partial x_j}\left[(\mu + \sigma_k \mu_t)\frac{\partial k}{\partial x_j}\right] - \beta^* \rho \omega k \tag{3.44}$$

$$\left.\begin{aligned}\frac{D\rho\omega}{Dt} = \frac{\gamma}{\rho}\frac{\partial U_i}{\partial x_j}\left(\frac{\partial U_i}{\partial x_j} + \frac{\partial U_j}{\partial x_i}\right) + \frac{\partial}{\partial x_j}\left[(\mu + \sigma_\omega \mu_t)\frac{\partial \omega}{\partial x_j}\right] \\ - \beta\rho\omega^2 + 2\rho(1 - F_1)\frac{\sigma_{\omega 2}}{\omega}\frac{\partial k}{\partial x_j}\frac{\partial \omega}{\partial x_j}\end{aligned}\right\}. \tag{3.45}$$

The eddy viscosity is the same as the one used in the standard k-ω model (Eq. (3.39) with α^*=1). The inner region constants, which are similar to those of k-ω model (Wilcox, 1988) are:

$$\left.\begin{aligned}\sigma_{k1} = 0.5 \quad \sigma_{\omega 1} = 0.5 \quad \beta_1 = 0.0750 \\ \beta^* = 0.09 \quad \kappa = 0.41 \quad \gamma_1 = \beta_1/\beta^* - \sigma_{\omega 1}\kappa^2/\sqrt{\beta^*}\end{aligned}\right\}. \tag{3.46}$$

The constants for the outer region, which are those of the standard k-ε model, are given as:

$$\left.\begin{aligned}\sigma_{k2} = 0.5 \quad \sigma_{\omega 2} = 0.5 \quad \beta_2 = 0.0750 \\ \beta^* = 0.09 \quad \kappa = 0.41 \quad \gamma_{21} = \beta_2/\beta^* - \sigma_{\omega 2}\kappa^2/\sqrt{\beta^*}\end{aligned}\right\}. \tag{3.47}$$

The constants for the model employed for the inner region of the boundary layer, i.e., at the vicinity of the wall, denoted by a symbol φ_1, and the conditions for the model used to solve for in the outer region of the boundary layer as well as the freestream region, denoted by φ_2, are related together by a function that is called "blending function F_1". The latter provides the constants, φ, for the BSL model as

$$\varphi = F_1\varphi_1 + (1 - F_1)\varphi_2, \tag{3.48}$$

where

$$F_1 = \tanh\left(\arg_1^4\right), \tag{3.49}$$

and

$$\arg_1 = \min\left[\max\left(\frac{\sqrt{k}}{0.09\omega y}; \frac{500\nu}{y^2\omega}\right); \frac{4\rho\sigma_{\omega 2}k}{CD_{k\omega}y^2}\right] \tag{3.50}$$

The symbol y in Eq. (3.50) is the distance to the wall and $CD_{k\omega}$ is the positive portion of the cross-diffusion term in the ω-equation, i. e.,

$$CD_{k\omega} = \max\left[2\rho\frac{\sigma_{\omega 2}}{\omega}\frac{\partial k}{\partial x_j}\frac{\partial \omega}{\partial x_j}; 10^{-20}\right]. \tag{3.51}$$

e. k-ω SHEAR STRESS TRANSPORT (SST) MODEL

The shear stress transport (SST) model, which is developed by Menter (1994), is identical to the BSL model except that the inner region constants, φ_1, have the following values

$$\left.\begin{array}{llll} \sigma_{k1} = 0.85 & \sigma_{\omega 1} = 0.5 & \beta_1 = 0.0750 & a_1 = 0.31 \\ \beta^* = 0.09 & \kappa = 0.41 & \gamma_1 = \beta_1/\beta^* - \sigma_{\omega 2}\kappa^2/\sqrt{\beta^*} & \end{array}\right\}, \tag{3.52}$$

and the eddy viscosity is now defined as

$$\nu_t = \frac{a_1 k}{\max(a_1 \omega; \Omega F_2)}, \tag{3.53}$$

where Ω is the absolute value of vorticity, which is defined as

$$\Omega = \frac{\partial U_2}{\partial x_1} - \frac{\partial U_1}{\partial x_2}, \tag{3.54}$$

and F_2 is given by

$$F_2 = \tanh(\arg_2^2), \tag{3.55}$$

with

$$\arg_2 = \max\left(2\frac{\sqrt{k}}{0.09\omega y}; \frac{500\nu}{y^2\omega}\right). \tag{3.56}$$

3.6 FREESTREAM AND GAS-LIQUID INTERFACE CONDITIONS

The freestream mean-velocities, pressure and turbulence quantities are given the following values

$$U = U_\infty, \tag{3.57}$$

$$V = 0, \tag{3.58}$$

$$W = 0, \tag{3.59}$$

$$p = p_\infty, \tag{3.60}$$

$$k = k_\infty, \tag{3.61}$$

and

$$\varepsilon = \varepsilon_\infty \text{ or } \omega = \omega_\infty, \tag{3.62}$$

depending on the turbulence closure model being used.

The free stream value for k and ε are estimated from the following relations (Kral, 1998).

$$k_\infty = 1.5\left(I_\infty \times U_\infty\right)^2, \tag{3.63}$$

$$\varepsilon_\infty = c_\mu f_\mu \rho \frac{k_\infty^2}{\mu_{t\infty}} \mathrm{Re}, \tag{3.64}$$

$$\omega_\infty = \rho_\infty \frac{k_\infty}{\mu_\infty}\left(\frac{\mu_{t\infty}}{\mu_\infty}\right)^{-1} \tag{3.65}$$

where $\mu_{t\infty}$ is the freestream value of turbulent viscosity taken as $\mu_{t\infty} \cong (0.1-10)\mu_\infty$.

A distinctive gas-liquid interface exists at the droplet surface between the liquid-phase and its surrounding gas-phase. Conditions at this distinctive interface are obtained by coupling the conservation equations (momentum, energy and species equations) between the gas- and liquid-phases as follows

a) Shear stress continuity

$$\tau_{ij,g} = \tau_{ij,l} \tag{3.66}$$

b) Tangential velocity continuity

$$U_{\tan}\big|_g = U_{\tan}\big|_l = U_s \tag{3.67}$$

c) Normal velocity continuity

$$U_{nor}\big|_l = \left(\frac{\rho_g}{\rho_l}\right) U_{nor}\big|_g + \dot{r}\left(1 - \frac{\rho_g}{\rho_l}\right) \tag{3.68}$$

d) Temperature continuity

$$T_g = T_l = T_s \tag{3.69}$$

e) Energy conservation

$$\lambda_{eff} \frac{\partial T}{\partial x_i}\bigg|_g = \lambda \frac{\partial T}{\partial x_i}\bigg|_l + \dot{m}''_{evap} h_{evap} \tag{3.70}$$

f) Species conservation

$$\dot{m}''_{evap}\left(Y_{F,g}-1\right)-\rho_g D_{AB,g}\frac{\partial Y_{F,g}}{\partial x_i}=0 \tag{3.71}$$

g) Droplet mass conservation

$$\dot{r}=-\frac{\sum_{\substack{evaporated\\surfaces}}\dot{m}''_{evap,i}A_s}{4\pi\rho r^2}+\frac{r}{3\rho}\frac{d\rho}{dt} \tag{3.72}$$

In the above equations, the subscripts g and l denote the variables in the gas side and liquid side at the droplet interface, respectively. The symbol $\dot{r}$ denotes the regression rate of the droplet radius, where r is the instantaneous droplet radius and A_s is the surface area of each node at the droplet surface that is subjected to the flow. The last term in Eq. (3.72) represents the swelling of the droplet during its warming-up period.

3.7 WALL BOUNDARY CONDITIONS

The existence of a solid boundary (wall) induces considerable changes in the flow and turbulence structure as compared to the turbulent freestream away from the wall. Therefore, the flow conditions at the wall must be defined. The no-slip boundary conditions are used for velocities, however, zero gradients are used for pressure, temperature and fuel mass fraction as

$$U_w=V_w=W_w=0, \tag{3.73}$$

$$\frac{\partial p_w}{\partial n}=0, \tag{3.74}$$

$$\frac{\partial T_w}{\partial n}=0, \tag{3.75}$$

$$\frac{\partial Y_{F,w}}{\partial n}=0, \tag{3.76}$$

where n is the normal direction onto the wall.

For turbulence quantities, i.e., kinetic energy k, viscosity μ_t, dissipation ε, specific dissipation ω, and their values at the wall are set as follows (Kral, 1998; Menter, 1994)

$$k_w = 0, \tag{3.77}$$

$$\mu_{t,w} = 0, \tag{3.78}$$

$$\varepsilon_w = 0, \tag{3.79}$$

$$\omega_w = 800\frac{\mu_w}{\rho_w(\Delta y_1)^2}, \tag{3.80}$$

where Δy_1 is the distance to the next node away from the wall.

Chapter

4

SOLUTION ALGORITHM

The set of equations describing the gas- and liquid-phases subjected to the boundary conditions reported previously in Chapter 3 are solved numerically using the Finite-Volume scheme developed by Patankar (1980). The numerical solution is obtained by using a Cartesian grid based blocked-off technique. A brief review of the Blocked-off technique is given below. Detailed explanation of the treatment of a spherical object (a droplet or a sphere) in the calculation domain is also presented in this chapter. Finally, the computational domain and the grid generation are reported at the end of this chapter.

4.1. SOLUTION APPROACH

The aforementioned set of governing equations for the gas-phase and the liquid-phase may be conveniently written in a general transport equation form as

$$\underbrace{\frac{\partial}{\partial t}(\rho\Phi)}_{\substack{Transient\\ Term}}+\underbrace{\frac{\partial}{\partial x_j}(\rho U_i\Phi)}_{\substack{Convection\\ Term}}=\underbrace{\frac{\partial}{\partial x_j}\left\{\Gamma_\Phi\frac{\partial\Phi}{\partial x_j}\right\}}_{\substack{Diffusion\\ Term}}+\underbrace{S_\Phi}_{\substack{Source\\ Term}}, \tag{4.1}$$

where the general variable Φ may represent the mean value of the mass, velocity components (U, V or W), pressure p, temperature T, mass fraction of the evaporating fuel droplet Y_F or turbulence quantities (k, ε or ω). Γ_Φ represents an effective diffusion coefficient of the general variable Φ and S_Φ is the source term. This generalized equation contains four terms, i.e., transient, convection, diffusion and source terms. It is worth to mention that the source term includes all terms that are not explicitly accounted for in the first three terms of Eq. (4.1). Summary of the governing equations in the gas-phase and the liquid-phase in terms of Φ, Γ and S is given in Table 4.1.

In order to solve the complex nonlinear and strongly coupled set of governing transport equations, Finite-Volume approach (Patankar, 1980) with staggered grid is employed. The governing differential equations are integrated over discrete volumes resulting in a set of algebraic equations of the following general form

$$\underbrace{a_P\Phi_P}_{(1)}=\underbrace{a_E\Phi_E+a_W\Phi_W+a_N\Phi_N+a_S\Phi_S+a_T\Phi_T+a_B\Phi_B}_{(2)}+\underbrace{b_\Phi}_{(3)}, \tag{4.2}$$

where $a_p, a_E, a_W, a_N, a_S, a_T, a_B$ and b_Φ are coefficient, which are defined as:

$$a_p=a_E+a_W+a_N+a_S+a_T+a_B-S_P\Delta x\Delta y\Delta z, \tag{4.3}$$

$$b_\phi=S_C\Delta x\Delta y\Delta z, \tag{4.4}$$

$$a_E=\beta_e D_e+\dot{m}_e\alpha_e-\dot{m}_e/2, \tag{4.5}$$

Table 4.1 Summary of governing equations in terms of Φ, Γ_Φ and S_Φ

	Equation	Φ	Γ_Φ	S_Φ
Gas-phase	Continuity	1	0	0
	x-Momentum	U	$\mu+\mu_t$	$S_U = -\frac{\partial p}{\partial x} - \frac{2}{3}\frac{\partial}{\partial x_j}\left(\rho k + \mu_t \frac{\partial U}{\partial x}\right)\delta_{1j}$
	y- Momentum	V	$\mu+\mu_t$	$S_V = -\frac{\partial p}{\partial y} - \frac{2}{3}\frac{\partial}{\partial x_j}\left(\rho k + \mu_t \frac{\partial V}{\partial y}\right)\delta_{2j}$
	z-Momentum	W	$\mu+\mu_t$	$S_W = -\frac{\partial p}{\partial z} - \frac{2}{3}\frac{\partial}{\partial x_j}\left(\rho k + \mu_t \frac{\partial W}{\partial z}\right)\delta_{3j}$
	Energy	T	$\mu + \mu_t/\mathrm{Pr}_t$	0
	Fuel mass fraction	Y_F	$\mu + \mu_t/Sc_t$	0
	Turbulence kinetic energy (k-ε) model	k	$\mu + \mu_t/\sigma_k$	$S_k = \mu_t \frac{\partial U_i}{\partial x_j}\left(\frac{\partial U_i}{\partial x_j} + \frac{\partial U_j}{\partial x_i}\right) - 2\mu\left(\frac{\partial k^{1/2}}{\partial x_j}\right)^2 - \rho\varepsilon$
	Turbulence dissipation rate	ε	$\mu + \mu_t/\sigma_\varepsilon$	$S_\varepsilon = f_1 C_{\varepsilon 1}\mu_t \frac{\varepsilon}{k}\frac{\partial U_i}{\partial x_j}\left(\frac{\partial U_i}{\partial x_j} + \frac{\partial U_j}{\partial x_i}\right) - C_{\varepsilon 2} f_2 \rho \frac{\varepsilon^2}{k} + \rho E$
	Turbulence kinetic energy (k-ω) model	k_1	$\mu + \mu_t\sigma_{k1}$	$S_{k1} = \mu_t \frac{\partial U_i}{\partial x_j}\left[\frac{\partial U_i}{\partial x_j} + \frac{\partial U_j}{\partial x_i}\right] - \beta^* \rho\omega k$
	Turbulence specific dissipation rate (k-ω) model	ω	$\mu + \mu_t\sigma_{\omega 1}$	$S_\omega = \rho\gamma_1 \frac{\partial U_i}{\partial x_j}\left[\frac{\partial U_i}{\partial x_j} + \frac{\partial U_j}{\partial x_i}\right] - \beta_1 \rho\omega^2$
Liquid-phase	Continuity	1	0	0
	x-Momentum	U_l	μ_l	0
	y- Momentum	V_l	μ_l	0
	z-Momentum	W_l	μ_l	0
	Energy	T_l	μ_l/Pr_l	0

$$a_W = \beta_w D_w + \dot{m}_w \alpha_w + \dot{m}_w / 2, \tag{4.6}$$

$$a_N = \beta_n D_n + \dot{m}_n \alpha_n - \dot{m}_n / 2, \tag{4.7}$$

$$a_S = \beta_s D_s + \dot{m}_s \alpha_s + \dot{m}_s / 2, \tag{4.8}$$

$$a_T = \beta_t D_t + \dot{m}_t \alpha_e - \dot{m}_t / 2, \tag{4.9}$$

$$a_B = \beta_b D_b + \dot{m}_b \alpha_b + \dot{m}_b / 2. \tag{4.10}$$

The subscripts E, W, N, S, T and B refer to centers of the neighborhood control volumes, i.e., east, west, north, south, top and bottom, respectively, with respect to the central control volume P, as illustrated in Figure 4.1. Subscripts e, w, n, s, t and b refer to east, west, north, south, top and bottom faces of the central control volume P, respectively, as illustrated in Figure 4.2. S_P and S_C are the coefficients of the linearized source term, i.e., $S_\Phi = S_C + S_P \Phi$ and f_i is the ratio of the neighborhood control volume length to the total length of neighborhood and central control volumes in x, y or z direction, where $f = 0.5$ if the grid is uniform.

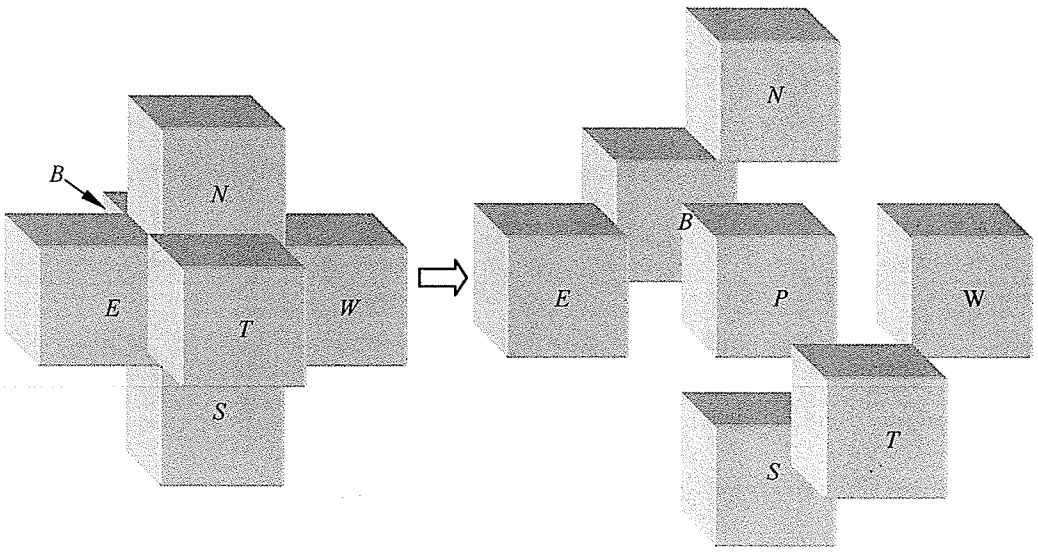

Figure 4.1 Central control volume P with its neighborhood control volumes

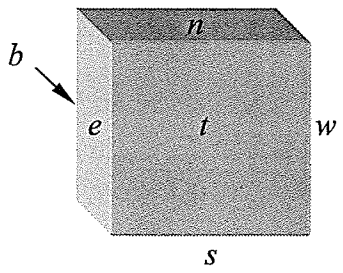

Figure 4.2 Faces of the central control volume P

The general diffusion conductance D, the general diffusion coefficient Γ, the parameter f, the convection weighting factor α, and the diffusion weighting factor β in Eqs. (4.6-4.10) are defined as follow

$$D_i = 2\Gamma_i A_i / (\Delta x_I + \Delta x_P), \tag{4.11}$$

$$\Gamma_i = \Gamma_P \Gamma_I / [\Gamma_I \Gamma_P + (1 - f_i)\Gamma_I], \tag{4.12}$$

$$f_i = \frac{(\Delta x_j)_I}{(\Delta x_j)_I + (\Delta x_j)_P}, \tag{4.13}$$

$$\alpha_i = \frac{1}{2} \times \frac{(Pe)_i^2}{5 + (Pe)_i^2}, \tag{4.14}$$

$$\beta_i = \frac{1 + 0.005(Pe)_i^2}{1 + 0.05(Pe)_i^2}, \tag{4.15}$$

where $\Delta x_j = \Delta x$ for j=1, Δy for j=2 and Δz for j=3, respectively. Subscripts I and i in Eqs. (4.11-4.15) denotes E, W, N, S, T or B and e, w, n, s, t or b, respectively. Finally, Pe stands for Peclet number which is defined as

$$(Pe)_i = \frac{\dot{m}_i}{D_i}, \tag{4.16}$$

where $\dot{m}$ is the mass flow rate. Complete derivation of the previous equations (i.e., Eqs. 4.2 through 4.15) is provided in Appendix A.

The absence of an explicit equation for pressure when working numerically with the so-called primitive variables U, V, W and p, presents an obstacle which is overcome by using the SIMPLEC approach (Van Doormall and Raithby, 1984). This approach allows developing an expression in the form of Eq. (4.2) for the pressure through a combination of the continuity and momentum equations. The objective is to develop a pressure field such that the resulting velocity field satisfies the continuity equation for every control volume in the calculation domain. The solution of the set of linearized algebraic equations, which are resulted from the application of Eq. (4.2) to each control volume in the computational domain, is accomplished by using a three-dimensional Strongly Implicit Procedure (SIP) developed by Leister and Perić (1991). The Strongly Implicit Procedure is chosen as a solver because it takes less number of iterations for convergence compared to other solvers, such as point Successive Over Relaxation (SOR) or Line Successive Over Relaxation (LSOR). Details of SIP, SOR and LSOR procedures are presented in Appendix B.

The iterative procedure, shown in Figure 4.3, sweeps the solution domain which includes gas- and liquid-phases until either the assigned maximum number of iterations is exceeded or the range-normalized relative errors (Eq. (4.17)) of the diffusion parameters (U, V, W, p, k, and ε or ω) are satisfied for each control volume.

$$\left| \frac{\Phi^{n+1} - \Phi^{n}}{\Phi_{max} - \Phi_{min}} \right| \leq \Theta_{\Phi}, \tag{4.17}$$

where Φ^{n+1} and Φ^{n} are the new and old values of the diffusion parameter Φ. Φ_{max} and Φ_{min} are the maximum and minimum value for the entire Φ^{n+1} field and Θ_{Φ} is taken to be 10^{-4} for all quantities.

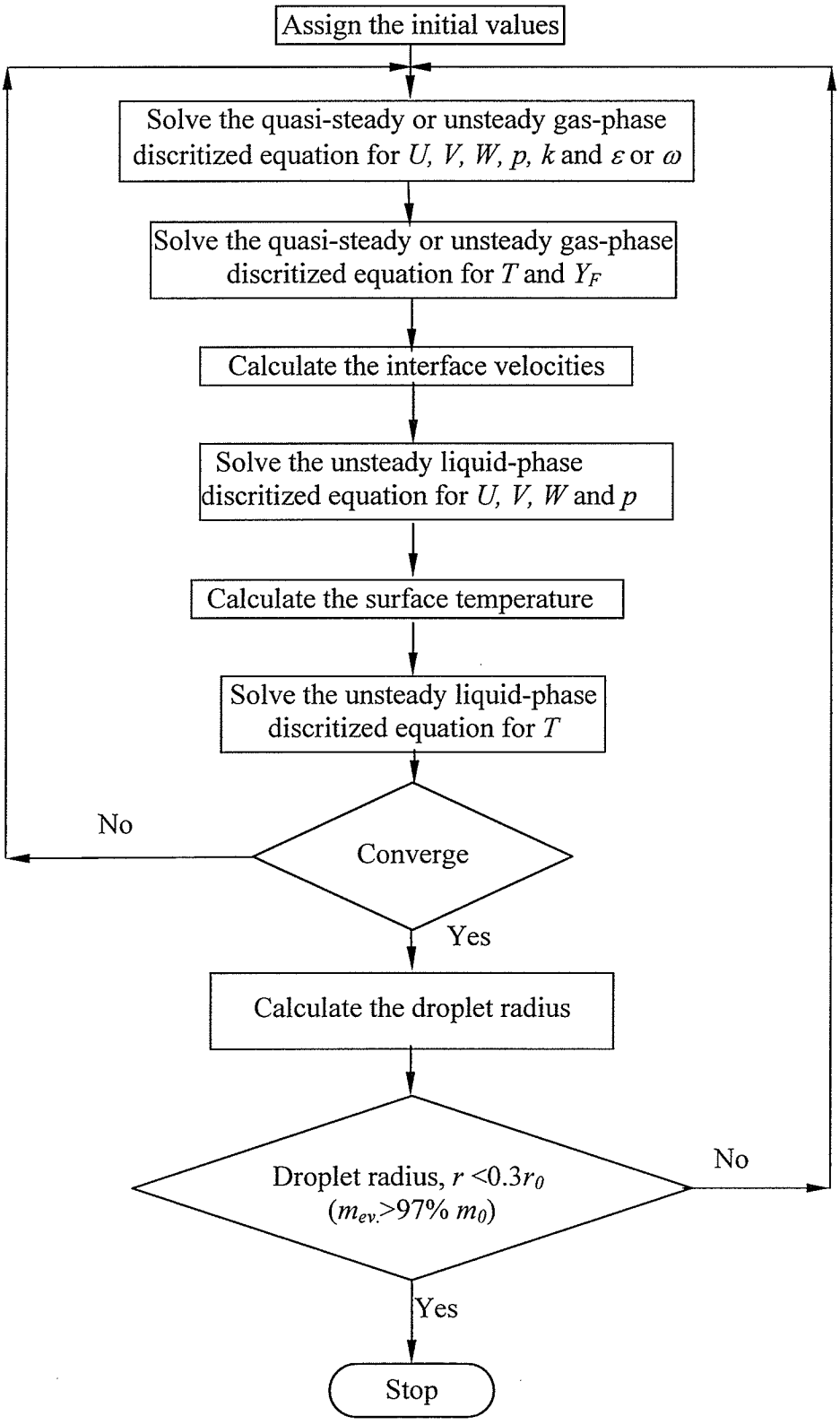

Figure 4.3 Iterative procedure for solving both the gas-phase and liquid-phase governing equations

4.2 BLOCKED-OFF TECHNIQUE

The difficulty in developing a 3D numerical code lies in the creation of a computational grid especially in spherical coordinates. Attempts are made to overcome this difficulty which include, for example, an approach that enables transforming the Navier-Stokes equations to general coordinates (ξ, η, and ζ) so that the Cartesian grid can be employed (Drikakis, 1995; Johnson ,1996; Constantinescu *et al.*, 2004; Niazmand and Renksizbulut, 2005). This approach makes the discretization process more difficult. Immersed-boundary fitted approach has also been employed (Kim *et al.* 2001), which consists of introducing a body in the flow field of interest. This virtual body is accounted for by adding an additional term of momentum forcing into Navier-Stokes equations and therefore the flow over a complex geometry can be handled by using orthogonal grids (Cartesian or Cylindrical). Another different approach, which is called "blocked-off", consists of using a calculation domain that includes both the gas- and liquid (or solid) - phases regions, but with the possibility of blocking off the control volumes of an inactive region (for example, a sphere in a flow computational domain). The blocking-off approach is first developed by Patankar (1978, 1991) to solve for conjugate heat transfer problems in a duct with curvilinear geometries. Then, it has been successfully applied to solve radiative heat transfer problems in irregular geometries by using Cartesian coordinates. These radiative heat transfer studies dealt with two-dimensional problems (Chai *et al.*, 1993; Kim *et al.*, 2001; and Byun *et al.*, 2003), and three-dimensional problems (Coelho *et al.*, 1998; Borjini *et al.*, 2003; and Consalvi *et al.*, 2003). Recently, this technique has been used in medical studies (Zhou *et al.*, 2004) dealing with three-

dimensional light and heat transport in several typical tissue domains with either one single blood vessel or two countercurrent blood vessels running through.

The blocked-off technique is adopted in the present study because of its ease of implementation, simplicity, and ease of grid generation compared to unstructured or multi-block grid generation. To the best knowledge of the author, this approach has never been used to solve for a flow over a spherical object (Abou Al-Sood and Birouk, 2005a, 2005b and 2005c; Birouk and Abou Al-Sood, 2006).

4.3 TREATMENT OF A DROPLET (OR A SPHERE) IN THE CALCULATION DOMAIN

This section describes the manner in which an embedded body, i.e., a droplet (or a sphere), is treated in the computational domain by the blocked-off procedure. For the case of a flow over a sphere, the treatment is achieved by blocking-off the control volumes that form the embedded body (i.e., sphere) so that the remaining active control volumes form the desired domain (i.e., the surrounding gas-phase). The Cartesian-based blocked-off treatment of an embedded body immersed in the computational domain is schematically shown in Figure 4.4. Using the blocked-off technique for an evaporating droplet in the air requires switching the active and inactive control volumes between the gas (surrounding)-phase and liquid-phase. For instance, when solving for the gas-phase, the control volumes forming the liquid-phase (droplet) are inactive (blocked) and those forming the gas-phase are active. Likewise, when solving for the liquid-phase, the control volumes forming the droplet are active and those of the gas-phase are inactive. When solving for the active control volumes the predefined diffusion parameters $\Phi_{p,desired}$ (see

Eq. (4.18)) in the inactive control volumes preserve their values before they become inactive. The simplest way in which the desired values of these parameters could be obtained in the inactive control volumes is by assigning a large source term in the discritized equation. That is setting S_C and S_P in Eqs. (4.3) and (4.4) for the inactive zone as follows

$$S_C = 10^{30}\Phi_{P,desired}, \tag{4.18}$$

$$S_P = -10^{30}, \tag{4.19}$$

where 10^{30} is a number large enough so that the other terms in the discritized equation, i.e., terms denoted by number 2 in Eq. (4.2), become negligible. Therefore, Eq. (4.2) becomes

$$S_C + S_P\Phi_P = 0\ , \tag{4.20}$$

and hence

$$\Phi_P = -S_C/S_P = \Phi_{P,desired}\ . \tag{4.21}$$

Although the computation is performed over the entire domain, only the solution within the active control volumes is meaningful. Note that this technique makes the surface of a droplet (or a sphere) looks like stair steps as illustrated in Figure 4.4. This approximation induces some calculation errors which can be minimized by using a very fine grid in the droplet domain.

4.4 SOLUTION PROCEDURE

The calculation domain, which is a cube of $32r_0$ x $32r_0$ x $32r_0$, where r_0 is the sphere (or droplet) radius, is divided into several control volumes and the droplet (or sphere) is

fixed at the center of the cube. This choice is based on the suggestions made by Sundararajan and Ayyaswamy (1984) who pointed out that the freestream inflow and boundary conditions must be taken at a distance from the center of the sphere that is at least ten times greater than the sphere radius. Figure 4.5 summarizes the computational domain and boundary conditions as the left and right faces are inflow and outflow boundary conditions, respectively, whereas the remaining faces are taken as the wall boundary conditions. In the present analysis, the Cartesian grid in the calculation domain consists of 60×60×60. Since the gradients around the sphere are large, a very fine grid, 40×40×40 is used in the domain of $4r$, i.e., $2r$ from the sphere (or droplet) center in all directions, as shown schematically in Figure 4.6. This number of grids is found to be the optimum number that provides stable results with an acceptable computational time. Coarser grids, such as 40×40×40 for the entire calculation domain and 30×30×30 for the domain of $4r$ are also tested. To eliminate the dependence of the results on the chosen grid, very fine grids are also tested such as, for example, 80×80×80 for the entire computation domain and 50×50×50 for the $4r$ domain. For example, at Re =100 and I_∞ =0 (laminar flow) the predicted sphere drag coefficient, is found lower than its experimental counterpart's by about 20% when using the coarser grid. Whereas the result is that the sphere drag coefficient changes by less than 3% compared with its counterpart's calculated by using the optimum grid employed in this study. Moreover, the computational time is extremely long for this finer grid. A summary of the sensitivity of the present model predictions to the chosen grid is given in Table 4.2. Note that Figure 4.6 does not show the complete computational grid but only an illustration to provide a

general idea. The same figure shows that the uniform grid is fine in the *4r* region, which is twice the size of the sphere, and coarser outside this region.

Table 4.2 Grid sensitivity to the present model predictions

		Domain	Grid		
		$32r_0$ (see Fig. 4.6)	40×40×40	60×60×60	80×80×80
		4r (see Fig. 4.6)	30×30×30	40×40×40	50×50×50
Sphere drag coefficient, C_D	Laminar flow (Re=100)		1.3547 (19.23%)	1.1384 (-----)*	1.1099 (2.50%)
	Turbulent flow (k-ε model) (Re=100, I_∞=20%)		1.4912 (24.20%)	1.2006 (-----)	1.2731 (6.04%)
	Turbulent flow (SST model) (Re=100, I_∞=20%)		2.1147 (82.09%)	1.1614 (-----)	1.1882 (2.31%)
Droplet Evaporation rate, K (mm^2/s)	k-ε model (T_∞=300 K, U_∞= 1m/s, I_∞=20%)		0.2084 (25.43)	0.1688 (-----)	0.1712 (1.72%)
	SST model				
	▪ (T_∞=300 K, U_∞= 2m/s, I_∞=20%)		0.2292 (23.62%)	0.1854 (-----)	0.1884 (1.62%)
	▪ (T_∞=773 K, U_∞= 2m/s, I_∞=20%)		2.1742 (22.25%)	1.7785 (-----)	1.8000 (1.21%)
	▪ (T_∞=1273 K, U_∞= 2m/s, I_∞=20%)		2.7649 (23.67%)	2.2357 (-----)	2.2562 (0.92%)

* Error is based on the optimum grid (60×60×60 in the whole domain with 40×40×40 in the *4r* domain)

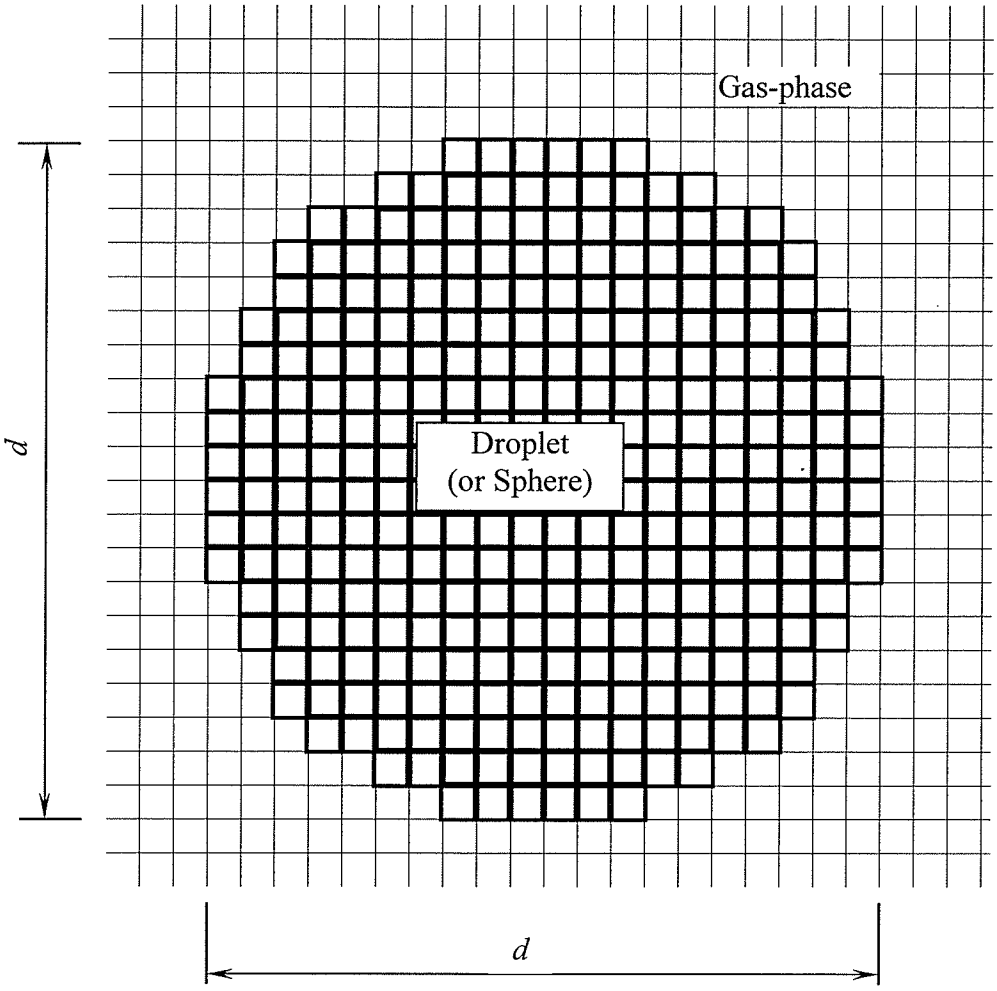

Figure 4.4 The Cartesian-based blocked-off treatment of a spherical object (a droplet or a sphere) immersed in the computational domain

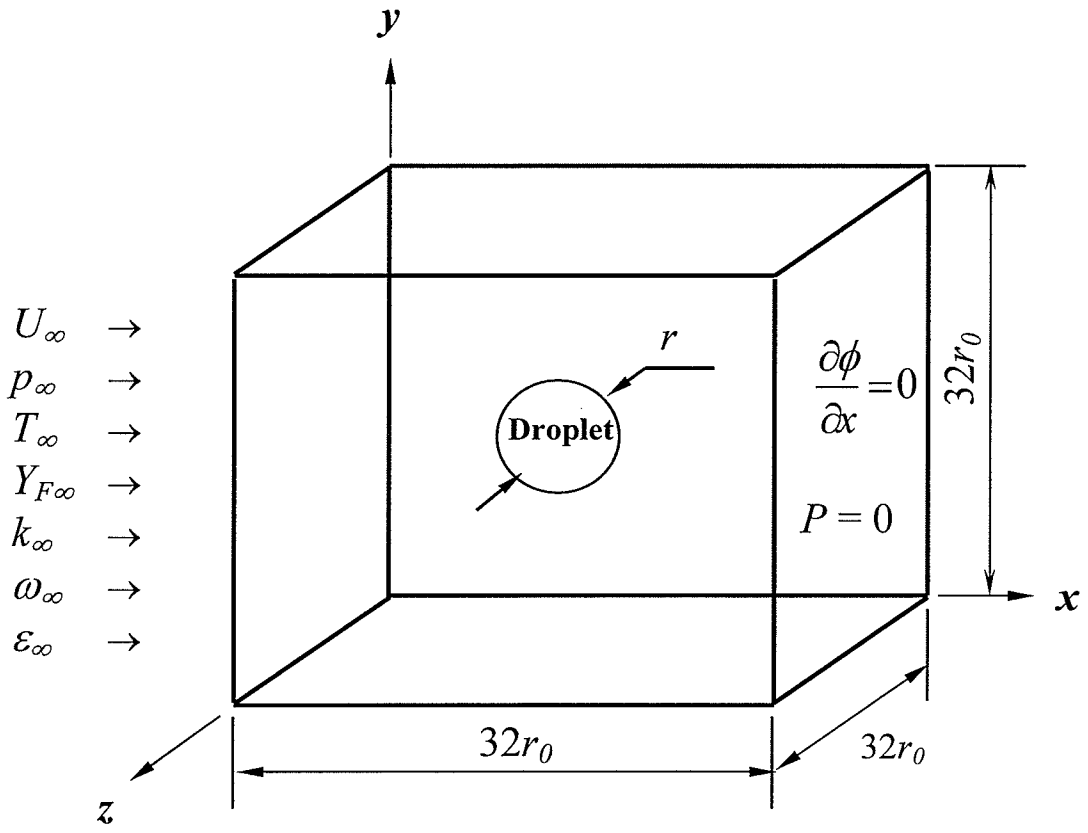

Figure 4.5 Illustration of the computational domain and boundary conditions for a flow over a droplet (or a sphere)

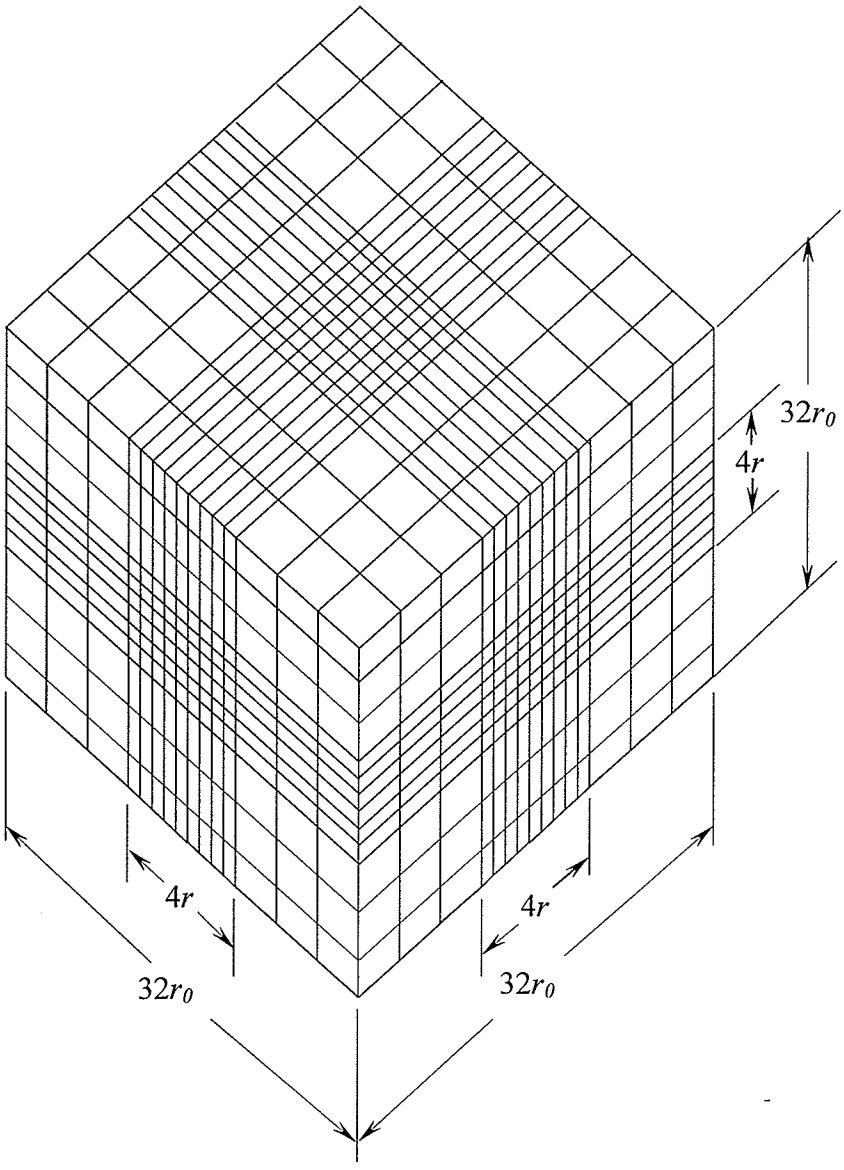

Figure 4.6 Schematic diagram of the computational grid

Chapter

5

RESULTS AND DISCUSSIONS

5.1 INTRODUCTION

This chapter is composed of two main parts. The first part concerns the effect of freestream turbulence on sphere drag coefficient and, the second part deals with freestream turbulence effect on the evaporation of a single fuel droplet. Four different eddy-viscosity turbulence closure models are tested for studying sphere drag coefficient. These models are: low-Reynolds-number k-ε model (Jones and Launder, 1973), low-Reynolds-number k-ω model (Wilcox, 1988), as well as BSL and SST blended k-ε/k-ω models (Menter, 1994). However, only two turbulence models, i.e., low-Reynolds-number k-ε and SST models, are employed for studying the effect of turbulence on the droplet evaporation at standard temperature and pressure conditions (Abou Al-Sood and Birouk, 2006a). Whereas only SST model is used for investigating the effect of

turbulence on the droplet evaporation in hot freestream conditions (Abou Al-Sood and Birouk, 2006c).

5.2 SPHERE DRAG COEFFICIENT

Calculations of the drag coefficient of a sphere are performed for Reynolds number in the range between 10 and 250. Although the main results presented in this section concern the numerical predictions of the mean drag coefficient of a sphere exposed to a turbulent freestream, results of the drag coefficient of a sphere exposed to a laminar freestream are also presented to demonstrate the successfulness of the numerical model developed here and particularly the blocked-off technique. The pressure coefficient at the centre and shear stress at the surfaces of each active (i.e., not blocked) control volume that is exposed to the flow are calculated. The local values of these two parameters are transformed from Cartesian coordinates into spherical coordinates. The mean drag coefficient is then calculated by integrating the wall pressure and shear stress coefficient over the surface area of the sphere as

$$C_D = \underbrace{\int_0^{\pi} C_p \sin(2\phi) d\phi}_{C_{D,p}} + \underbrace{\frac{1}{\rho U_\infty^2} \int_0^{\pi} \tau_w (1-\cos(2\phi)) d\phi}_{C_{D,f}}, \tag{5.1}$$

where ϕ is the azimuthal angle, and C_p and τ_w are the local wall pressure coefficient and shear stress, respectively, which are defined as

$$C_p = \frac{p - p_\infty}{\frac{1}{2}\rho U_\infty^2}, \tag{5.2}$$

$$\tau_w = \mu \left(\frac{\partial U_i}{\partial x_j} + \frac{\partial U_j}{\partial x_i} \right) + \frac{2}{3} \left(\frac{\partial u_j}{\partial x_j} \right) \delta_{ij}. \tag{5.3}$$

An important challenge that is raised when using Cartesian grid for a flow over a droplet (or a sphere) is the calculation of its surface area. Since the blocked-off technique does not reproduce the exact shape of the droplet/sphere, it is important to ensure that the surface area generated by using this technique matches approximately the real droplet/sphere surface (within an acceptable calculation error).

5.2.1 SPHERE DRAG COEFFICIENT IN A LAMINAR FLOW

Figure 5.1 displays a comparison between the wall pressure coefficient predicted by the present numerical model and those found by Johnson (1996) and Kim *et al.* (2001) who both employed different numerical techniques. The comparison made in Figure 5.1, for a typical Reynolds number of 100, shows a slight difference between the present data and those of the aforementioned authors. The difference occurred particularly between two azimuthal positions along the periphery of the sphere, i.e., between 30° and 70° and, between 100° and 150°, respectively. Within these regions the maximum difference between the present predictions and the published results quoted in Figure 5.1 is less than around 10% which might be attributed to computational error. Nevertheless, the comparison in this figure overall shows fair agreement between the results of the present predictions and those of Johnson (1996) and Kim *et al.* (2001). Figure 5.2 shows the variation of the wall pressure coefficient over the sphere for various Reynolds numbers, *Re*, ranging between 20 and 250. This figure shows clearly that the sphere wall pressure coefficient, $C_{p,}$ increases with increasing Reynolds number. The increase in C_p occurs particularly in the regions around the sphere between two azimuthal angles, i.e., 45° and 180°, which may be considered as the wake region of the sphere. The variation of the predicted sphere drag coefficient with Reynolds number, which is based on the

freestream velocity and sphere diameter, is plotted in Figure 5.3, which shows also a comparison with the experimental drag coefficient† results found by Roos and Willmarth (1971). The comparison made in Figure 5.3 clearly demonstrates an excellent agreement between the present results and the experimental results of Roos and Willmarth (1971) within experimental and numerical errors.

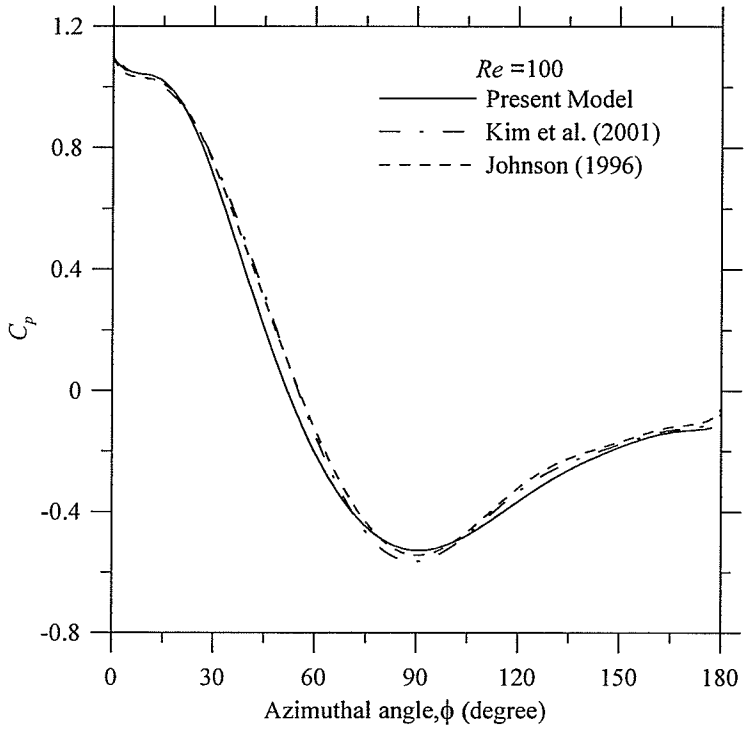

Figure 5.1 Comparison of the predicted local wall pressure coefficient against published numerical data for a typical Reynolds number

† It is also called sphere "standard drag coefficient"

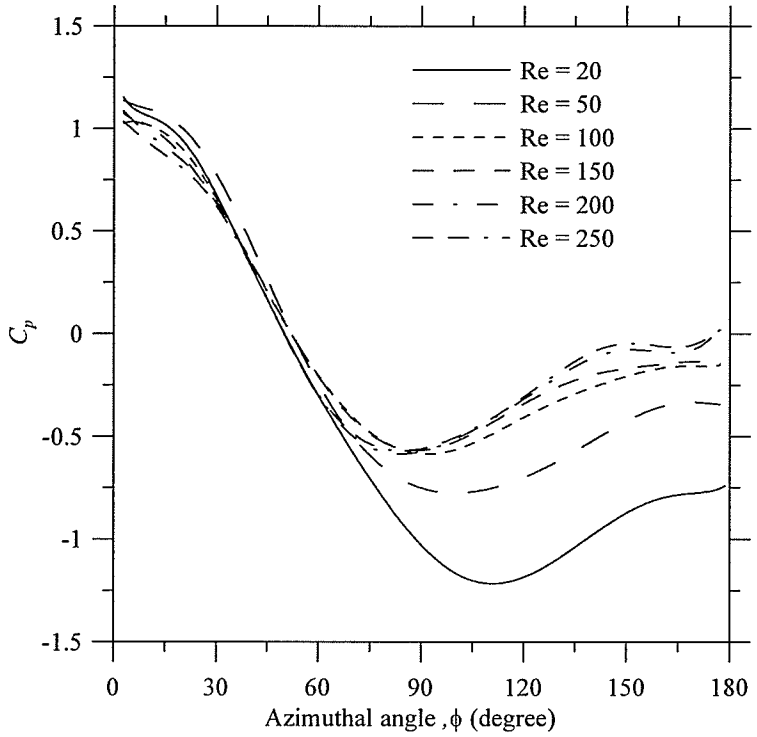

Figure 5.2 Variation of the predicted wall pressure coefficient around the sphere for different Reynolds numbers

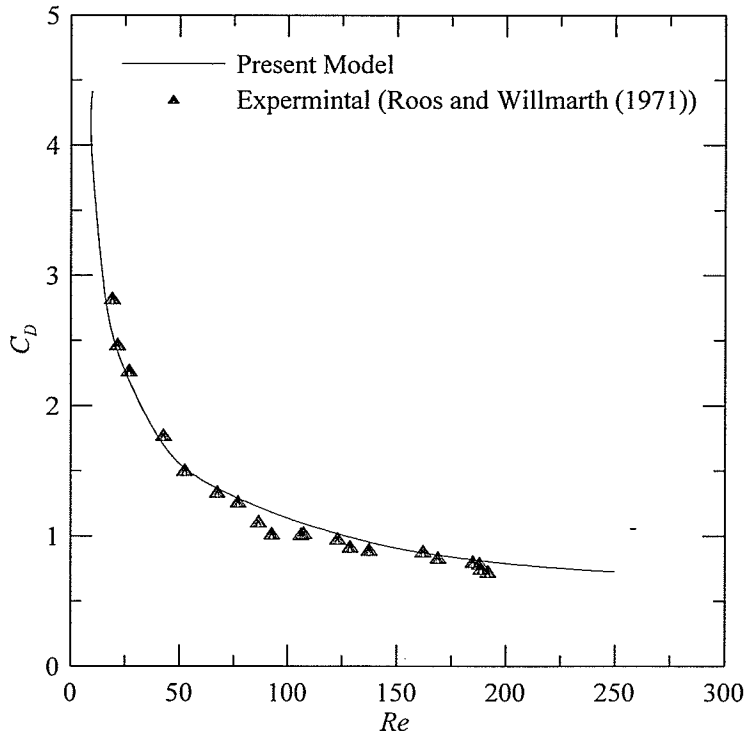

Figure 5.3 Comparison of the predicted drag coefficient of a sphere exposed to a laminar freestream of air against its counterpart's experimental published data for various Reynolds numbers

5.2.2 SPHERE DRAG COEFFICIENT IN A TURBULENT FLOW

The freestream Reynolds number and turbulence intensity are varied from 10 up to 250 and, from 0% up to 60%, respectively. The freestream turbulence intensity is defined as $I_\infty = u'_\infty / U_\infty$ and, Reynolds number is based on the sphere diameter and air freestream mean-velocity upstream of the sphere, U_∞. Figure 5.4 shows 2D contours of the pressure coefficient of a sphere exposed to a turbulent freestream for a typical Reynolds number and freestream intensity (i.e., Re=186 and I_∞ = 60%). Figure 5.5 displays a typical variation of the wall pressure coefficient calculated by using Menter's SST turbulence closure model for a typical Reynolds number of 100 and three typical turbulence intensity values, i.e., 10%, 30% and 60%. Figure 5.5 shows that the variations of the wall pressure coefficient versus the azimuthal position remain practically the same when varying the freestream turbulence intensity from 10% up to 60%. Figures 5.6 and 5.7 show the variation of the sphere drag coefficient versus turbulence intensity for three typical Reynolds number values, i.e.,, 10, 50 and 100. The drag coefficient results predicted by using only two different turbulence closure models are presented as examples in Figures 5.6 and 5.7. These figures show that, regardless of the closure model used, turbulence intensity does not seem to affect the drag coefficient for any given freestream Reynolds number explored here. Therefore the sphere drag coefficient should collapse on the "laminar" standard drag coefficient curve independently of the freestream turbulence intensity. This is clearly shown with the Menter's SST model as illustrated in Figure 5.7. This corroborate with the suggestions of Warnica *et al.* (1995b) and Bagchi and Balachandar (2003), who investigated this flow problem and found that the freestream turbulence intensity does not affect significantly the drag coefficient of a particle (or

sphere) within the range of flow conditions explored in the present study. However, it is differing in the case of Jones and Launder model as shown in Figure 5.6, which is also the case for the two other tested turbulence closure models; low-Reynolds-number k-ω and BSL model.

Figure 5.8 shows a comparison between the sphere drag coefficient predicted by using four different turbulence closure models, which are the low-Reynolds-number k-ω model, BSL and SST blended k-ε/k-ω models and, low-Reynolds-number k-ε model. These predictions display two interesting observations as can be seen in Figure 5.8. The first one is that all the four closure models predict the same value of the sphere drag coefficient in the range of Reynolds number between $100 < Re < 250$ within numerical error. The second observation concerns the range of Reynolds number below 100. Within this Reynolds number range the low Reynolds k-ε model predicts relatively the highest drag coefficient followed by the low Reynolds k-ω model and then the BSL model of Menter for which all the results obtained with these models do not collapse on the laminar "standard drag coefficient" curve. However, only the predictions obtained by using Menter SST Model agree with laminar experimental results (i.e., the standard drag coefficient). Thus, the Menter's SST model predicts the best results as specified by our foregoing consideration in the previous paragraph. The results of the sphere drag coefficient in the Reynolds number range up to 100 have been magnified in Figure 5.9 to make clear the results discussed above. This suggests that contrary to the SST model of Menter, the three turbulence models, which are the low Reynolds k-ε and k-ω models as well as the BSL model, are incapable of predicting satisfactory the sphere "standard" drag coefficient in the Reynolds number range below approximately 100.

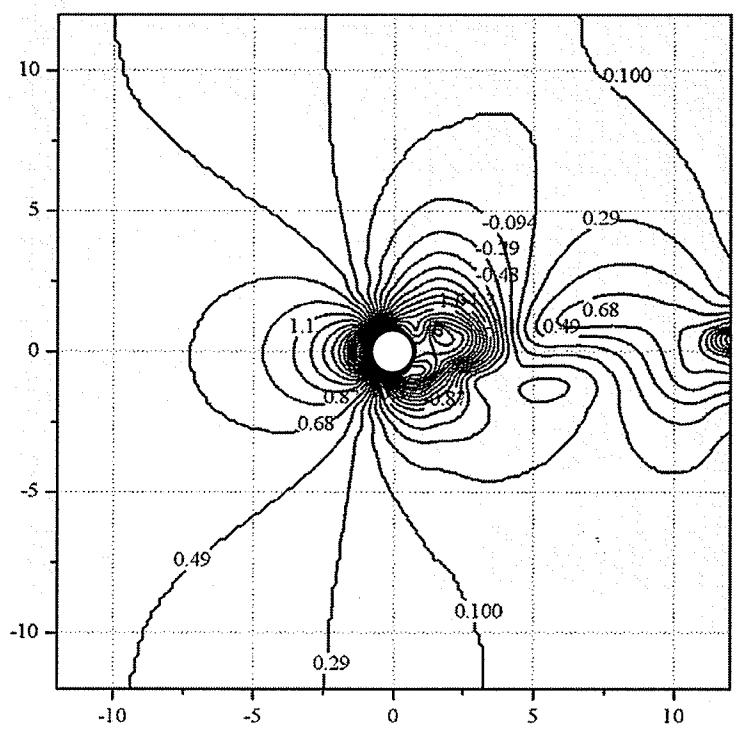

Figure 5.4 SST model based predictions of pressure coefficient contours in the x-y plane for Re=186 and $I_\infty = 60\%$

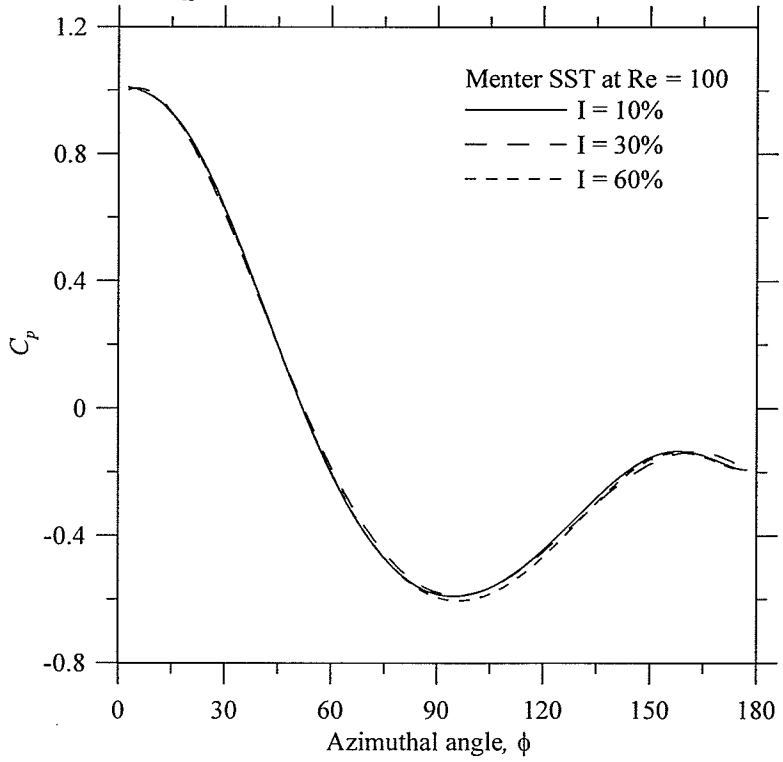

Figure 5.5 Variation of the local wall pressure coefficient around the sphere for various freestream turbulence intensities and a typical Reynolds number

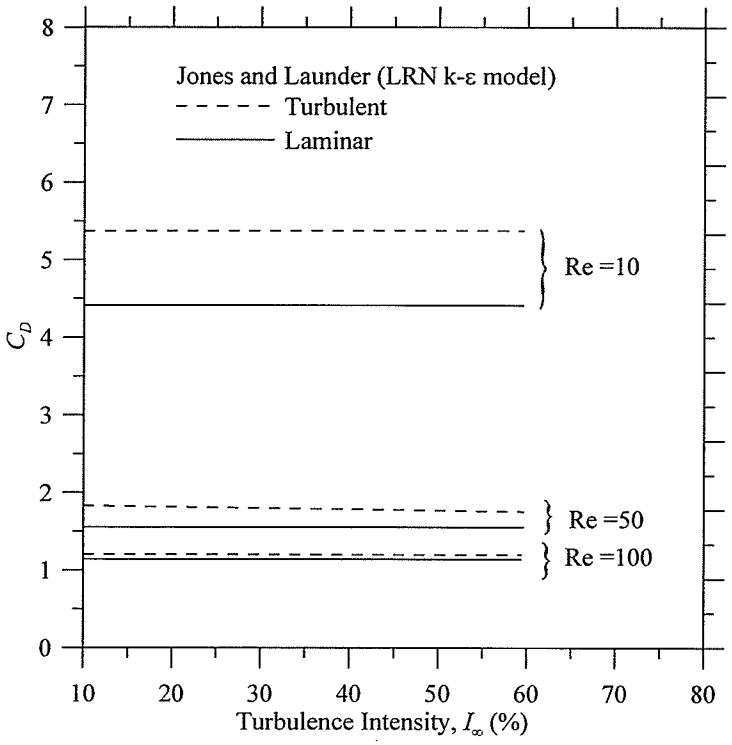

Figure 5.6 Variation of the laminar and turbulent (based on LRN k-ε model) predicted drag coefficient versus the freestream turbulence intensity for different Reynolds numbers

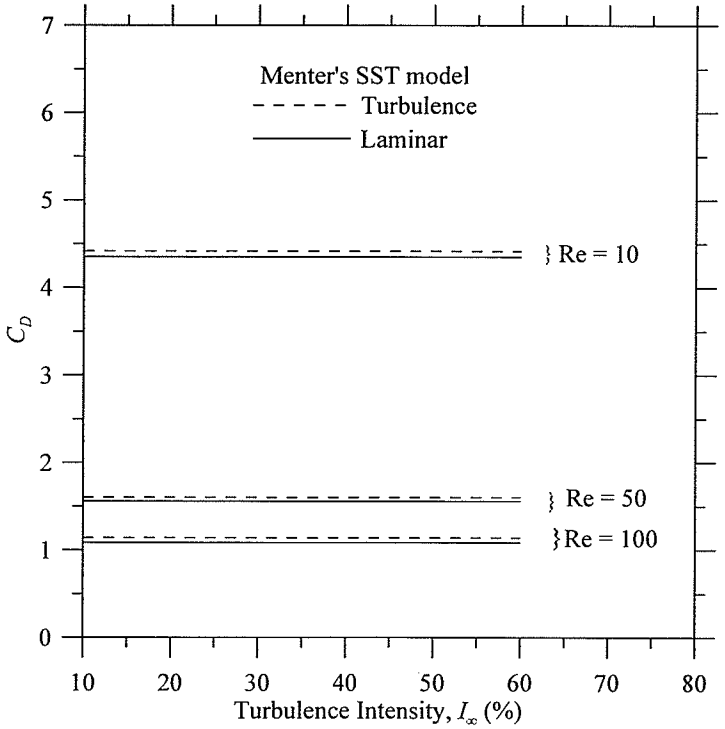

Figure 5.7 Variation of the laminar and turbulent (based on Menter's SST model) predicted drag coefficient versus the freestream turbulence intensity for different Reynolds numbers

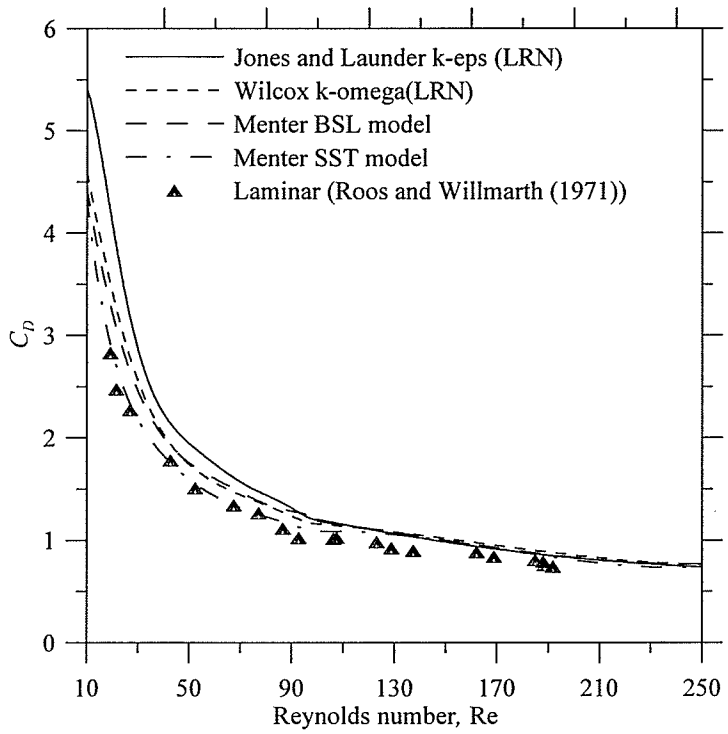

Figure 5.8 Comparison of the sphere drag coefficient predicted by using different turbulence closure models against its counterpart experimental laminar "standard" drag in the Reynolds number range between 10 and 250

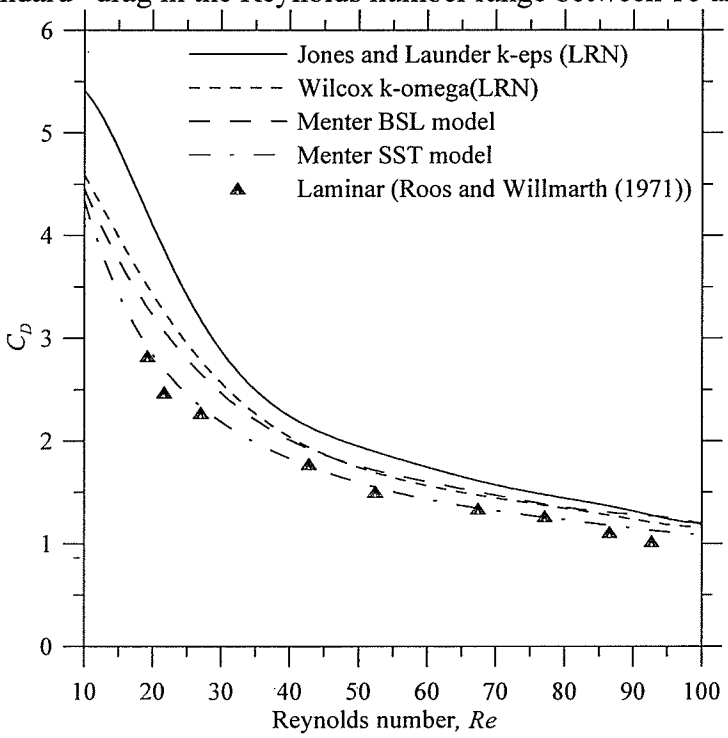

Figure 5.9 Magnification of the comparison presented in Figure 5.8 for Reynolds number ranging between 10 and 100

5.3 FREESTREAM TURBULENCE EFFECT ON THE EVAPORATION OF A DROPLET

The test conditions employed in the present study are limited to those reported in Table 5.1. Some of the test conditions are deliberately chosen to enable comparing with published data. The formula employed to calculate the thermodynamic properties of *n*-heptane and *n*-decane droplets, as well as the air-vapor mixture are reported in Appendix C.

Table 5.1 Test conditions

Flow	Test no.	$d_0(mm)$	$U_\infty(m/s)$	I_∞ (%)	p_∞ (atm)	$T_\infty(K)$	Re_∞
Laminar	(1)	1.50	0.6	0	1	300	56
	(2)	1.50	1.0	0	1	300	93
	(3)	1.50	2.0	0	1	300	186
	(4)	1.18	6.0	0	1	297	440
	(5)	1.50	2.0	0	1	363	136
	(6)	1.50	2.0	0	1	400	116
	(7)	1.50	2.0	0	1	773	39
	(8)	1.96	1.0	0	1	1000	17
	(9)	1.50	2.0	0	1	1273	17
Turbulent	(1)-(12)	1.50	0.6	5-60*	1	300	56
	(13)-(24)	1.50	1.0	5-60	1	300	93
	(25)-(36)	1.50	2.0	5-60	1	300	186
	(37)-(48)	1.50	2.0	5-60	1	363	136
	(49)-(60)	1.50	2.0	5-60	1	400	116
	(61)-(72)	1.50	2.0	5-60	1	773	39
	(73)-(84)	1.50	2.0	5-60	1	1273	17

* I_∞ was varied from 5% to 60% with an increment of 5%

The accuracy of the present numerical model is first checked by verifying the level of error involved in the calculation of the volume and surface area of the droplet generated by the blocked-off technique. This is because the blocked-off technique cannot configure (reproduce) the exact spherical shape of the droplet, as can be seen in Figure 4.4. Thus, the accuracy of this technique is tested by comparing the instantaneous volume and surface area of the evaporating droplet predicted by this calculation technique (i.e.,, blocked-off treatment) versus their theoretical counterparts' computed by using the following expressions $V_d = \pi d^3 / 6$ and $A_d = \pi d^2$, respectively, where the droplet diameter (d = $2r$) is obtained from Equation (3.72). According to the chosen grid the blocked-off technique approximates the droplet as the sum of 4224 control volumes. These control volume have a total of 25344 surfaces/faces (each control volume has 6 faces) but only 1464 surfaces are subjected to flow and eventually represent the outer surface of droplet. Note that the number of control volumes and surfaces are kept constant throughout the course of the droplet evaporation whereas their dimensions change. More details about the present predictions of the droplet volume and surface area are provided in Appendix D. Predicted results are presented in Figure 5.10. This figure shows that the difference between the two methods is almost unnoticeable, less than 1%, indicating good accuracy of the blocked-off technique. The calculation error induced by the blocked-off technique can be minimized by making an adequately fine grid in the $2r$ calculation domain.

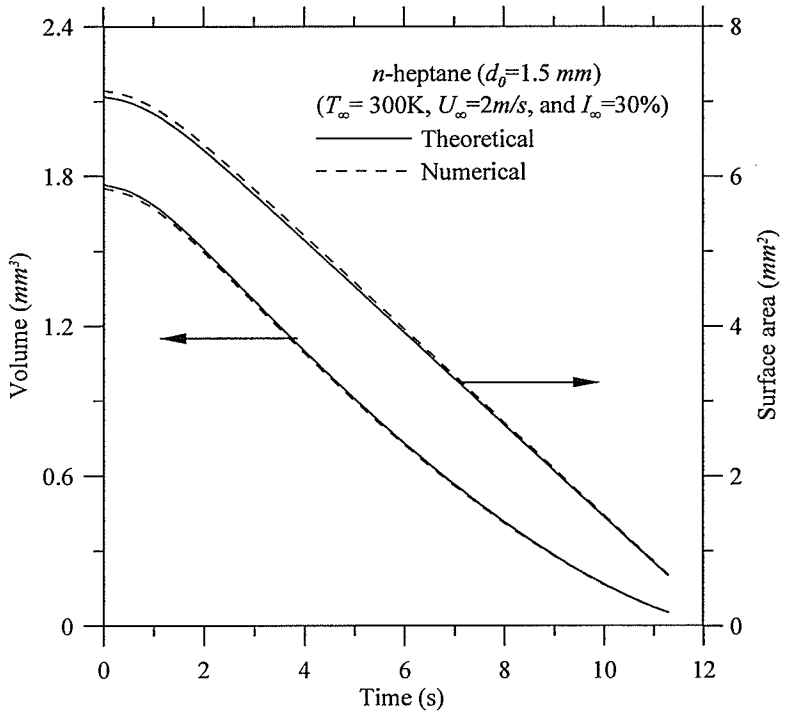

Figure 5.10 Time-history of *n*-heptane droplet's volume and evaporating surface area for typical test conditions

5.3.1 TURBULENCE EFFECT UNDER STANDARD FREESTREAM PRESSURE AND TEMPERATURE CONDITIONS

The current three-dimensional numerical model is validated first by comparing the present numerical predictions against the existing published experimental and numerical laminar data. The present laminar predictions are obtained by assigning a value of zero to the freestream turbulence intensity in the numerical code. Figure 5.11 displays a typical variation of the time-history of the squared normalized diameter of *n*-heptane droplet in freestream of air having a mean-velocity of U_∞= 6 m/s. This figure shows that the present predictions agree reasonably well with published numerical data (Zhang, 2003) and almost perfectly with experimental data (Gökalp *et al.*, 1988).

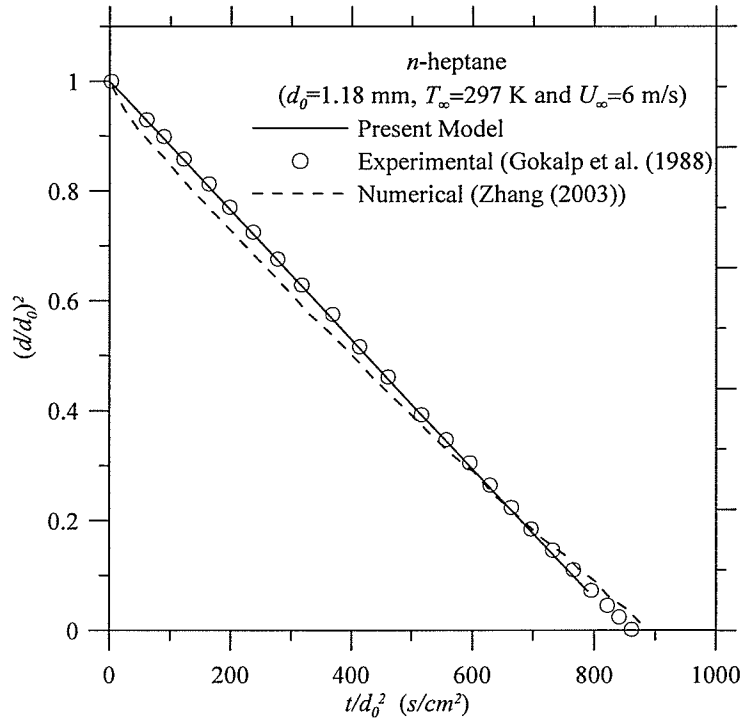

Figure 5.11 Time-history of the squared normalized diameter for *n*-heptane droplet in a laminar flow

Figure 5.12 displays the variation of the surface temperature of *n*-heptane and *n*-decane droplets versus the evaporation time for different turbulence intensities. As expected, this figure exhibits two distinct regions; transient and steady state. At any given airstream conditions, the transient region shows a rapid increase in the droplet surface temperature until it reaches a constant temperature, i.e., wet-bulb temperature. During the transient lifetime of the droplet, most of the heat transferred into the liquid phase is used to heat-up the liquid droplet. The steady-state region is characterized by a constant temperature, i.e., the wet-bulb temperature, which indicates that all the heat transferred to the liquid droplet is used only for evaporating the droplet. More importantly, this figure reveals that the droplet heat-up period decreases as the airstream turbulence intensity increases, indicating an increase in the rate of heat transfer to the droplet as a result of an increase in the airstream turbulence intensity. The only noticeable difference between the

two droplets is that the surface temperature of *n*-heptane is less than that of *n*-decane under similar test conditions. This is due to the difference in the amount of heat stored inside the droplet, which is directly proportional to the droplet boiling temperature that is higher for *n*-decane fuel.

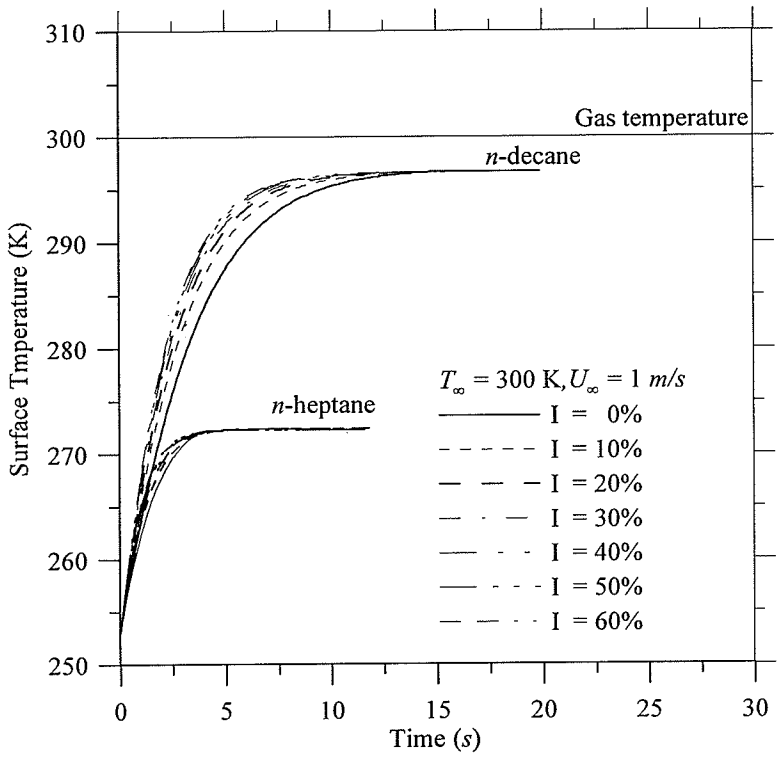

Figure 5.12 Time-history of *n*-heptane and *n*-decane droplets surface temperature for different airstream turbulence intensities

Figure 5.13 shows the time-history of the squared normalized diameter of *n*-decane droplet versus the normalized evaporation time for quiescent (stagnant) and laminar airstream, as well as for various airstream turbulence intensities. The droplet life time is terminated when 97.3% of the droplet is evaporated, however, only the initial portion of the laminar and quiescent (stagnant) data is presented in Figure 5.13 to enable observing the effect of turbulence. After the elapse of the droplet heating-up period, the squared droplet diameter appears to follow a linear variation with the evaporation time

obeying the famous d^2-law. Moreover, this figure clearly shows that turbulence decreases the life time of the droplet yielding an increase in the droplet mass transfer (i.e., the evaporation rate). The same scenario is seen with *n*-heptane droplet, which is shown in Figure 5.14.

The predicted vaporization rate of *n*-heptane and *n*-decane droplets under turbulent flow conditions which are deduced from Figures 5.13 and 5.14 shown above, are compared with published experimental data (Wu *et al.*, 2001). This comparison illustrated in Figure 5.15. This figure shows that the present numerical predictions obtained with the SST closure model agree reasonably well with their counterparts' experimental data within experimental error. However, the low-Reynolds k-ε model produced unsatisfactory results, as it overpredicts the vaporization rate of both droplets. This is may be attributed to the value of the calculated turbulent viscosity based on the low-Reynolds k-ε model which is slightly higher than that based on the SST model, which consequently yields a higher mass evaporation according to Equation (3.70). Note that in this equation, the mass evaporation increases as a result of an increase in the effective thermal conductivity, which is termed as $\lambda_{eff}=\mu / \mathrm{Pr}+ \mu_t / \sigma_h$ (Abou Al-Sood and Birouk, 2006a). Typical two-dimensional contours of turbulent viscosity predicted by using low-Reynolds k-ε and SST models are presented in Figures 5.16 and 5.17, respectively.

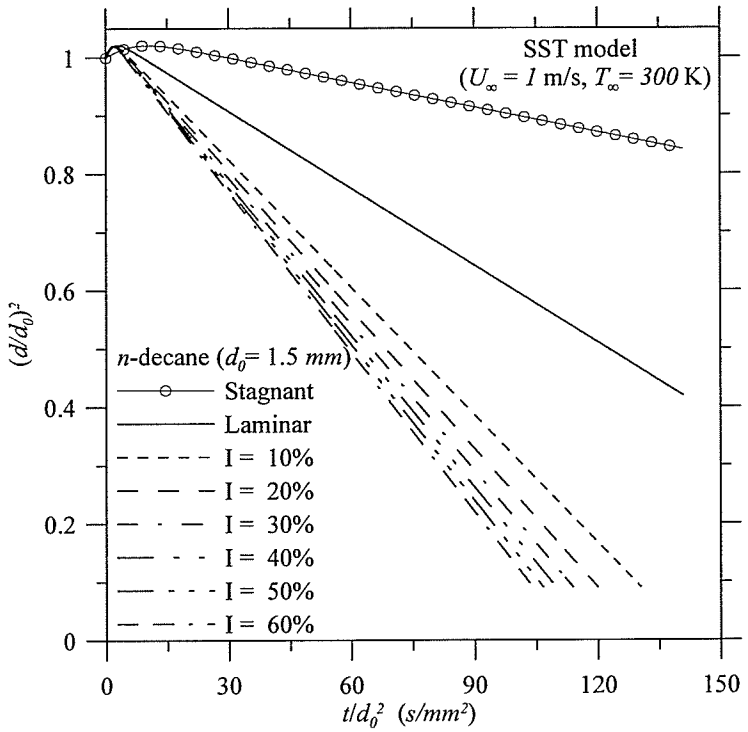

Figure 5.13 SST turbulence closure model based predictions of time-history of the squared normalized diameter of *n*-decane droplet

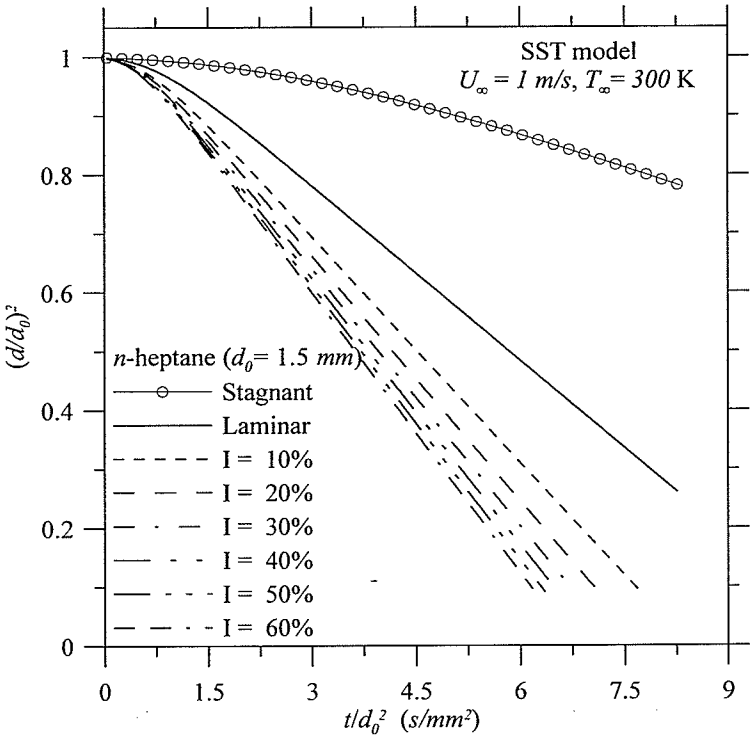

Figure 5.14 SST turbulence closure model based predictions of time-history of the squared normalized diameter of *n*-heptane droplet

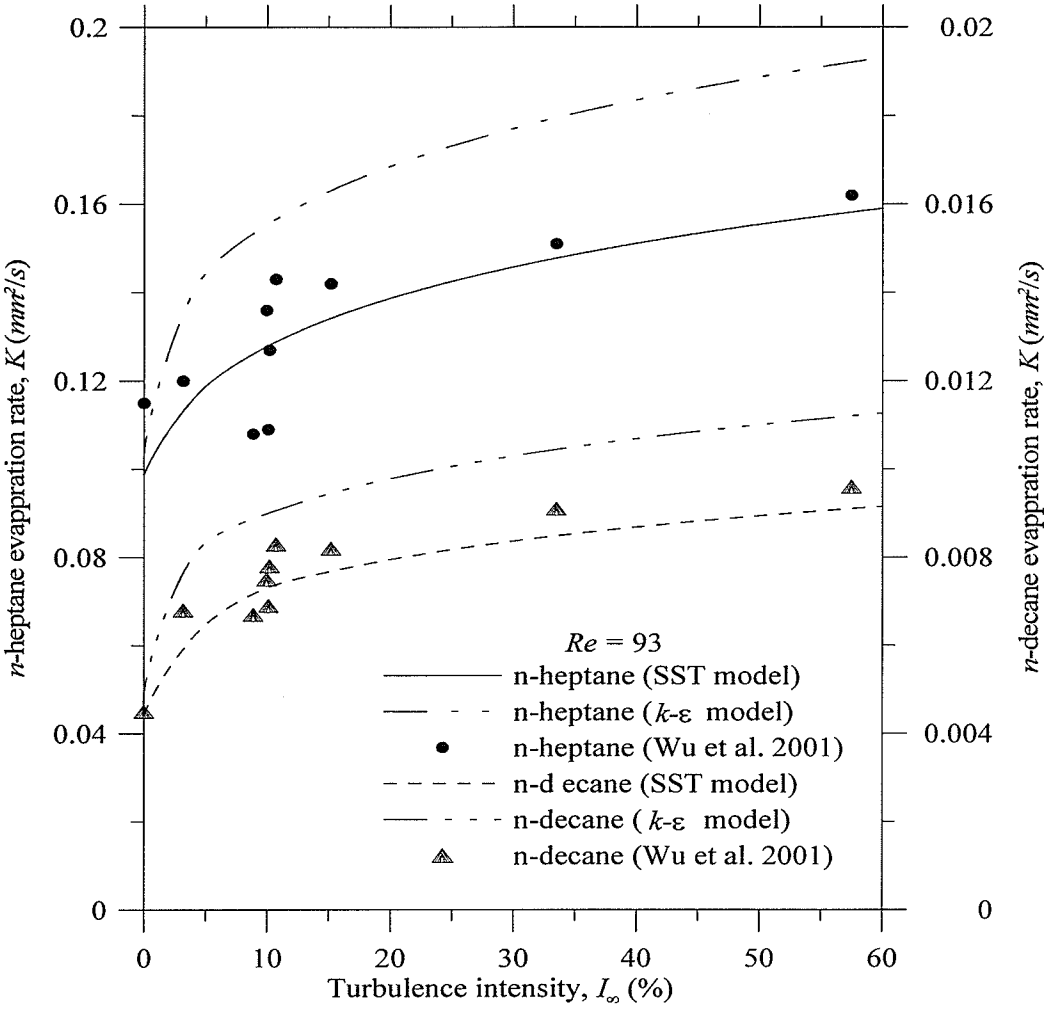

Figure 5.15 Variation of the evaporation rates of *n*-heptane and *n*-decane droplets versus freestream turbulence intensity

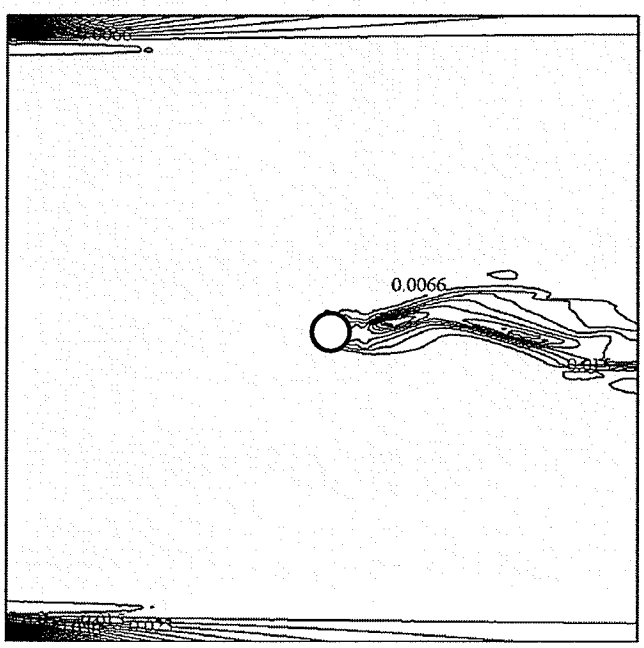

Figure 5.16 SST model-based calculation of turbulent viscosity contours over a sphere for freestream mean-velocity of 2 m/s and turbulence intensity of 60%

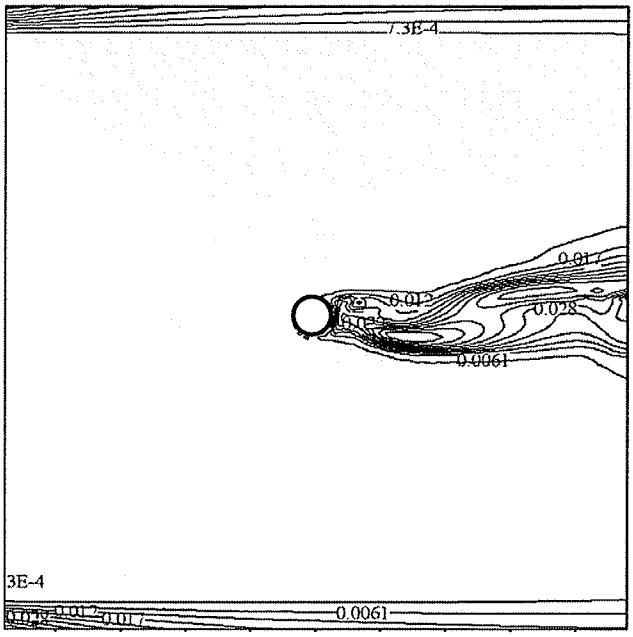

Figure 5.17 LRN k-ε model-based calculation of turbulent viscosity contours over a sphere for freestream mean-velocity of 2 m/s and turbulence intensity of 60%

The predictions discussed above based on the SST turbulence closure model are used to verify the vaporization Damköhler number correlation proposed by Gökalp *et al.* (1992) and Wu *et al.* (2001, 2003). Gökalp *et al.* (1992) defined the vaporization Damköhler number as a ratio between turbulence characteristic time, T_t, and evaporation characteristic time, T_v, as

$$Da_v = \frac{T_t}{T_v} \tag{5.4}$$

The turbulence and evaporation characteristic times are defined, respectively, as

$$T_t = \frac{d_0^{2/3}}{\varepsilon^{1/3}}, \tag{5.5}$$

$$T_v = \frac{\delta_M}{V_r}, \tag{5.6}$$

where ε, δ_M and V_r are turbulence dissipation rate, vapor film thickness around the droplet and, vapor blowing velocity, respectively. The turbulence dissipation rate is defined as (Hinze 1959)

$$\varepsilon = \mathrm{A}\frac{u'^3}{L_i}, \tag{5.7}$$

where A is a constant and assumed unity in this study and L_i is the integral length scale. The vapor film thickness and vapor blowing velocity are defined according to film theory (Abramzon and Sirignano, 1989) as follow

$$\delta_M = \frac{d}{Sh_0 - 2} F(B_M), \tag{5.8}$$

$$V_r = \frac{D_{AB} Sh^* (1 + B_M)}{d}, \tag{5.9}$$

where Sh_0 and Sh^* are the laminar and modified Sherwood numbers which are defined as

$$Sh_0 = 1 + (1 + \mathrm{Re}\,Sc)^{0.7}\,\mathrm{Re}^{0.077}, \tag{5.10}$$

$$Sh^* = 2 + \frac{(Sh_0 - 2)}{F(B_M)} \tag{5.11}$$

The diffusion correction factor $F(B_M)$ is defined as

$$F(B_M) = (1 + B_M)^{0.7}\,\frac{\ln(1 + B_M)}{B_M}, \tag{5.12}$$

where B_M is the Spalding mass transfer number, which is given as

$$B_M = \frac{Y_{F,s} - Y_{F,\infty}}{1 - Y_{F,s}}, \tag{5.13}$$

where Y_F is the fuel mass fraction given as

$$Y_{F,s} = \frac{p_{F,s}(T_s)M_F}{p_{F,s}(T_s)M_F + (p - p_{F,s}(T_s))M_a} \tag{5.14a}$$

$$\text{or } Y_{F,s} = \frac{X_{F,s}M_F}{X_{F,s}M_F + (1 - X_{F,s})M_a} \tag{5.14b}$$

Figure 5.18 shows the predicted normalized turbulent vaporization rates of *n*-decane and *n*-heptane droplets versus the vaporization Damköhler number, Da_v (see Eq. 5.4). The data of the vaporization Damköhler number are calculated by employing droplet-based Reynolds number in the range between 56 and 186, freestream turbulence intensity of up to 60% and a turbulent integral length scale assumed equal 5 times the initial droplet diameter, which is the average value measured by Wu *et al.* (2001 and 2003). As shown in Figure 5.18 the present numerical data for both fuels, i.e., *n*-heptane and *n*-decane, collapse on a single line having the following expression

$K/K_L = 0.786 Da_v^{-0.144}$. The correlation developed by Wu *et al.* (2003) is expressed as $K/K_L = 0.771 Da_v^{-0.111}$. The two expressions agree reasonably well, although they have slightly different values of the proportionality coefficient and the exponent of Da_v. This slight difference might be contributed to the experimental error as well as the assumption made for the turbulence integral length scale that is needed to calculate Da_v. Nevertheless, this comparison suggests that the vaporization Damköhler number can be used to correlate the effects of freestream turbulence on the droplet evaporation rate at ambient standard temperature and pressure conditions (Abou Al-Sood and Birouk, 2006c).

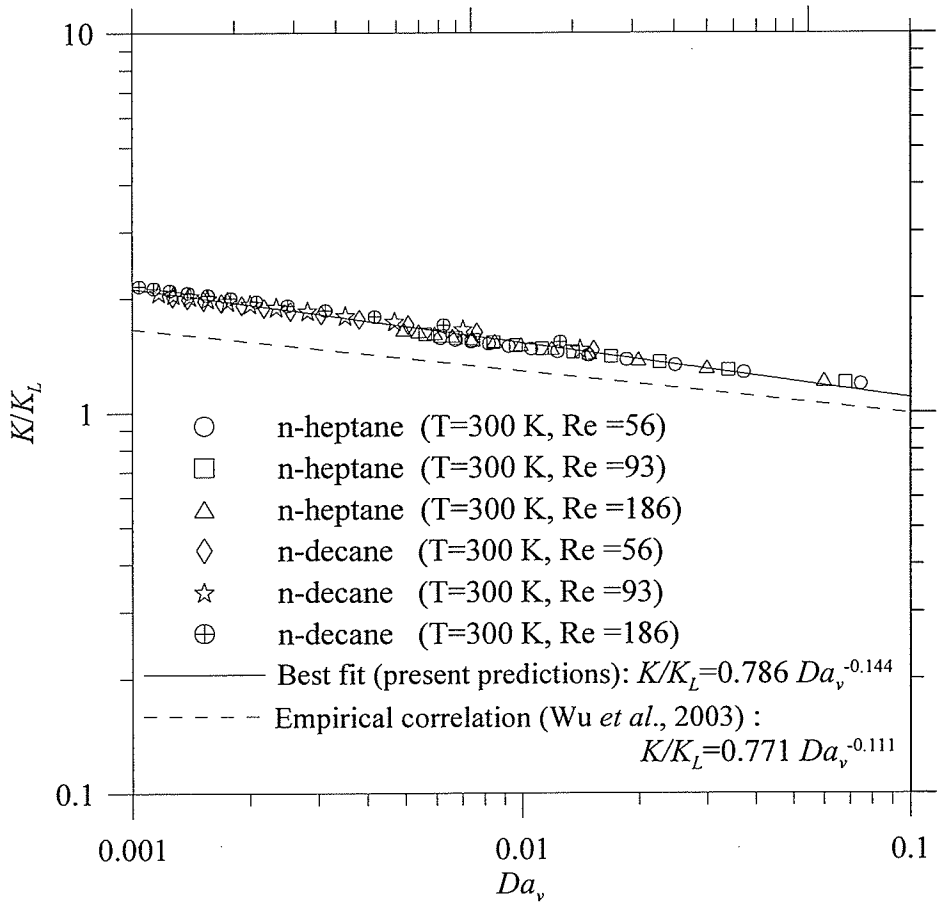

Figure 5.18 Normalized evaporation rate of *n*-heptane and *n*-decane droplets versus the vaporization Damköhler number

5.3.2 TURBULENCE EFFECT IN HOT AIRSTREAM CONDITIONS

Figure 5.19 shows the time-history of the squared normalized diameter of *n*-decane droplet as predicted by the present numerical model. The same figure displays also a comparison with the laminar numerical data of Megaridis (1993) and the laminar experimental data of Wong and Lin (1992) at a Reynolds number of 17 and a freestream temperature T_∞ =1000 K. Figure 5.19 exhibits two major distinct zones. The first one concerns the transient phase (i.e., the heating-up period) of the droplet. During this phase, contrary to the data of Megaridis (1993), the present predictions appear to agree reasonably well with its counterpart experimental data (Wong and Lin (1992)). The non-agreement of Megaridis (1993) data with the present predictions and the experimental data of Wong and Lin (1992) could be attributed to the assumption of constant droplet density which is employed by Megaridis (1993). The second zone concerns the droplet steady-state evaporation phase. Although Megaridis (1993) data seem to reveal shorter droplet life time, in fact the slope (i.e., the evaporation rate) of this steady-state linear variation of $(d/d_0)^2$ versus the normalized droplet evaporation time is approximately the same, within experimental error, for all three studies (i.e., 0.802 mm^2/s, 0.791 mm^2/s and 0.949 mm^2/s for the present predictions, Megaridis (1993) and Wong and Lin (1992), respectively).

Figure 5.20 shows the predicted time-history of the normalized squared diameter of *n*-heptane droplet for a freestream mean-velocity and a temperature of 2 m/s and 1273K, respectively, over a wide range of freestream turbulence intensity. Two important remarks can be drawn from this figure. Firstly, the droplet heating period becomes shorter as the freestream turbulence intensity increases. Secondly, the overall droplet

lifetime decreases with increasing turbulence intensity. Furthermore, it is remarkably noticeable that freestream turbulence intensity still has an effect on the droplet's evaporation rate even at elevated freestream temperatures. In addition, Figure 5.20 reveals that the d^2-law still holds even at high freestream temperatures. This observation contradicts that of Sazhin *et al.* (2005) who claimed that the d^2-law does not hold at higher ambient temperatures (i.e., for $T_\infty > 700K$) when considering radiation effect. However, the present predictions with neglected radiation are in agreement with those of Morin *et al.* (2005) who showed experimentally that the d^2-law holds at similar ambient gas temperatures. Figure 5.21 shows the time history of the surface temperatures of *n*-heptane and *n*-decane droplets at different turbulence intensities. The surface temperature for both fuels increases asymptotically until they reach their wet-bulb temperatures, which are below their corresponding boiling temperatures. Also, the effect of turbulence is noticeable in decreasing the droplet heat-up period because of the increase in the heat transfer from the surroundings to droplet due to turbulence.

Figure 5.22 presents the variations of the *n*-heptane and *n*-decane droplets' turbulent evaporation rates normalized by their corresponding laminar values, K/K_L, for three typical freestream temperatures, i.e., 300K, 773K and 1273K. This figure reveals that increasing the ambient temperature from 300K to 773K and then to 1273K increases K/K_L by a maximum factor of approximately 1.66, 1.51, 1.41 for *n*-heptane and 2.15, 1.87, 1.79 for *n*-decane, respectively, when varying the freestream turbulence intensity from 0% to 60% (the turbulent evaporation rates of *n*-heptane and *n*-decane droplets are tabulated in Appendix E). This suggests that the effect of turbulence on droplet lifetime tends to weaken as the freestream temperature increases. In addition, it can be observed

from this figure that overall the effect of turbulence is much more pronounced at low to moderate turbulence intensities (i.e., for $I_\infty < 20$). This in line with the interpretation provided in Birouk *et al.* (1996), that is, turbulence role is to diffuse the vapour away from the droplet surface. Therefore an increase in the droplet's surrounding temperature increases the heat transfer into the droplet which in turn increases the molecular diffusion of the vapour. As a result the vapour residence time at the droplet surface decreases which makes less available time for turbulence to act

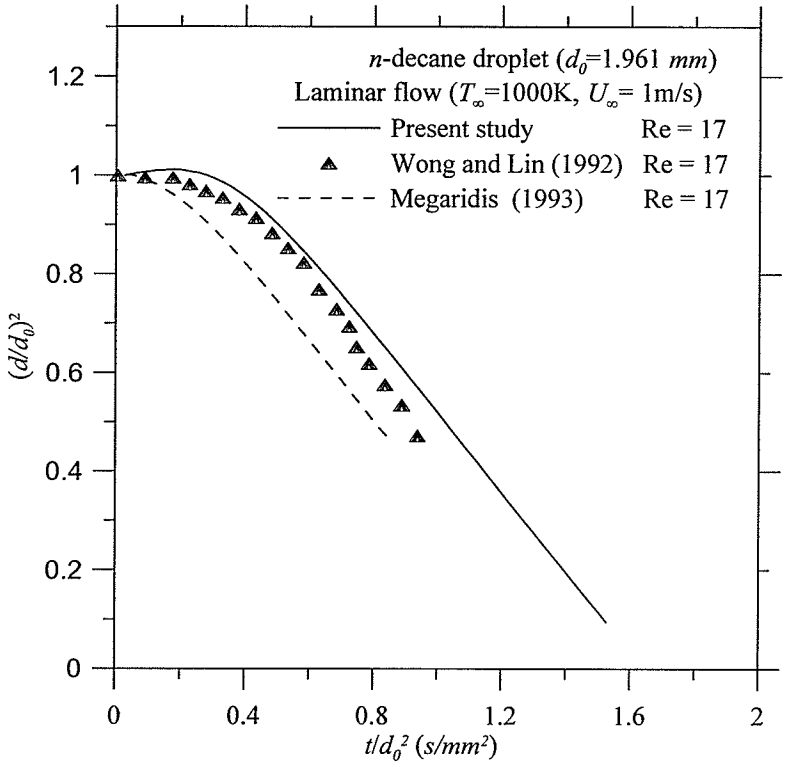

Figure 5.19 Time-history of *n*-decane normalized squared diameter

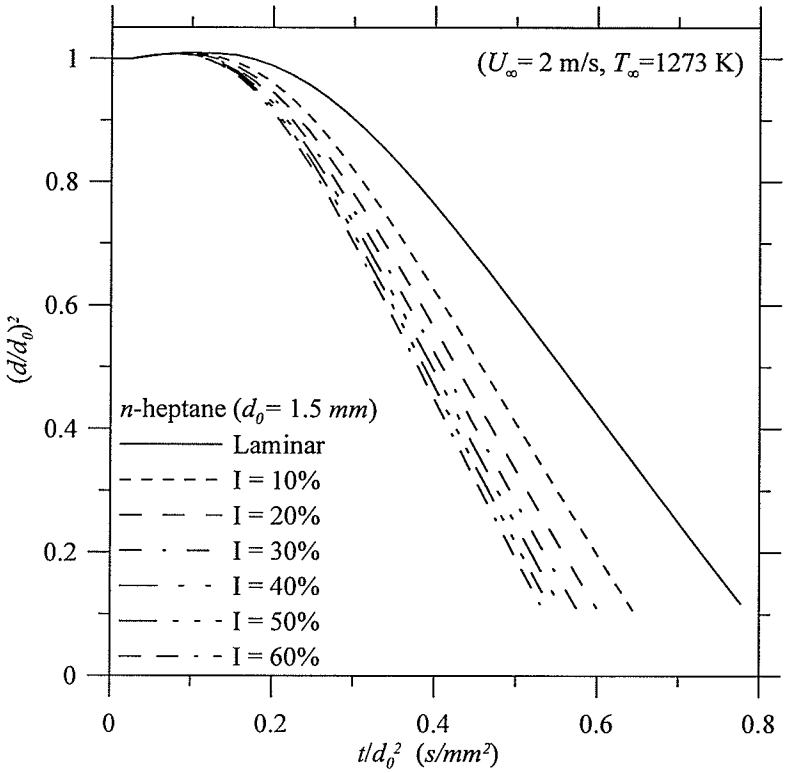

Figure 5.20 Time-history of the normalized squared diameter of *n*-heptane droplet at T_∞ = 1273 K and U_∞= 2 m/s for various freestream turbulence intensities

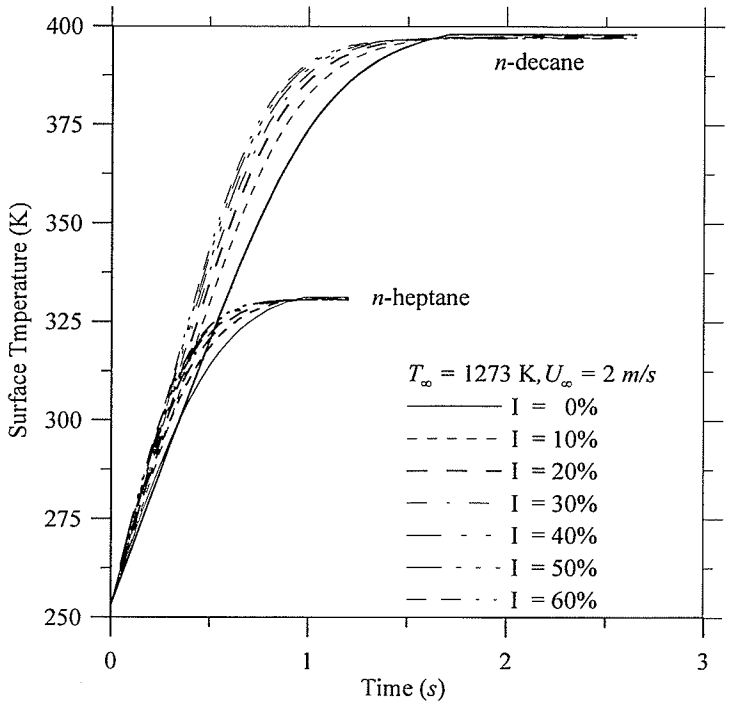

Figure 5.21 Time-history of the surface temperature for *n*-heptane and *n*-decane droplets at different turbulence intensities

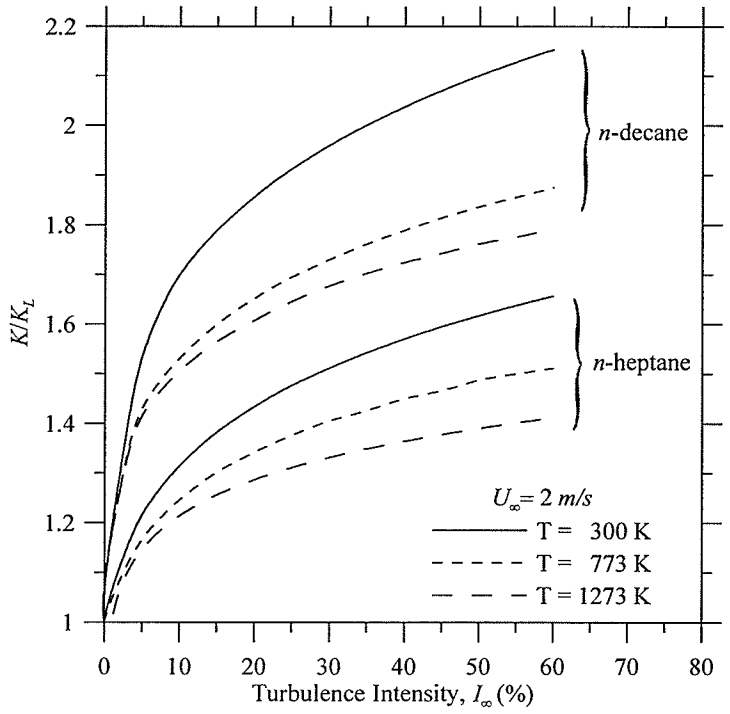

Figure 5.22 Normalized evaporation rate of *n*-heptane and *n*-decane droplets versus the freestream turbulence intensity at a typical freestream mean velocity $U_\infty = 2$ *m/s* and various freestream temperatures

The vaporization Damköhler number correlation, which is discussed in the previous section, is examined for freestream temperatures higher than room temperature. The tested temperatures are 363 K, 400 K, 773 K and 1273 K. It is discovered that the corresponding Damköhler number could not be used to correlate the variation of K/K_L. This is mainly due to the fact that the Da_v for *n*-decane droplet, which is smaller than that of *n*-heptane droplet at room temperature conditions, becomes larger at higher freestream temperatures (see Figure 5.23). To find out the reason for the change of Da_v with T_∞, the variation of the characteristic vaporization time, t_v, is plotted versus the freestream temperature, T_∞, for typical flow conditions, as shown in Figure 5.24. This figure reveals that the scenario seen in Figure 5.23 is repeated in Figure 5.23 but with different trend's sign, which indicates that the variation of the Da_v seen in Figure 5.23 is caused by the

variation of t_v. Therefore, we decided to investigate the variation of the fuel mole fraction as well as the fuel mass fraction (i.e., the product of the fuel mole fraction and the molecular weight $X_{Fs}M_F$) which is the parameter needed for calculating t_v (see Eq. 5.14b). Figure 5.25 clearly shows that the trend of t_v seen in Figure 5.24 is driven by the variation of $X_{Fs}M_F$. Therefore, the Da_v number correlation proposed by Gökalp *et al.* (1992) and Wu *et al.* (2001, 2003) does not seem to hold for a droplet evaporating in hot convective flows.

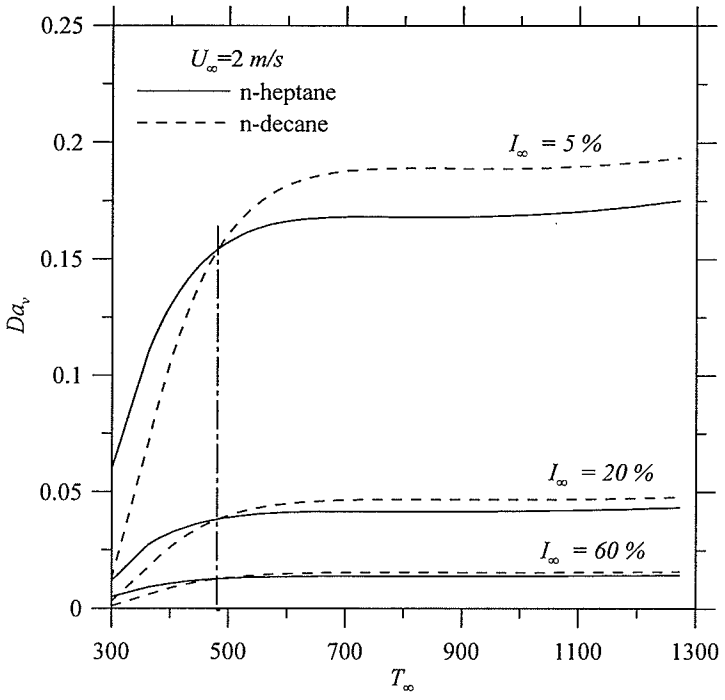

Figure 5.23 Vaporization Damköhler number versus the freestream temperature for typical turbulence intensities

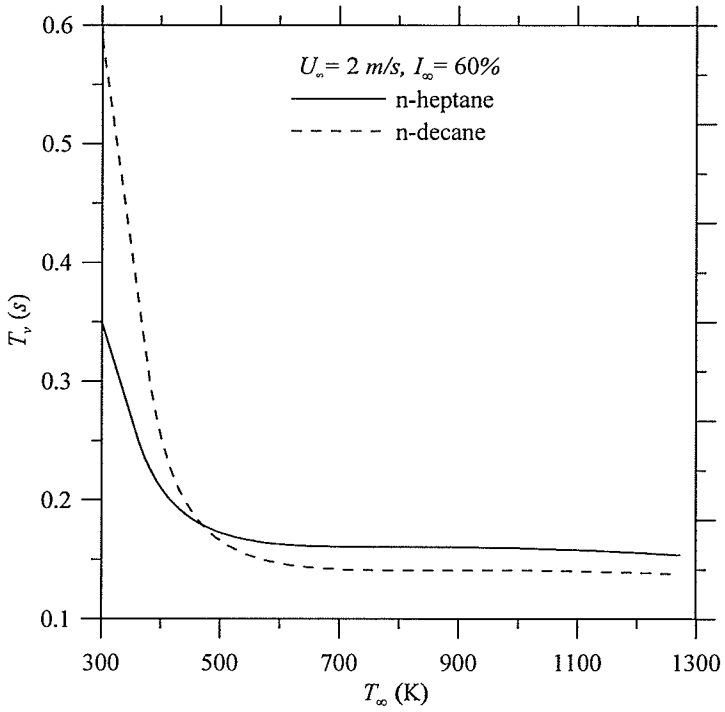

Figure 5.24 Droplet evaporation characteristic time versus the freestream temperature for typical turbulence intensity

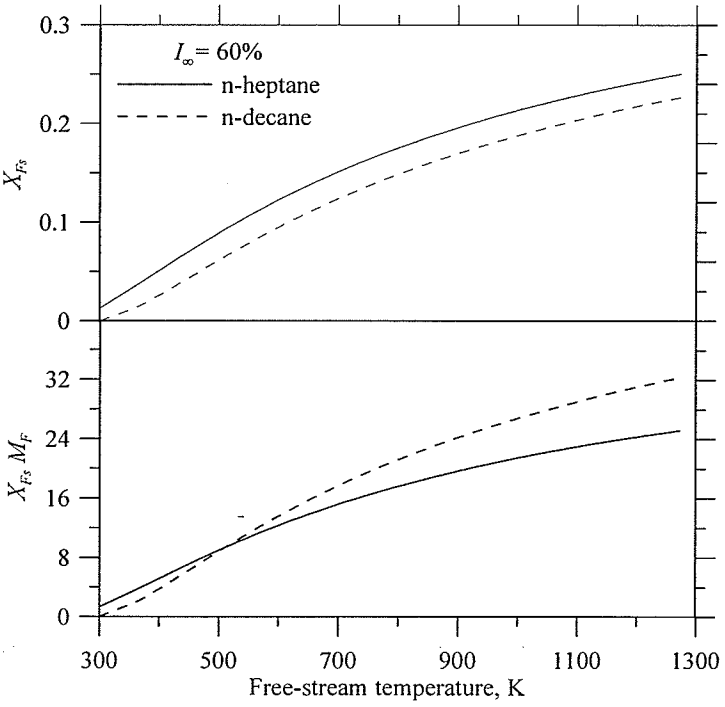

Figure 5.25 Fuel mole and mass fractions versus the freestream temperature for various turbulence intensities

In an attempt to correlate the droplet turbulent mass transfer rate over a wide range of freestream temperatures, the conventional form, i.e., Eq. (2.2) presented in Chapter 2, is employed. Sherwood number appears in this equation is calculated by using the droplet mass transfer rate $\dot{m}_{evap}$, surface temperature T_s and, instantaneous droplet diameter of the steady-state region as

$$Sh = \dot{m}_{evap} / (\pi d \rho_m D_{AB} B_M), \tag{5.15}$$

where D_{AB} is the mass diffusion coefficient, B_M is the Spalding mass transfer number that is defined as $B_M = (Y_{F,s} - Y_{F,\infty})/(1 - Y_{F,s})$. All mixture's properties are calculated at reference conditions of temperature and fuel mass fraction as

$$T_f = T_s + (T_\infty - T_s)/3, \tag{5.16}$$

$$(Y_{F,s})_f = Y_{F,s} + (Y_{F,\infty} - Y_{F,s})/3. \tag{5.17}$$

Schmidt and Reynolds numbers of the gas mixture are calculated as $Sc_f = \mu_f / (\rho_f D_{AB})$ and $\mathrm{Re}_m = \rho_\infty d U_\infty / \mu_f$, respectively.

The present predictions of the laminar Sherwood number, that is for I_∞= 0%, compares well with the data of Renksizbulut *et al.* (1991) for similar test conditions, as can be seen in Figure 5.26. Figure 5.27 shows the variation of *n*-heptane and *n*-decane steady-state Sherwood number versus the freestream Reynolds number for different freestream turbulence intensities and temperatures, which range between 0% and 60% and, from 300K to 1273K, respectively. Three mean velocities, i.e., 0.6 m/s, 1 m/s and 2 m/s are employed. This figure shows that Sherwood number increases with increasing the freestream turbulence intensity for a given Reynolds number. The variation of the turbulent Sherwood number versus the freestream turbulence intensity can be correlated

by using Eq. (2.2) presented in Chapter 2. The best fit for the present predicted data is found to have the following expression (with a standard deviation of 93%)

$$Sh_f(1+B_{M,f})^{0.7} = 2+0.914\,\mathrm{Re}_M^{1/2}\,Sc_f^{1/3}\left(1+1.235I_\infty^{0.372}\right). \tag{5.18}$$

This correlation, which is displayed in Figure 5.28, is tested over a wide range of liquid properties and freestream conditions. The liquid properties are varied by using two different fuels, i.e., *n*-heptane and *n*-decane droplets. The freestream conditions are varied by changing the temperature in the range between 300K and 1273K, turbulence intensity between 5% and 60% and the freestream mean-velocity in the range between 0.6 m/s and 2 m/s. The proposed correlation (e.g. Eq. (5.18)) is compared with previously published data (see Figure 2.2 of Chapter 2). This Figure shows that although all the correlations reported in Table 2.1 and presented in Fig. 2.2 showed a linear increase in the sphere or droplet mass transfer with C_T, the present study predicts the highest values of Sherwood number. The present correlation is also compared with recent experimental data of Yearling (1995) as shown in Figure 5.28. This figure indicates that there is no agreement between the present predictions and Yearling's data. An examination of Yearling's (1995) data revealed that there is no significant difference between Yearling's turbulent and laminar data as illustrated in Figure 5.29. Yearling tested low levels of turbulence intensity, i.e., below 11%, and this is maybe the reason why Yearling's experimental turbulent mass transfer data are comparable to their counterparts' laminar data. In other words, Yearling's turbulent data may be within the experimental error (Abou Al-Sood and Birouk, 2006c).

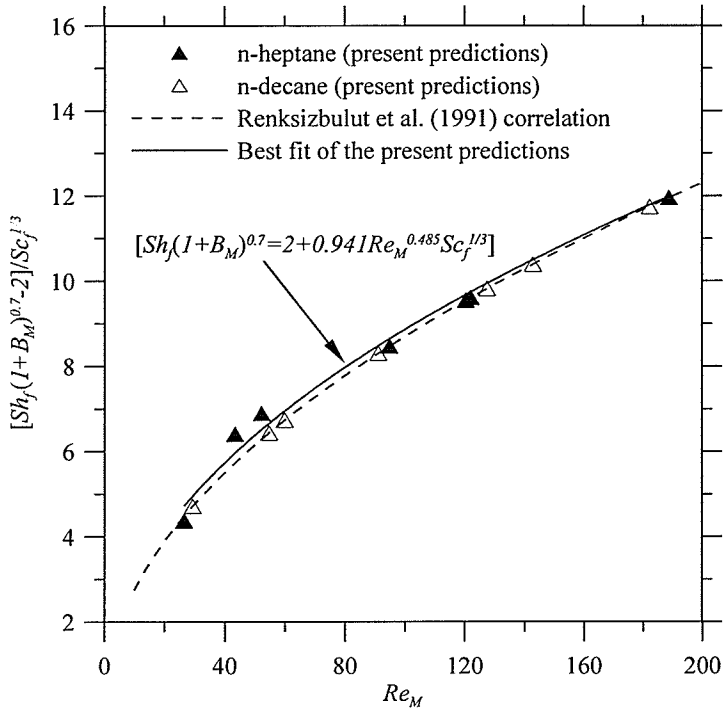

Figure 5.26 Predicted laminar Sherwood number for *n*-heptane and *n*-decane droplets versus Reynolds number for freestream temperature ranging between 300 K and 1273 K

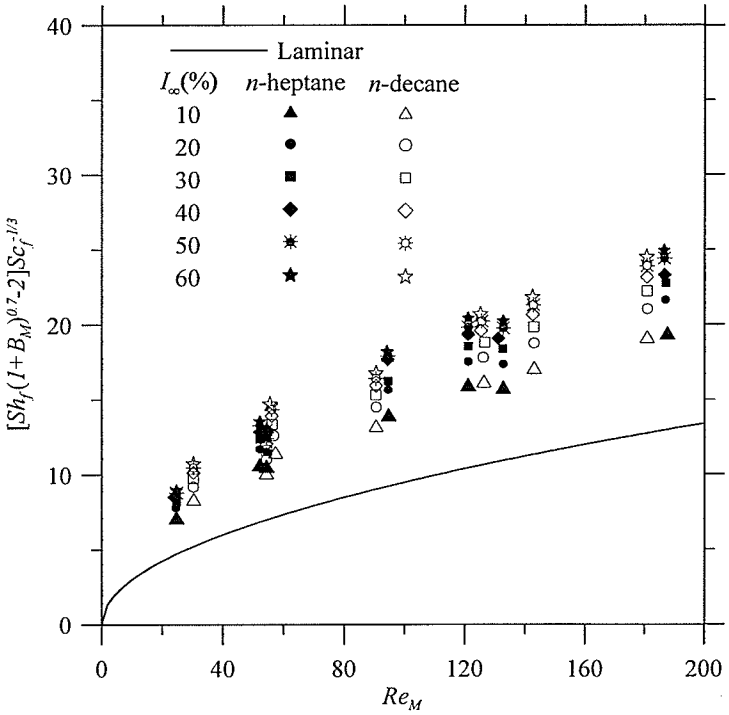

Figure 5.27 Predicted Sherwood number for *n*-heptane and *n*-decane droplets versus Re_M for different turbulence intensities

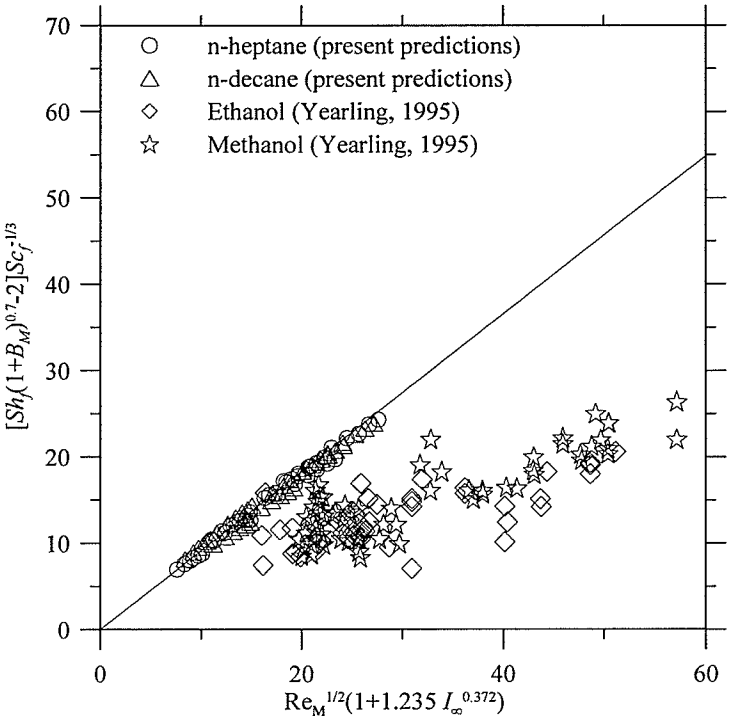

Figure 5.28 Comparison of the predicted turbulent Sherwood number for *n*-heptane and *n*-decane droplets with the experimental data of Yearling (1995)

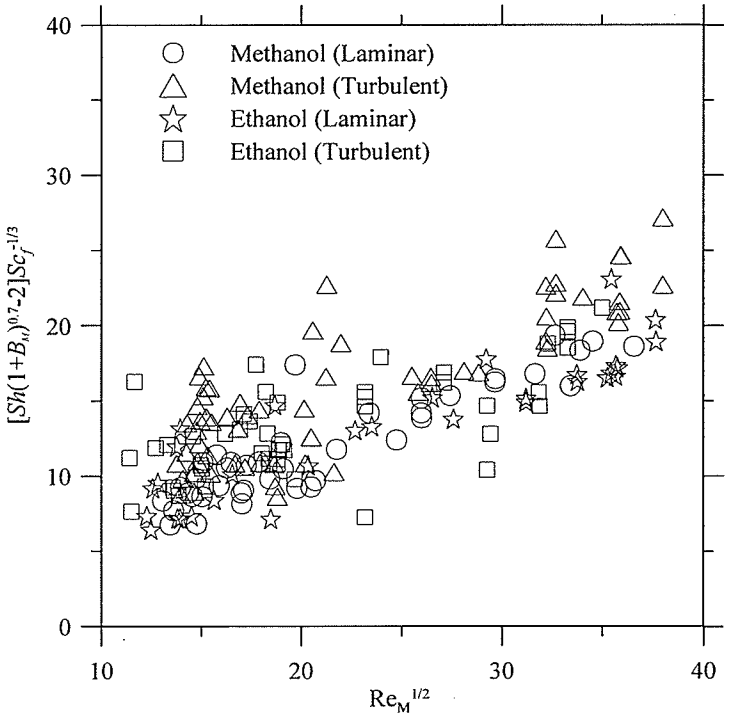

Figure 5.29 Yearling (1995) Laminar and turbulent Sherwood number data versus Reynolds number

Chapter

6

CONCULSIONS AND FUTURE WORK

6.1 CONCLUSIONS

A three-dimensional numerical model is developed for investigating the effect of freestream turbulence on (i) the drag coefficient of a non-evaporating droplet (sphere) and, (ii) the mass transfer (evaporation rate) of a droplet. The freestream Reynolds number, turbulence intensity and temperature are varied to provide a wide range of test conditions whereas the pressure is kept constant. For the study of the droplet evaporation, the liquid properties are varied by investigating *n*-heptane and *n*-decane droplets

The major conclusions are summarized as follow

- Although the Cartesian grid based blocked-off technique is unable to reproduce the exact shape of the sphere (or droplet), the induced calculation error can be reduced substantially by increasing the number of grids in the sphere (or droplet) calculation domain.

- Four different turbulence closure models are tested for predicting the effect of the freestream turbulence intensity on the sphere drag coefficient. However only the Menter's SST turbulence closure model predicts realistic drag coefficient results which agree with published data.
- The numerical code based on the SST turbulence closure model predicts reasonably well the vaporization rate of hydrocarbons fuel droplets as compared to published data.
- Although the freestream turbulence intensity seems to affect the droplet mass transfer even at temperatures higher than the liquid boiling temperature, the effect of turbulence weakens as the freestream temperature increases. This may be attributed to the fact that as the temperature increases the vapor molecular diffusion increases as well, which reduces the residence time of the vapor around the droplet and thus decrease the necessary time for turbulence to act. This is may be the reason why the effect of freestream turbulence is more pronounced at lower values, i.e., $I_\infty < 20\%$.
- The expression proposed in the literature which correlates the effect of turbulence on the droplet vaporization rate (K/K_L) in terms of a vaporization Damköhler number (Da_v) is found to be valid only at ambient room temperature conditions.
- A droplet mass transfer correlation based on Sherwood number is proposed to account for the effect of freestream turbulence on droplet mass transfer in a hot airflow.

- More experimental data are needed to confirm the limitations of the evaporation Damköhler number correlation as well as to verify the mass transfer correlation proposed in the present study.

6.2 FUTURE WORK

The numerical model developed in this thesis can be extended to study the following:

- The effect of turbulence on the droplet evaporation under ambient elevated pressure and temperature conditions. This also implies that the effects of solubility as well as non-ideality of the gas phase should be considered.
- The effect of radiation particularly when the droplet's surrounding is at reasonably high temperatures.
- The accuracy of the blocked-off technique. This will be performed by comparing the sphere drag coefficient predicted by using the blocked-off technique with that obtained by using another technique that uses spherical coordinates.
- The evaporation process of multi-components droplets.
- The combustion process of mono- as well as multi-components droplets.

REFERENCES

Abou Al-Sood, M. M., Birouk, M., 2005a, "Computational study of turbulent flow around a sphere using finite volume blocked-off technique", *20th Canadian Congress of Applied Mechanics, CANCAM 2005, McGill University May 30th - June 2nd*

Abou Al-Sood, M. M., Birouk, M., 2005b, "Numerical study of laminar flow around a sphere using finite volume blocked-off technique", *20th Canadian Congress of Applied Mechanics, CANCAM 2005, McGill University May 30th - June 2nd*

Abou Al-Sood, M. M., Birouk, M., 2005c, "A Three-dimensional numerical model for calculating the rate of mass transfer from liquid droplets in turbulent flow", *4th International Conference on Heat Transfer, Fluid Mechanics and Thermodynamics, HEFAT2005, Cairo, Egypt, Sept.* 18- 22..

Abou Al-Sood, M. M., Birouk, M., 2006a, "A Numerical model for calculating the vaporization rate of a fuel droplet exposed to a convective turbulent airflow", *Int. J. Num. Meth. Heat Fluid Flow* (accepted)

Abou Al-Sood, M. M., Birouk, M., 2006b, 'Numerical simulation of a droplet evaporating in hot convective turbulent environments, Combustion Institute/Canadian Section, Spring Technical Meeting, Kingston, Ontario, Canada, May 14-16

Abou Al-Sood, M. M., Birouk, M., 2006c, "A numerical study of the effect of turbulence on mass transfer from a fuel droplet evaporating in hot freestream", *Int. J. of Thermal Science* (accepted)

Abramzon, B. and Sirignano, W. A., 1989, "Droplet vaporization model for spray combustion calculations", *Int. J. Heat Mass Transfer*, Vol. 3, pp.1605-1618

Anderson T. J., and Uhlherr, P. H. T., 1977, "The influence of stream turbulence on the drag coefficient spheres," *Preprints of papers to the sixth Australian*

Hydraulics and Fluid Mechanics Conference, Australia, Institute of Engineers, pp. 541-545

Bagchi, P., and Balachandar, S., 2003, "Effect of turbulence on the drag and lift of a particle", Physics of Fluids, Vol. 15, pp. 3496-3513.

Birouk, M., 1996, "Influence de la turbulence homogene et isotrope sur la vaporization et la combustion de gouttes de combustibles liquids," Ph.D. thesis, *Universite D'Orleans,* France

Birouk, M., and Abou Al-Sood, M. M., 2006, "Numerical study of sphere drag coefficient in turbulent flow at low Reynolds number, *Numerical Heat Transfer A* (accepted)

Birouk, M., and Gökalp, I., 2002, "A new correlation for turbulent mass transfer from liquid droplets", *Int. J. Heat Mass Transfer*, Vol. 45. pp. 37-45

Birouk, M., and Gökalp, I., 2006, "Current status of droplet evaporation in turbulent flows", *Progress in Energy and combustion*, Vol. 32(4), pp. 408-423

Birouk, M., Chauveau, C., Sarah, B., Quilgars, A. and Gökalp, I., 1996, "Turbulence effects on the vaporization of monocomponent single droplets", *Combustion Science and Technology*, Vols. 113-114, pp. 413-428

Borjini, M. N., Farahat., H., and Radhouani, M. S., 2003, "Analysis of radiative Heat transfer in a partitioned idealized furnace," *Numerical Heat Transfer A*, Vol. 44, no. 2, pp. 199-218

Brown, R. A. S., Sato, K., and Sage, B. H., 1958, "Material transfer in turbulent gas stream: Effect of turbulence on macroscopic transport from spheres", *Chem. Eng. Data Series*, Vol. 3, pp. 263-272

Brucato, A., Grisafi, F. and Montante, G., 1998, "Particle drag coefficients in turbulent fluids", *Chemical Engineering Science*, Vol. 53, pp. 3952-3314

Brucato, A., Grisafi, F. and Montante, G., 1998, "Particle drag coefficients in turbulent fluids", *Chemical Engineering Science*, Vol. 53, pp. 3952-3314

Brucato, A., Grisafi, F. and Montante, G., 1998, "Particle drag coefficients in turbulent fluids", *Chemical Engineering Science*, Vol. 53, pp. 3952-3314

Byun, D. Y., Baek, S. W., and Kim, M. Y., 2003, "Investigation of radiative heat transfer in complex geometries using blocked-off , multiblock, and embedded

boundary treatments", *Numerical Heat Transfer A*, Vol. 43, no. 8, pp. 807-825

Chai, J. C., Lee, H. S. and Patankar, S. V., 1993, "Treatment of Irregular Geometries Using a Cartesian-Coordinates-Based Discrete-Ordinates-Method, Radiative Heat Transfer: Theory and Applications", HTD- Vol. 244, *ASME*, New York

Chien, K.-Y., 1982, "Predictions of channel and boundary-layer flows with a low-Reynolds number turbulence model", AIAA Journal Vol. 20, pp. 33-38

Clamen, A. and Gauvin, W. H., 1969, "Effect of turbulence on the drag coefficients of spheres in a supercritical flow regime", AIChE, J., Vol. 15, pp. 184-189

Clift, J. R., and Gauvin, W. H., 1971, "Motion of entrained particles in gas streams", *Can. J. Chem. Eng.*, Vol. 49, pp. 439-448

Clift, J. R., and Gauvin, W. H., 1971, "Motion of entrained particles in gas streams", *Can. J. Chem. Eng.*, Vol. 49, pp. 439-448

Clift, J. R., Grace, J. R., and Weber, M. E., 1978, *Bubbles Drops and Particles*, New York: Academic Press.

Coelho, P. J., Goncalves, J. M., Carvalho, M. G. and Trinic, D. N., 1998, "Modelling radiative heat transfer in enclosures with obstacles," *Int. J. Heat Mass Transfer*, Vol. 41, pp. 745-756

Consalvi, J. L., Porterie, B., and Lraud, J. C., 2003, "Method for computing the interaction of fire environment and internal solid boundaries," *Numerical Heat Transfer A*, Vol. 43, no. 8, pp. 777-805

Constantinescu, S.G., and Squires, K.D, 2004, "Numerical investigation of the flow over a sphere in the subcritical and supercritical regimes", *Physics of Fluids*, Vol. 15, no. 5, pp. 1449-1467.

De Kocl, D. J., 2005, "Optimal tundish design methodology in a continuous casting process", Ph.D. thesis, *University of Pretoria*, South Africa

Drikakis, D., 1995, "Development and implementation of parallel high-resolution schemes in 3D flows over bluff bodies", *Proceedings of the Parallel*

CFD Conference Implementation and Results Using Parallel Computers, Elsevier Science Publishers, Amsterdam, pp 191–198

Fan, S., Lakshminarayana, B. and Barnett, M., 1982, "A low-Reynolds number k-ε for unsteady turbulent boundary layer flows", AIAA Journal Vol. 20, pp. 33-38

Galloway, T. R., and Sage, B. H., 1964, "Thermal and material transfer in turbulent gas streams- A method of prediction for spheres", *Int. J. Heat Mass Transfer*, Vol. 7, pp. 283-291

Galloway, T. R., and Sage, B. H., 1967, "Thermal and material port from spheres: Prediction of macroscopic thermal and material transport", *Int. J. Heat Mass Transfer*, Vol. 10, pp. 1195-1210

Gökalp, I., Chauveau, C., and Richard, J. R., 1988, "Observation on the low temperature vaporization and envelope or wake flame burning of *n*-heptane droplet at reduced gravity during parabolic flights," *Proc. Combust. Instit.*, Vol. 22, pp. 2027-2035

Gökalp, I., Chauveau, C., Simon, O. and Chesneau, X., 1992, "Mass transfer from liquid fuel droplets in turbulent flow", *Combust. Flame*, Vol. 89, pp. 286-298

Gore, R. A., and Growe, C. T., 1990, "Discussion of Particle drag in a dilute turbulent two-phase suspension flow", *Int. J. Multiphase flow*, Vol. 16, pp. 359-361

Gostkowski, V. J., and Costello, F. A., 1970, "The effect of free stream turbulence on heat and mass transfer from stagnation point of a sphere", *Int. J. Heat Mass Transfer*, Vol. 13, pp. 1382-1386

Harlow, F.H., Nakayama, P.I., 1967, "Turbulence transport equations", Phys. Fluids, Vol. 10, pp.2323-2423

Hayward, G. L., and Pei, D. C., 1978, "Local heat transfer from a single spheres to a turbulent air stream", *Int. J. Heat Mass Transfer*, Vol. 21, pp. 35-41

Hinze, J. O., 1959, *Turbulence*, 1st edition, McGraw Hill

Hiromitsu, N. and Kawaguchi, O., 1995, "Influence of flow turbulence on the evaporation rate of suspended droplet in a hot air flow," *Heat Transfer-Japanese Research*, Vol. 24, pp. 689-700.

Hsu, N. T., and Sage, B. H., 1957, "Thermal and material transfer in turbulent gas stream: Local transport from spheres', *A. I. Ch. E. Journal*, Vol. 3, no. 3, pp. 405-410

Johnson, T. A., 1996, "Numerical and experimental investigation of flow past a sphere up to a Reynolds number of 300", Ph.D. dissertation, *University of Iowa*, USA

Jones, W. P., and Launder, B. E., 1973, "The calculation of low-Reynolds-number phenomena with a two-equation model of turbulence", *Int. J. Heat and Mass Transfer*, Vol. 16, pp. 1119-1130

Kantha, L. H., 2004, "Length scale equations in turbulence models", *Nonlinear Processes in Geophysics*, Vol. 11, pp. 83-97

Kim, J., Kim, D. and Choi, H., 2001, "An immersed boundary finite-volume method for simulation of flow in complex geometries", *J. Comput. Phy.*, Vol. 171, pp. 35-60

Kim, M. Y., Wook, S. W. and Park, J. H., 2001, "Unstructured Finite-Volume Method for Radiative Heat Transfer in a Complex Two-Dimensional Geometry with Obstacles", *Numerical Heat Transfer B*, Vol. 39, pp. 617-635

Kolmogorov, A. N., 1942, "Equations of turbulent motion of an incompressible fluid", *Izv. Akad. Nauk SSSR Ser. Fiz.,* Vol. 6, pp. 56–58.

Kolmogorov, A. N., 1942, Equations of turbulent motion of an incompressible fluid", *Izv. Akad. Nauk SSSR Ser. Fiz.,* Vol. 6, pp. 56–58

Kral, L. D., 1998, "Recent experience with different turbulence models applied to the calculation of flow over aircraft components," *Prog. Aerospace Sci.*, Vol. 34. pp. 481-541.

Lam, C. K. G., Bremhorst, K. A., 1981, "Modified form of the k-ε model for predicting wall turbulence", Journal of Fluid Engineering, Vol. 103, pp. 456-460

Launder, B. E., Sharma, B. I., 1974, "Application of the energy dissipation model of turbulence to the calculation of the flow near a spinning disc", Letters in Heat and Mass Transfer, Vol. 1, pp 131-138

Lavender, W. J., and Pei, D. C., 1967, "The effect of fluid turbulence on the rate of heat transfer from spheres", *Int. J. Heat Mass Transfer*, Vol. 10, pp. 529-539

Lee, S. L., 1987, "Particle drag in a dilute turbulent two-phase suspension flow," *Multiphase Flow*, vol. 13, pp. 247-256.

Lefebvre, A.H., 1989, *Atomization and sprays*, Hemisphere Publishing Corp

Leister, H.-J., and Perić, M., 1994, "Vectorized strongly implicit solving procedure for a seven-diagonal coefficient matrix", *Int. J. Num. Meth. Heat Fluid Flow*, Vol. 4, pp. 159-172

Maisel, D. S., and Sherwood, T. K., 1950, "Effect of air turbulence on rate of evaporation of water", *Chem. Eng. Prog.* , Vol. 46, no. 4, pp.172-175

Masoudi, M., and Sirignano, W. A., 2000, "Collision of a vortex with a vaporizing droplet", *International Journal of Multiphase Flow*, Vol. 26, pp. 1925-1949

Mathieu, J., Scott, J., 2000, *An introduction to turbulent flow*, Cambridge University Press

Megaridis, C. M., 1993, "Comparison between experimental measurements and numerical predictions of internal temperature distributions of a droplet vaporizing under high-temperature convective conditions", *Combust. Flame*, Vol. 93, pp. 287-302

Menter, F. R., 1994, "Two-Equation eddy-Viscosity Turbulence Models for Engineering applications", *AIAA Journal*, Vol.32, no. 8, pp.1598-1605

Morin, C., Chauveau, C. and Gökalp, I., 2000, "Droplet vaporization characteristics of vegetable oil derived biofuels at high temperatures", *Experimental Thermal and Fluid Science*, Vol.21, pp. 41-50

Neve, R. S., 1986,"The importance of turbulence macroscales in determining the drag coefficient of spheres", *Int. J. Heat and Fluid Flow*, Vol. 7, pp. 27-36

Neve, R. S., and Jaafar, F. B., 1982,"The importance of turbulence and surface roughness on the drag of spheres in thin jets", *The Aeronautical Journal,* Vol. 86, pp. 331-336

Neve, R. S., and Shansonga, 1989,"The effects of turbulence characteristics on sphere drag", *Int. J. Heat and Fluid Flow*, Vol. 10, pp. 318-321.

Niazmand, H., and Renksizbulut, M., 2005," Flow past a spinning sphere with surface blowing and heat transfer", *Journal of Fluids Engineering, Transactions of the ASME*, Vol. 127, no. 1, pp. 163-171

Ohta, Y., Shimoyama, K. and Ohigashi, S.V., 1975, "Vaporization and combustion of single liquid fuel droplets in turbulent environment", *Bulletin of JSME*, Vol. 18, pp. 47-56

Park, J-K., 1987, "Droplet Vaporization in Turbulent Flow", Ph.D. thesis, *University of Wisconsin-Madison,* USA

Patankar, S. V., 1978, "A Numerical Method for Conduction in Composite Materials, Flow in Irregular Geometries and Conjugate Heat Transfer," *in Proc. 6th Int. Heat Transfer Conf.*, Toronto, Canada, Vol. 3, pp. 297-302.

Patankar, S. V., 1980, *Numerical Heat Transfer and Fluid Flow*, Hemisphere Publishing Corporation

Patankar, S. V., 1991, "Computation of conduction and duct flow heat transfer," *Innovative Research*, Inc., Minneapolis, MN

Petrak, D., 1976, "Der Strömungswiderstand frei beweglicher einzel-undschwarmkugeln bei turbulenter anströmung entgegengesetzi zur bewegungsrichtung (Drag force of freely moving single and cloud spheres in case of counter current turbulent gas-solid flow)", Cheische Technik, Vol. 28, pp. 591-595.

Prakash, S., and Sirginano, W. A., 1978, "Liquid fuel droplet heating with internal circulation", *Int. J. Heat and Mass Transfer*, Vol. 21, pp. 885-895

Prakash, S., and Sirginano, W. A., 1980, "Theory of the Convective Droplet Vaporization with Unsteady Heat Transfer in the Circulating Liquid Phase", *Int. J. Heat and Mass Transfer*, Vol. 23, pp. 253-268.

Prandtl, L., 1925, "Bericht über untersuchungen zur ausgebildete Turbulenz", *ZAMM* 5: 136–139

Raithby, G. D., and Eckert, E. R. G., 1968, "The effect of turbulence parameters and support position on the heat transfer from spheres", *Int. J. Heat Mass Transfer*, Vol. 11, pp. 1233-1252

Refai-Ahmed, G., Yovanovich, M. M., and Culham, J. R., 1997, "Experimental and approximate analysis of forced convection and isothermal spheres", *Journal of Thermophysics and Heat Transfer*, Vol. 11, no. 2, pp. 223-231.

Renksizbulut, M., and Yuen, M. C., 1983a, "Numerical study of droplet evaporation in high temperature air stream", *J. of heat transfer*, Vol. 105, pp. 384-388

Renksizbulut, M., Nafziger, R. and Li, X., 1991, "A mass transfer correlation for droplet evaporation in high-temperature flows", Chem. Eng. Sci., Vol. 46, pp. 2351-2358

Reynolds, W. C., 1976, "Computation of turbulent flows", *Annual Review of Fluid Mechanics*, Vol. 8, pp. 183-208

Robert Y. S. Lai, and Desiraju B. Rao, 1976, "Wind drift currents in deep sea with variable eddy viscosity", Arch. Met. Geoph. Biokl., Ser. A, Vol. 25, pp. 131- 140

Roos, F. W., and Willmarth, W. W., 1971, "Some experimental results on sphere and disk drag", *AIAA J.*, Vol. 9, pp. 285-291

Rotta, J. C., 1951, "Statistiche Theorie Nichthomogener Turbulenz", Zeitschrift under Physik, bD 129, pp. 547-572

Rudoff, R. C., and Bachalo, W. D., 1988, "Measurement of droplet drag coefficients in polydispersed turbulent flow field", *AIAA Thermophysics, Plasmadynamics and Laser Conference Proceeding, San Antonio, Texas, USA*

Sandoval-Robles, J. G., Delmas, H., and Couderc, J. P., 1981, "Influence of turbulence on mass transfer between a liquid and a solid sphere", *A. I. Ch. E. Journal*, Vol. 27, pp. 819-823

Sankagiri, N., and Ruff, G. A., 1997, "Measurement of sphere drag in high turbulent intensity flows", *Proceeding of the ASME Fluids Engineering Division*, FED-Vol. 244, pp. 277-282

Sazhin, S. S., Abdelghaffar, W. A., Sazhina, E. M. and Heikal, M. R., 2005, "Models for droplet transient heating: Effects on droplet evaporation, ignition, and break-up", Int. J. of thermal Sciences, Vol. 44, pp. 610-622

Schlichting, H., 1979, *Boundary Layer Theory,* McGraw-Hill, New York, 7th edition

Spalart, P. R., and Allmaras, S. R., 1992, "A one-equation turbulence model for aerodynamics flows", 30th Aerospace Sciences Meeting & Exhibit, January 6-9, Reno, NV.

Spalding, D. B., 1972, "The k-ω model of turbulence", Imperial College, Mechanical Engineering Report TM/TN/A/16

Stone, H. L., 1968, "Iterative solution of implicit approximations of multidimensional partial differential equations, *SIAM J. Num. Anal.*, Vol. 5, pp. 530-558.

Sundararajan, T. and Ayyaswamy, P. S., 1984, "Hydrodynamics and heat transfer associated with condensation on a moving drop: solution of intermediate Reynolds number", *J. Fluid Mech.*, Vol. 149, pp. 33-58

Tennekes, H. and Lumley, J. L., 2001, *A first Course in Turbulence*, MIT Press

Torobin, L. B., and Gauvin, W. H., 1961, "Drag coefficients of single sphere moving in steady and accelerated motion in a turbulent fluid", *AIChE, J.*, Vol. 7, pp. 615-619

Uhlherr, P. and Sinclair, C., 1970, "The Effect of free-stream turbulence on the drag coefficient of freely entrained spheres," *Chemica' 70: A conference convened by Australian National Committee of the Institution of Chemical Engineers and Australian Academy of science*, pp. 1-13.

Van Doormall, J. P. and Raithby, G. D., 1984, "Enhancement of the simple method for predicting incompressible fluid flows", *Numerical Heat Transfer*, Vol. 7, pp. 147-163

Venezian, E., Crespo, M. J., and Sage, B. H., 1962, "Thermal and material transfer in turbulent gas stream: One inch spheres", *A. I. Ch. E. Journal*, Vol. 8, no. 3, pp. 383-388

Warnica, W. D., Renksizbulut, M., and Strong, A. B., 1995a, "Drag coefficient of spherical liquid droplets; Part 1: Quiescent gaseous fields", *Exp. Fluids,* Vol. 18, pp. 258-264

Warnica, W. D., Renksizbulut, M., and Strong, A. B., 1995b, "Drag coefficient of spherical liquid droplets; Part 2: Turbulent gaseous fields," *Exp. Fluids,* Vol. 18, pp. 265-276

Wilcox, D. C., 1988, "Reassessment of the scale-determining equation for advanced turbulence models", *AIAA Journal*, Vol. 26, no. 11, pp. 1299-1310

Wilcox, D. C., 1992,"The remarkable ability of turbulence model equations to describe transition", *Fifth Symposium on Numerical and Physical Aspects of Aerodynamic Flows, California State University, Long Beach, CA*, Jan. 13-15.

Wong, S-C., Lin, AR-C., 1992, "Internal temperature distributions of droplets vaporizing in high-temperature convective flows", *J. Fluid. Mech.*, Vol. 237, pp. 671-687

Wu, J–S., Hsu, K–H., Kuo, P-M., and Sheen, H–J., 2003, "Evaporation model of a single hydrocarbon fuel droplet due to ambient turbulence at intermediate Reynolds numbers," *Int. J. Heat Mass Transfer*, Vol. 46, pp. 4741-4745

Wu, J–S., Lin Y–J. and Sheen, H–J., 2001, "Effects of Ambient Turbulence and Fuel Properties on the Evaporation Rate of single Droplets," *Int. J. Heat Mass Transfer*, Vol. 44. pp. 4593-4603

Yang, Z., Shih, T.-H., 1993, "A new time scale based k-ε model for near wall turbulence", AIAA Journal Vol. 31, pp. 1191-1198

Yearling, P. R., 1995, Experimental determination of convective heat and mass transfer rates from single evaporating droplets in a turbulent air flow, Ph.D. thesis, North Carolina State University, USA

Yuge, T., 1959, "Experiments on Heat Transfer of Spheres— Report 3 (Influence of Free Stream Turbulence at Higher Reynolds Numbers)'', *Rep. Inst. High Sp. Mech. Japan*, Vol.11, 209-230

Yuge, T., 1960, "Experiments on heat transfer of spheres, including combined natural and forced convection", *J. Heat Transfer*, Vol. 82, pp. 214-220

Yusof, J., 1996, "Interaction of massive particles with turbulence", Ph.D. thesis, Department of Mechanical Engineering, Cornell University

Zarin, N. A., and Nicholls, J. S., 1971, "Sphere drag in solid rockets-non-continuum and turbulent fluids", *Combustion Science and Technology*, Vol. 3, pp. 273-285

Zhang, H., 2003, "Evaporation of a suspended droplet in forced convective high-pressure environment", C*ombust. Sci. and Tech.*, Vol. 175, pp. 2237-2268

Zhou, J. and Liu, J., 2004, "Numerical study on 3-d light and heat transport in biological tissues embedded with large blood vessels during laser-induced thermotherapy", *Numerical Heat Transfer A*, Vol. 45, pp. 415-449

Appendix A

DISCRETIZATION OF THE GOVERNING EQUATIONS

The governing equations for any transport process, i.e., the continuity equation and the convection/diffusion equations in the Cartesian coordinates, can be represented as

$$\left.\begin{aligned}\underbrace{\frac{\partial}{\partial t}(\rho\Phi)}_{\substack{Unsteady\\ term}}+\underbrace{\frac{\partial}{\partial x}(\rho U\Phi)+\frac{\partial}{\partial y}(\rho V\Phi)+\frac{\partial}{\partial z}(\rho W\Phi)}_{Convection\ terms}=\\ \underbrace{\frac{\partial}{\partial x}\left\{\Gamma_\Phi\frac{\partial\Phi}{\partial x}\right\}+\frac{\partial}{\partial y}\left\{\Gamma_\Phi\frac{\partial\Phi}{\partial y}\right\}+\frac{\partial}{\partial z}\left\{\Gamma_\Phi\frac{\partial\Phi}{\partial z}\right\}}_{Convection\ terms}+\underbrace{S_\Phi}_{\substack{Source\\ term}}\end{aligned}\right\}. \tag{A.1}$$

By integrating the equation above over a control volume, which is shown in Figure A.1, and a time interval, Δt, Eq. (A.1) becomes

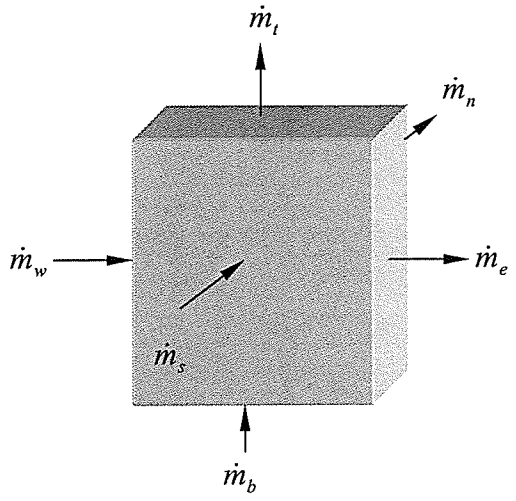

Figure A.1 Mass flow through a typical control volume

$$\left.\begin{aligned}
&\underbrace{\int_t^{t+\Delta t}\int_{V_p}\frac{\partial}{\partial t}(\rho\Phi)dV_p dt}_{\text{I}}+\underbrace{\int_t^{t+\Delta t}\int_{V_p}\frac{\partial}{\partial x}(\rho U\Phi)dV_p dt}_{\text{II}}+\underbrace{\int_t^{t+\Delta t}\int_{V_p}\frac{\partial}{\partial x}(\rho V\Phi)dV_p dt}_{\text{III}}+\\
&\underbrace{\int_t^{t+\Delta t}\int_{V_p}\frac{\partial}{\partial x}(\rho W\Phi)dV_p dt}_{\text{IV}}=\underbrace{\int_t^{t+\Delta t}\int_{V_p}\frac{\partial}{\partial x}\left\{\Gamma_\Phi\frac{\partial\Phi}{\partial x}\right\}dV_p dt}_{\text{V}}+\\
&\underbrace{\int_t^{t+\Delta t}\int_{V_p}\frac{\partial}{\partial y}\left\{\Gamma_\Phi\frac{\partial\Phi}{\partial y}\right\}dV_p dt}_{\text{VI}}+\underbrace{\int_t^{t+\Delta t}\int_{V_p}\frac{\partial}{\partial z}\left\{\Gamma_\Phi\frac{\partial\Phi}{\partial z}\right\}dV_p dt}_{\text{VII}}\\
&\underbrace{\int_t^{t+\Delta t}\int_{V_p}S_\Phi dV_p dt}_{\text{VIII}}
\end{aligned}\right\}. \qquad \text{(A.2)}$$

The integration of the first term of Eq. (A.2) gives

$$\text{I}=\int_t^{t+\Delta t}\int_{V_p}\frac{\partial}{\partial t}(\rho\Phi)dV_p dt\cong\left(\rho_P\Phi_P-\rho_P^0\Phi_P^0\right)V_P\cong\left(\dot{Q}_P\Phi_P-\dot{Q}_P^0\Phi_P^0\right), \qquad \text{(A.3)}$$

where the superscript "0" refers to the old precedent value.

The integration of the second term of Eq. (A.2) results in

$$\left.\begin{aligned} \mathrm{II} = \int_t^{t+\Delta t}\int_{V_p}\frac{\partial}{\partial x}(\rho U\Phi)d\mathrm{V}_p dt = \int_t^{t+\Delta t}\int_{V_p}\frac{\partial}{\partial x}(\rho U\Phi)dxdA_p dt = \int_t^{t+\Delta t}\int_w^e\frac{\partial}{\partial x}(\rho U\Phi A)dx = \\ \int_t^{t+\Delta t}\left[(\rho U\Phi A)_e-(\rho U\Phi A)_w\right]dt = \int_t^{t+\Delta t}(\dot{m}_e\Phi_e-\dot{m}_w\Phi_w)dt = \\ f_t(\dot{m}_e\Phi_e-\dot{m}_w\Phi_w)+(1-f_t)(\dot{m}_e\Phi_e-\dot{m}_w\Phi_w)^0 \end{aligned}\right\}, \quad (A.4)$$

where f_t is a weighting factor which ranges between 0 and 1 depending on the scheme used, that is

$$f_t=\begin{cases}0 & \text{Explicit scheme}\\ 0.5 & \text{Crank - Nicolson scheme}\\ 1 & \text{Fully implicit scheme}\end{cases}$$

Using a fully implicit scheme, Eq. (A.4) becomes

$$\mathrm{II} = \int_t^{t+\Delta t}\int_{V_p}\frac{\partial}{\partial x}(\rho U\Phi)d\mathrm{V}_p dt = (\dot{m}_e\Phi_e-\dot{m}_w\Phi_w)\Delta t\,. \quad (A.5)$$

Introducing a convection weighting factor α, Φ_e and Φ_w can be approximated as

$$\Phi_e=\left(\frac{1}{2}+\alpha_e\right)\Phi_P+\left(\frac{1}{2}-\alpha_e\right)\Phi_E, \quad (A.6)$$

$$\Phi_w=\left(\frac{1}{2}+\alpha_w\right)\Phi_W+\left(\frac{1}{2}-\alpha_w\right)\Phi_P. \quad (A.7)$$

Substituting Φ_e and Φ_w into Eq. (A.5) leads to

$$\mathrm{II} = \int_{t}^{t+\Delta t}\int_{V_p}\frac{\partial}{\partial x}(\rho U\Phi)d\mathrm{V}_p dt = \left\{\dot{m}_e\left(\frac{1}{2}+\alpha_e\right)\Phi_P + \dot{m}_e\left(\frac{1}{2}-\alpha_e\right)\Phi_E\right\} - \left\{\dot{m}_w\left(\frac{1}{2}+\alpha_w\right)\Phi_W + \dot{m}_w\left(\frac{1}{2}-\alpha_w\right)\Phi_P\right\} = \dot{m}_e\left(\frac{1}{2}-\alpha_e\right)\Phi_E - \dot{m}_w\left(\frac{1}{2}+\alpha_w\right)\Phi_W + \left\{\dot{m}_e\left(\frac{1}{2}+\alpha_e\right) - \dot{m}_w\left(\frac{1}{2}-\alpha_w\right)\right\}\Phi_P \quad \text{(A.6)}$$

The integration of the third and fourth terms of Eq. (A.2) are calculated in a similar manner to the second term of Eq. (A.2) so that

$$\mathrm{III} = \int_{t}^{t+\Delta t}\int_{V_p}\frac{\partial}{\partial x}(\rho V\Phi)d\mathrm{V}_p dt = \dot{m}_t\left(\frac{1}{2}-\alpha_t\right)\Phi_T - \dot{m}_b\left(\frac{1}{2}+\alpha_b\right)\Phi_B + \left\{\dot{m}_t\left(\frac{1}{2}+\alpha_t\right) - \dot{m}_w\left(\frac{1}{2}-\alpha_b\right)\right\}\Phi_P \quad \text{(A.7)}$$

$$\mathrm{IV} = \int_{t}^{t+\Delta t}\int_{V_p}\frac{\partial}{\partial x}(\rho W\Phi)d\mathrm{V}_p dt = \dot{m}_n\left(\frac{1}{2}-\alpha_n\right)\Phi_N - \dot{m}_s\left(\frac{1}{2}+\alpha_s\right)\Phi_S + \left\{\dot{m}_n\left(\frac{1}{2}+\alpha_n\right) - \dot{m}_s\left(\frac{1}{2}-\alpha_s\right)\right\}\Phi_P \quad \text{(A.8)}$$

The first term in the diffusion terms, i.e., term V of right hand side of Eq. (A.2), is calculated as follows

$$\left.\begin{aligned} V = \int_t^{t+\Delta t}\int_{V_p}\frac{\partial}{\partial x}\left\{\Gamma_\phi\frac{\partial\Phi}{\partial x}\right\}dV_p dt &= \int_t^{t+\Delta t}\int_e^w \frac{\partial}{\partial x}\left\{\Gamma_\phi\frac{\partial\Phi}{\partial x}\right\}dx dA_p dt \\ &= \int_t^{t+\Delta t}\left\{\left(\Gamma_\phi A\frac{\partial\Phi}{\partial x}\right)_e - \left(\Gamma_\phi A\frac{\partial\Phi}{\partial x}\right)_w\right\}dt \end{aligned}\right\}. \quad \text{(A.9)}$$

Introducing a diffusion weighting factor β, the gradients of the parameter Φ can be approximated as

$$\left(\frac{\partial\Phi}{\partial x}\right)_e = \beta_e\left\{\frac{(\Phi_E - \Phi_P)}{(\delta x)_e}\right\}, \quad \text{(A.10)}$$

$$\left(\frac{\partial\Phi}{\partial x}\right)_w = \beta_w\left\{\frac{(\Phi_P - \Phi_W)}{(\delta x)_w}\right\}. \quad \text{(A.11)}$$

Substituting $(\partial\Phi/\partial x)_e$ and $(\partial\Phi/\partial x)_w$ into Eq. (A.9) and using the fully implicit scheme, Eq. (A.9) becomes

$$\left.\begin{aligned} V = \int_t^{t+\Delta t}\left\{\left(\frac{\Gamma_\phi A\beta}{\delta x}\right)_e(\Phi_E - \Phi_P) - \left(\frac{\Gamma_\phi A\beta}{\delta x}\right)_w(\Phi_P - \Phi_W)\right\}dt \\ = \left\{\left(\frac{\Gamma_\phi A\beta}{\delta x}\right)_e(\Phi_E - \Phi_P) - \left(\frac{\Gamma_\phi A\beta}{\delta x}\right)_w(\Phi_P - \Phi_W)\right\}\Delta t \end{aligned}\right\}. \quad \text{(A.12)}$$

Terms VI and VII of the right hand side of Eq. (A.2) can be manipulated following the same way as for term V:

$$VI = \int_{t}^{t+\Delta t} \int_{V_p} \frac{\partial}{\partial y}\left\{\Gamma_\phi \frac{\partial \Phi}{\partial y}\right\} dV_p dt$$
$$= \left\{\left(\frac{\Gamma_\phi A\beta}{\delta y}\right)_t (\Phi_T - \Phi_P) - \left(\frac{\Gamma_\phi A\beta}{\delta y}\right)_b (\Phi_P - \Phi_B)\right\}\Delta t \Bigg\}, \quad \text{(A.13)}$$

and

$$\mathrm{VII} = \int_{t}^{t+\Delta t} \int_{V_p} \frac{\partial}{\partial z}\left\{\Gamma_\phi \frac{\partial \Phi}{\partial z}\right\} dV_p dt$$
$$= \left\{\left(\frac{\Gamma_\phi A\beta}{\delta z}\right)_t (\Phi_N - \Phi_P) - \left(\frac{\Gamma_\phi A\beta}{\delta z}\right)_b (\Phi_P - \Phi_S)\right\}\Delta t \Bigg\}. \quad \text{(A.14)}$$

The integration of the source term, i.e., term VIII of Eq. (A.2), is approximated as follow

$$\mathrm{VIII} = \int_{t}^{t+\Delta t} \int_{V_p} S_\Phi dV_p dt \cong \int_{t}^{t+\Delta t} \int_{V_p} (S_C + S_P \Phi_P) dV_p dt$$
$$\cong (S_C V_P + S_P V_P \Phi_P)\Delta t$$
$$\cong (Q_P + R_P \Phi_P)\Delta t \Bigg\}. \quad \text{(A.15)}$$

Substituting Eqs.(A.3-A.15) into Eq. (A.2) and dividing by Δt we can obtain the discritized form of Eq. (A.1) becomes

$$
\begin{aligned}
&\left(\dot{Q}_P\Phi_P - \dot{Q}_P^0\Phi_P^0\right) + \dot{m}_e\left(\frac{1}{2}-\alpha_e\right)\Phi_E - \dot{m}_w\left(\frac{1}{2}+\alpha_w\right)\Phi_W \\
&\quad + \left\{\dot{m}_e\left(\frac{1}{2}+\alpha_e\right) - \dot{m}_w\left(\frac{1}{2}-\alpha_w\right)\right\}\Phi_P \\
&\quad + \dot{m}_t\left(\frac{1}{2}-\alpha_t\right)\Phi_T - \dot{m}_b\left(\frac{1}{2}+\alpha_b\right)\Phi_B \\
&\quad + \left\{\dot{m}_t\left(\frac{1}{2}+\alpha_t\right) - \dot{m}_w\left(\frac{1}{2}-\alpha_b\right)\right\}\Phi_P \\
&\quad + \dot{m}_n\left(\frac{1}{2}-\alpha_n\right)\Phi_N - \dot{m}_s\left(\frac{1}{2}+\alpha_s\right)\Phi_S \\
&\quad + \left\{\dot{m}_n\left(\frac{1}{2}+\alpha_n\right) - \dot{m}_s\left(\frac{1}{2}-\alpha_s\right)\right\}\Phi_P \\
&= \left\{\left(\frac{\Gamma_\phi A\beta}{\delta x}\right)_e\left(\Phi_E-\Phi_P\right) - \left(\frac{\Gamma_\phi A\beta}{\delta x}\right)_w\left(\Phi_P-\Phi_W\right)\right\} \\
&\quad + \left\{\left(\frac{\Gamma_\phi A\beta}{\delta y}\right)_t\left(\Phi_T-\Phi_P\right) - \left(\frac{\Gamma_\phi A\beta}{\delta y}\right)_b\left(\Phi_P-\Phi_B\right)\right\} \\
&\quad + \left\{\left(\frac{\Gamma_\phi A\beta}{\delta z}\right)_t\left(\Phi_N-\Phi_P\right) - \left(\frac{\Gamma_\phi A\beta}{\delta z}\right)_b\left(\Phi_P-\Phi_S\right)\right\} \\
&\quad + \left(Q_P + R_P\Phi_P\right)
\end{aligned}, \qquad \text{(A.16)}
$$

Rearranging the equation above leads to a general equation

$$
a_P\Phi_P = a_E\Phi_E + a_W\Phi_W + a_N\Phi_N + a_S\Phi_S + a_T\Phi_T + a_B\Phi_B + b_\Phi, \qquad \text{(A.17)}
$$

where the coefficients $a_P, a_E, a_W, a_N, a_S, a_T, a_B$ and b_Φ are expressed as:

$$
a_E = \beta_e D_e + \dot{m}_e\alpha_e - \frac{\dot{m}_e}{2}, \qquad \text{(A.18)}
$$

$$a_W = \beta_w D_w + \dot{m}_w \alpha_w + \frac{\dot{m}_w}{2}, \tag{A.19}$$

$$a_N = \beta_n D_n + \dot{m}_n \alpha_n - \frac{\dot{m}_n}{2}, \tag{A.20}$$

$$a_S = \beta_s D_s + \dot{m}_s \alpha_s + \frac{\dot{m}_s}{2}, \tag{A.21}$$

$$a_T = \beta_t D_t + \dot{m}_t \alpha_e - \frac{\dot{m}_t}{2}, \tag{A.22}$$

$$a_B = \beta_b D_b + \dot{m}_b \alpha_b + \frac{\dot{m}_b}{2}, \tag{A.23}$$

$$a_P = a_E + a_W + a_T + a_B + a_N + a_S + \left(\frac{\dot{Q}_P}{\Delta t} - R_P \right), \tag{A.24}$$

$$b_\Phi = \frac{\dot{Q}_P^0}{\Delta t} \Phi_P^0 + Q_P . \tag{A.25}$$

The corresponding conductances D_e, D_w, D_t, D_b, D_n and D_s are defined as

$$\left.\begin{aligned} D_e &= \frac{2\Gamma_e A_e}{(\Delta x_E + \Delta x_P)} \\ D_w &= \frac{2\Gamma_w A_w}{(\Delta x_W + \Delta x_P)} \\ D_t &= \frac{2\Gamma_t A_t}{(\Delta y_T + \Delta y_P)} \\ D_b &= \frac{2\Gamma_b A_b}{(\Delta y_B + \Delta y_P)} \\ D_n &= \frac{2\Gamma_n A_n}{(\Delta z_N + \Delta z_P)} \\ D_s &= \frac{2\Gamma_s A_s}{(\Delta z_S + \Delta z_P)} \end{aligned}\right\}. \tag{A.20}$$

The mass flow rates $\dot{m}_e, \dot{m}_w, \dot{m}_t, \dot{m}_b, \dot{m}_n$, and $\dot{m}_s$ are defined as

$$\left.\begin{aligned} \dot{m}_e &= \rho_e A_e U_e \\ \dot{m}_w &= \rho_w A_w U_w \\ \dot{m}_t &= \rho_t A_t U_t \\ \dot{m}_b &= \rho_b A_b U_b \\ \dot{m}_n &= \rho_n A_n U_n \\ \dot{m}_s &= \rho_s A_s U_s \end{aligned}\right\}, \tag{A.21}$$

where A_e, A_w, A_t, A_b, A_n and A_s are given as

$$\left.\begin{aligned} A_e &= \Delta x \Delta y \\ A_w &= \Delta x \Delta y \\ A_t &= \Delta z \Delta x \\ A_b &= \Delta z \Delta x \\ A_n &= \Delta y \Delta z \\ A_s &= \Delta y \Delta z \end{aligned}\right\}. \tag{A.22}$$

The diffusion coefficient Γ_Φ at the control volume faces $(\Gamma_\Phi)_e$, $(\Gamma_\Phi)_t$, and $(\Gamma_\Phi)_n$ can be calculated by assuming a harmonic mean of the diffusion coefficients of the two control volumes around each face as

$$\left.\begin{aligned} (\Gamma_\Phi)_e &= \left(\frac{1-f_e}{(\Gamma_\Phi)_P} + \frac{f_e}{(\Gamma_\Phi)_E}\right)^{-1} \\ (\Gamma_\Phi)_t &= \left(\frac{1-f_t}{(\Gamma_\Phi)_P} + \frac{f_t}{(\Gamma_\Phi)_T}\right)^{-1} \\ (\Gamma_\Phi)_n &= \left(\frac{1-f_n}{(\Gamma_\Phi)_P} + \frac{f_n}{(\Gamma_\Phi)_N}\right)^{-1} \end{aligned}\right\}, \tag{A.23}$$

whereas the coefficients f_e, f_t and f_n can be defined as

$$\left.\begin{aligned} f_e &= \frac{\Delta x_E}{\Delta x_E + \Delta x_P} \\ f_t &= \frac{\Delta y_t}{\Delta y_T + \Delta y_P} \\ f_n &= \frac{\Delta z_n}{\Delta z_N + \Delta z_P} \end{aligned}\right\}. \tag{A.24}$$

The convection weighting factors, α_e, α_t and α_n are expressed by using an approximation to EDS (Exponential Differencing Scheme) as follow

$$\left.\begin{aligned} \alpha_e &= \frac{1}{2} \times \frac{(\dot{m}_e / D_e)^2}{5 + (\dot{m}_e / D_e)^2} \\ \alpha_t &= \frac{1}{2} \times \frac{(\dot{m}_t / D_t)^2}{5 + (\dot{m}_t / D_t)^2} \\ \alpha_n &= \frac{1}{2} \times \frac{(\dot{m}_n / D_n)^2}{5 + (\dot{m}_n / D_n)^2} \end{aligned}\right\}. \tag{A.25}$$

The diffusion weighting factors, β_e, β_t and β_n are also given as

$$\left.\begin{aligned} \beta_e &= \frac{1 + 0.005(\dot{m}_e / D_e)^2}{1 + 0.05(\dot{m}_e / D_e)^2} \\ \beta_t &= \frac{1 + 0.005(\dot{m}_t / D_t)^2}{1 + 0.05 + (\dot{m}_t / D_t)^2} \\ \beta_n &= \frac{1 + 0.005(\dot{m}_n / D_n)^2}{1 + 0.05(\dot{m}_n / D_n)^2} \end{aligned}\right\}. \tag{A.26}$$

Appendix B

SOLUTION APPROACH FOR A SYSTEM OF ALGEBRAIC EQUATIONS

The discretization of the convection/diffusion equation (Eq. (A.2)) by using the Finite Volume scheme provides an algebraic equation (Eq. (A.17)) at each grid node. This equation (Eq. (A.17)) is a function of the diffusion parameter at that node as well as at the neighborhood nodes. By using this scheme for all control volumes in the computational domain produces a system of algebraic equations that can be easily formulated in a matrix form. Two techniques can be used to solve this system of algebraic equations: direct and iterative solution techniques. Direct solution technique allows to achieve solution of the entire system of equations simultaneously in one run. This technique has the demerit for its high time and memory demand. However, the iterative technique is based on repeating the solution procedure over the matrix by using an approximate guessed solution of the system until predefined convergence criteria is achieved. This

technique is very cheap in terms of memory and computing time. In the following only the iterative technique, used in the present code, is discussed.

B.1 Point Successive Over Relaxation Method (SOR)

The linear equation produced from discretizing the convection/diffusion equation is

$$a_P\Phi_P = a_E\Phi_E + a_W\Phi_W + a_N\Phi_N + a_S\Phi_S + a_T\Phi_T + a_B\phi_B + b_\Phi, \tag{B.1}$$

where all symbols and coefficients of this equation are defined in Appendix A. This equation can be solved by using Jacobi method as follow

$$\Phi_P^{n+1} = \frac{a_E\Phi_E^n + a_W\Phi_W^n + a_N\Phi_N^n + a_S\Phi_S^n + a_T\Phi_T^n + a_B\phi_B^n + b_\Phi}{a_P}, \tag{B.2}$$

where n and $n+1$ are the previous and new iterations.

Sweeping the entire computational domain in x, y and z directions stands only for one iteration, and the iteration process continue until the desired convergence is achieved. This method generally takes a long time to converge. Gauss-Sidel modified this method in order to speed its convergence by using the newest values of Φ_W, Φ_S and Φ_B as follow

$$\Phi_P^{n+1} = \frac{a_E\Phi_E^n + a_W\Phi_W^{n+1} + a_N\Phi_N^n + a_S\Phi_S^{n+1} + a_T\Phi_T^n + a_B\phi_B^{n+1} + b_\Phi}{a_P} \tag{B.3}$$

The Gauss-Sidel method can accelerate the convergence of the solution by introducing a parameter called overrelaxation factor, χ. This method is called successive over relaxation (SOR) when $\chi>1$ and is formulated as

$$a_P\hat{\Phi}_P = a_E\Phi_E^n + a_W\Phi_W^{n+1} + a_N\Phi_N^n + a_S\Phi_S^{n+1} + a_T\Phi_T^n + a_B\phi_B^{n+1} + b_\Phi, \tag{B.4}$$

$$\hat{\Phi}_P = \frac{\Phi_P^{n+1} - (1-\chi)\Phi_P^n}{\chi} = \frac{\Phi_P^{n+1}}{\chi} - \left(\frac{1}{\chi} - 1\right)\Phi_P^n, \tag{B.5}$$

and

$$\left.\begin{aligned}\Phi_P^{n+1} = \frac{\chi\left(a_E\Phi_E^n + a_W\Phi_W^{n+1} + a_N\Phi_N^n + a_S\Phi_S^{n+1} + a_T\Phi_T^n + a_B\phi_B^{n+1} + b_\Phi\right)}{a_P} \\ + \left(\frac{1}{\chi} - 1\right)\Phi_P^n\end{aligned}\right\} \quad \text{(B.6)}$$

The relaxation factor ranges between 0 and 2 so that

Under relaxation: $0 < \chi < 1$

Gauss-Sidel: $\chi = 1$

SOR: $1 < \chi < 2$

B.2 Line Successive Over Relaxation (LSOR)

The linear equation produced from discretizing the convection/diffusion equation (Eq. (A.1)) has the following form

$$a_P\Phi_P = a_E\Phi_E + a_W\Phi_W + a_N\Phi_N + a_S\Phi_S + a_T\Phi_T + a_B\phi_B + b_\Phi$$

For a constant row (x-direction) we can write

$$\left.\begin{aligned}a_P\Phi_P^{n+1/2m} = a_E\Phi_E^n + a_W\Phi_W^{n+1/2m} + a_T\Phi_T^{n+1/2m} + a_B\phi_B^{n+1/2m} \\ + \left(a_N\hat{\Phi}_N + a_S\Phi_S^{n+1/2m} + b_\phi\right)\end{aligned}\right\}, \quad \text{(B.7)}$$

where

$$\left.\begin{aligned}\hat{\Phi}_N &= (2-\chi)\Phi_N^n + (\chi-1)\Phi_N^{n+1/2m} \\ &= \Phi_N^n - (\chi-1)\Phi_N^n + (\chi-1)\Phi_N^{n+1/2m} \\ &= \Phi_N^n + (\chi-1)\left[\Phi_N^{n+1/2m} - \Phi_N^n\right]\end{aligned}\right\} \quad \text{(B.8)}$$

With the assumption $\Phi_N^{n+1/2m} - \Phi_N^n \cong \Phi_P^{n+1/2m} - \Phi_P^n$, Eq. (B.8) becomes

$$\hat{\Phi}_N = \Phi_N^n + (\chi-1)\left[\Phi_P^{n+1/2m} - \Phi_P^n\right] \quad \text{(B.9)}$$

Substituting Eq. (B.9) into Eq. (B.7) we obtain

$$\left.\begin{aligned}\left[a_P-(\chi-1)\right]\Phi_P^{n+1/2m}=a_E\Phi_E^{n+1/2m}+a_W\Phi_W^{n+1/2m}+\\ \left\{a_T\Phi_T^{n+1/2m}+a_B\phi_B^{n+1/2m}+a_S\Phi_S^{n+1/2m}+a_N\left[\Phi_N^n-(\chi-1)\Phi_P^n\right]+b_\phi\right\}\end{aligned}\right\} \quad \text{(B.10)}$$

Similarly for a constant column in y-direction we have

$$\left.\begin{aligned}\left[a_P-(\chi-1)\right]\Phi_P^{n+1/m}=a_N\Phi_N^{n+1/m}+a_S\Phi_S^{n+1/m}+\\ \left\{a_T\Phi_T^{n+1/m}+a_B\phi_B^{n+1/m}+a_W\Phi_W^{n+1/m}+a_E\left[\Phi_E^{n+1/m}-(\chi-1)\Phi_P^{n+1/m}\right]+b_\phi\right\}\end{aligned}\right\} \quad \text{(B.11)}$$

The last two equations, i.e., Eqs. (B.10) and (B.11)), can be generalized as:

$$A_i\Phi_i=A_{i+1}\Phi_{i+1}+A_{i-1}\Phi_{i-1}+B \quad \text{(B.12)}$$

This type of equations, i.e., (B.10) and (B.11), can be efficiently solved by using tri-diagonal matrix algorithm (TDMA). In case of a three dimensional problem, the sweep in x-direction and y-direction is first performed for a constant plane in z-direction, i.e., k=1. The plane is then switched to k=2, 3,... , m, where m is the last plane in z-direction. A single iteration is achieved once the plane m is completed. Usually the number of iterations required in order for this method to converge is less than that required in SOR method.

B.3 Strongly Implicit Procedure (SIP)

One of the most popular iterative methods for solving a set of linear equations is the Strongly Implicit Procedure (SIP) developed by Stone (1968). This method is developed for solving two-dimensional differential equations. Leister and Peric (1994) extended this method for three-dimensional problems.

Recall that Eq. (B.1) can be represented in a matrix form as

$$[a]_{N\times N}\{\Phi\}_{N\times 1}=\{b\}_{N\times 1}, \quad \text{(B.13)}$$

where $[a]$ is a matrix that has zero elements except in the seven diagonals and, N is the total number of control volumes in the computational domain, which can be expressed as

$$N = N_x \times N_y \times N_z = NI \times NJ \times NK \tag{B.14}$$

The variable parameter Φ is stored in one dimensional storage location with the following indices

$$ijk = (k-1)NIJ + (i-1)NJ + j\,,$$

where $i = 1,2,....,NI$, $j = 1,2,.....,NJ$, $k = 1,2,....,NK$ and $NIJ = NI \times NJ$

The iterative solution of Eq. (B.13) is assumed to be

$$[M]\{\Phi^{n+1}\} = \{b\} - [a - M]\{\Phi^n\}. \tag{B.15}$$

The matrix $[M]$ has been chosen so that

$$[M]\{\delta^n\} = \{R^n\} \tag{B.16}$$

where $\{\delta^n\}$ is the change in the variable Φ from iteration n to $n+1$ and, $\{R^n\}$ is the residual after the elapse of n iterations, which can be expressed as

$$\{R^n\} = \{b\} - [a]\{\Phi^n\} \tag{B.17}$$

Decomposing $[M]$ to $[L]$ and $[U]$ as

$$[M] = [L][U] \tag{B.18}$$

The structures of $[L]$ and $[U]$ have the following form

$$[M] = \begin{bmatrix} \diagdown & & \\ \diagdown & \diagdown & \\ & \diagdown & \diagdown \end{bmatrix} \begin{bmatrix} \diagdown & & \\ & \diagdown & \\ & & \diagdown \end{bmatrix}$$

where the diagonals from the left to the right represent L_B, L_W, L_S, L_P, U_P, U_N, U_E and U_T. Note that elements in the diagonal U_P are unity. The elements of $[L]$ and $[U]$ are calculated as

$$L_{B,ijk} = a_{B,ijk} \Big/ \left[1 + \mathrm{X}\left(U_{N,ijk-NIJ} + U_{E,ijk-NIJ}\right)\right] \tag{B.19}$$

$$L_{W,ijk} = a_{W,ijk} \Big/ \left[1 + \mathrm{X}\left(U_{N,ijk-NJ} + U_{T,ijk-NJ}\right)\right] \tag{B.20}$$

$$L_{S,ijk} = a_{S,ijk} \Big/ \left[1 + \mathrm{X}\left(U_{E,ijk-1} + U_{T,ijk-1}\right)\right] \tag{B.21}$$

$$\left.\begin{aligned} L_{P,ijk} = a_{P,ijk} + H_1 + H_2 + H_3 - L_{B,ijk}U_{T,ijk-NIJ} \\ - L_{W,ijk}U_{E,ijk-NJ} - L_{S,ijk}U_{N,ijk-1} \end{aligned}\right\} \tag{B.22}$$

$$U_{N,ijk} = \left(a_{N,ijk} - H_1\right) \Big/ L_{P,ijk} \tag{B.23}$$

$$U_{E,ijk} = \left(a_{E,ijk} - H_2\right) \Big/ L_{P,ijk} \tag{B.24}$$

$$U_{T,ijk} = \left(a_{T,ijk} - H_3\right) \Big/ L_{P,ijk} \tag{B.25}$$

where

$$H_1 = \mathrm{X}\left(L_{B,ijk}U_{N,ijk-NIJ} + L_{W,ijk}U_{N,ijk-NJ}\right) \tag{B.26}$$

$$H_2 = \mathrm{X}\left(L_{B,ijk}U_{E,ijk-NIJ} + L_{S,ijk}U_{E,ijk-1}\right) \tag{B.27}$$

$$H_3 = \mathrm{X}\left(L_{W,ijk}U_{T,ijk-NJ} + L_{S,ijk}U_{T,ijk-1}\right) \tag{B.28}$$

The value of X (i.e., an iteration parameter in the Stone's solver) should be around 0.92 and lower than 0.95 to avoid divergence. If the value of X is zero, then the SIP solver converts to standard Incomplete Lower-Upper (ILU) decomposition. The optimum values of X represent undesirable features of the SIP procedure. Leister and Peric (1994) suggested an optimum range of X to be within 0.92 to 0.94. This range gives realistic results for a considerable number of fluids flow problems.

Note that the elements of $[L]$ and $[U]$ corresponding to the boundaries of the nodes are assumed to be zero.

The elements of $\{\delta^n\}$ can be calculated by introducing auxiliary matrix $\{Q^n\}$ as

$$\left\{Q^n\right\} = \left[L^{-1}\right]\left\{R^n\right\} \tag{B.29}$$

with increment matrix $\{\delta\}$

$$\{\delta^n\} = [U^{-1}]\{Q^n\} \tag{B.30}$$

These two equations are solved by forward and backward substitutions as follow

$$Q^n_{ijk} = \left(R^n_{ijk} - L_{B,ijk}Q^n_{ijk-NIJ} - L_{W,ijk}Q^n_{ijk-NJ} - L_{S,ijk}Q^n_{ijk-1}\right)/L_{P,ijk} \tag{B.31}$$

$$\delta^n_{ijk} = Q^n_{ijk} - U_{N,ijk}\delta^n_{ijk+1} - U_{E,ijk}\delta^n_{ijk+NJ} - U_{T,ijk}Q^n_{ijk+NIJ}$$

where

$$\left.\begin{aligned} R^m_{ijk} = b_{ijk} - a_{P,ijk}\Phi^n_{ijk} - a_{E,ijk}\Phi^n_{ijk+NJ} - a_{W,ijk}\Phi^n_{ijk-NJ} - a_{N,ijk}\Phi^n_{ijk+1} \\ - a_{S,ijk}\Phi^n_{ijk-1} - a_{T,ijk}\Phi^n_{ijk+NIJ} - a_{B,ijk}\Phi^n_{ijk-NIJ} \end{aligned}\right\} \tag{B.32}$$

Once the increment matrix $\{\delta^n\}$ is obtained, the new values of $\{\Phi^{n+1}\}$ can be then calculated as

$$\{\Phi^{n+1}\} = \{\Phi^n\} + \{\delta^n\} \tag{B.33}$$

Appendix C

THERMODYNAMIC PROPERTIES

The temperature dependent thermodynamic properties of liquid and vapor species of *n*-heptane and *n*-decane droplets and the carrier gas (air) are calculated by using the expressions and table provided below. These expressions are established and collected from many references, such as Reid *et al* (1977)[‡], Perry (1997)[§], Heywood and Renksizbulut (1986)[**] and, Abramzon and Sirignano (1989)[††] Note that the temperature, T, in these correlations is expressed in Kelvin. However, some liquid properties of *n*-decane are assumed constant as they are lacking in the open literature.

➢ *n*-heptane (Liquid-phase)

[‡] Reid, R., Prausnitz, J. M. and Sherwood, T. K., *The Properties of gases and liquids*, McGraw-Hill, 2nd edition, 1977

[§] Perry, R. H., Perry's chemical engineers' handbook, McGraw Hill, 7th edition, 1997

[**] Haywood, R. J., Renksizbulut, M., 1986, "On variable-properties, blowing, and transient effects in convective droplet evaporation with internal circulation", Proc. 8th Int. Heat transfer Confer., San Francisco, Calf., pp. 1861-1866

[††] Abramzon, B. and Sirignano, W. A., 1989, "Droplet vaporization model for spray combustion calculations", Int. J. Heat Mass Transfer, Vol. 3, pp.1605-1618

- Density $\rho = 136.12(556.0 - T)^{0.29}$ (C1)
- Viscosity $\mu = 1.57 \times 10^{-5} \exp(962.1/T)$ (C2)
- Conductivity $\lambda = 0.041868(5.265 \times 10^{-4} - 7.857 \times 10^{-7} T)$ (C3)
- Specific heat $c_p = 4186.8(0.455 - 3.461 \times 10^{-4} T + 2.148 \times 10^{-6} T^2)$ (C4)

➢ *n*-decane (Liquid-phase)

- Density $\rho = 58.402 \times 3.9578^{1+\left(1-\frac{T}{617.6}\right)^{2/7}}$ (C5)
- Viscosity $\mu = 1.16 \times 10^{-5} \exp(1286.2/T)$ (C6)
- Conductivity $\lambda = 0.129$ (C7)
- Specific heat $c_p = 2220.0$ (C8)

➢ *n*-heptane (Gas-phase)

- Density $\rho = 1221/T$ (C9)
- Viscosity $\mu = 2.0 \times 10^{-8} T$ (C10)
- Conductivity $\lambda = 4.865 \times 10^{-11} T^{1.786}$ (C11)
- Specific heat $c_p = 4186.8(0.0575 + 0.001298T - 4.444 \times 10^{-7} T^2)$ (C12)
- Diffusion $D_{AB} = 3.341 \times 10^{-5} T^{1.75} p^{-1}$ (C13)

➢ *n*-decane (Gas-phase)

- Density $\rho = 1731/T$ (C14)

- Viscosity $\mu = 5.64\times10^{-6} + 1.75\times10^{-8}(T-300)$ (C15)

- Specific heat (C16)

$$c_p = 106.6 + 5.76T - 1.67\times10^{-3}T^2 - 4.73\times10^{-7}T^3 \quad \cdots T < 800$$

$$c_p = 410.9 + 5.46T - 2.487\times10^{-3}T^2 + 4.23\times10^{-7}T^3 \quad \cdots T \geq 800 \quad \text{(C17)}$$

- Diffusion $D_{AB} = 2.761\times10^{-5}T^{1.75}p^{-1}$ (C18)

Changes of thermodynamic properties of air with temperature are listed in Table C1. Thermodynamic properties of the gas (i.e., air-vapor) mixture are calculated by using the appropriate mixing rules of Reid *et al* (1977). However, gas mixture's viscosity is calculated by using Wilke's kinetic theory for gases (Reid *et al*, 1977), i.e.,

$$\mu_m = \sum_{i=1}^{n} \frac{y_i \mu_i}{\sum_{j=1}^{n} y_i \Xi_{ij}}, \quad \text{(C19)}$$

where Θ_{ij}

$$\Xi_{ij} = \frac{\left[1 + (\mu_i/\mu_j)^{1/2}(M_j/M_i)^{1/4}\right]^2}{\left[8(1 + M_i/M_j)\right]^{1/2}}, \quad \text{(C20)}$$

$$\Xi_{ji} = \frac{\mu_j}{\mu_i}\frac{M_i}{M_j}\Xi_{ij}, \quad \text{(C21)}$$

$$\Xi_{ii} = \Xi_{jj} = 1 \quad \text{(C22)}$$

These relations can also be used to calculate the mixture thermal conductivity by replacing μ by λ. Whereas, the gas mixture's density and specific heat are calculated by using the mole and mass fractions, respectively, as

$$\rho_m = Y_F \rho_v + (1 - Y_F)\rho_a , \tag{C23}$$

$$c_{pm} = X_F c_{pv} + (1 - X_F)c_{pa} \tag{C24}$$

Table C.1 Air properties at different temperatures

T (K)	ρ (kg/m^3)	c_p (J/kgK)	λ (W/mK)	μ (Pas)
100	3530488	10266	0009246	692E-06
150	2353659	10099	0013735	103E-05
200	1765244	10061	0018090	133E-05
250	1412195	10053	0022270	149E-05
300	1176829	10057	0026240	198E-05
350	1008711	10090	0030030	208E-05
400	0882622	10140	0033650	229E-05
450	0784553	10207	0037070	248E-05
500	0706098	10295	0040380	267E-05
550	0641907	10392	0043600	285E-05
600	0588415	10551	0046590	302E-05
650	0543152	10635	0049530	318E-05
700	0504355	10752	0052300	333E-05
750	0470732	10856	0055090	348E-05
800	0441311	10978	0057790	363E-05
850	0415352	11095	0060280	377E-05
900	0392276	11212	0062790	390E-05
950	0371630	11321	0065250	402E-05
1000	0353049	11417	0067520	415E-05
1100	0320953	11600	0073200	444E-05
1200	0294207	11790	0078200	469E-05
1300	0271576	11970	0083700	493E-05
1400	0252178	12140	0089100	517E-05
1500	0235366	12300	0094600	540E-05
1600	0220655	12480	0100000	563E-05
1700	0207676	12670	0105000	585E-05
1800	0196138	12870	0111000	607E-05
1900	0185815	13090	0117000	629E-05
2000	0176524	13380	0124000	650E-05
2100	0168118	13720	0131000	672E-05
2200	0160477	14190	0139000	693E-05
2300	0153499	14820	0149000	714E-05
2400	0147104	15740	0161000	735E-05
2500	0141220	16880	0175000	757E-05

Appendix D

CALCULATION OF DROPLET'S VOLUME AND SURFACE AREA BY USING BLOCKED-OFF TECHNIQUE

The blocked-off technique approximates the actual droplet surface as a stair step shape. This approximation makes the calculation of the droplet's surface area not straightforward and requires more attention. This appendix details the methodology used to calculate the volume and the surface area of the droplet generated by the blocked-off technique.

As shown in Figure D.1, according to the blocked-off technique the droplet can be divided into a number of *x-z* planes where each plane has a specified number of control volumes. The number of these planes and their corresponding control volumes depend on the chosen grid. According to the chosen grid in this study, the droplet is made up of twenty *x-z* planes (see Figure D.1). The control volumes of each plane can be viewed through a *x-y* projection, as shown in Figure D.2.

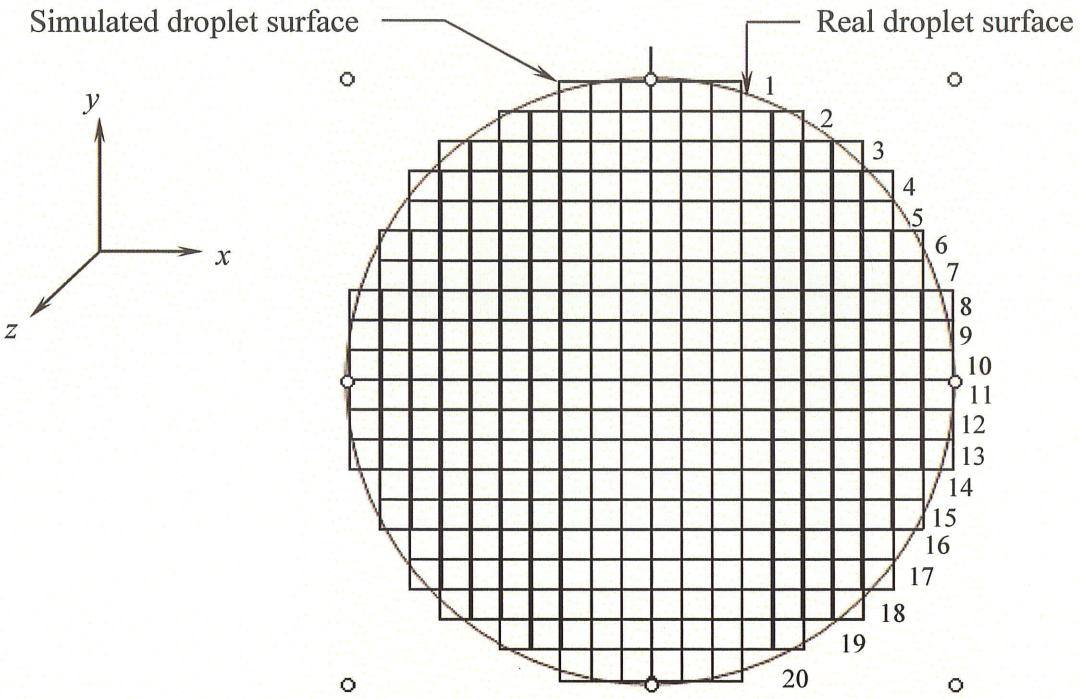

Figure D.1 Simulated and real droplet surface as seen from top view (i.e., *x*-*z* planes)

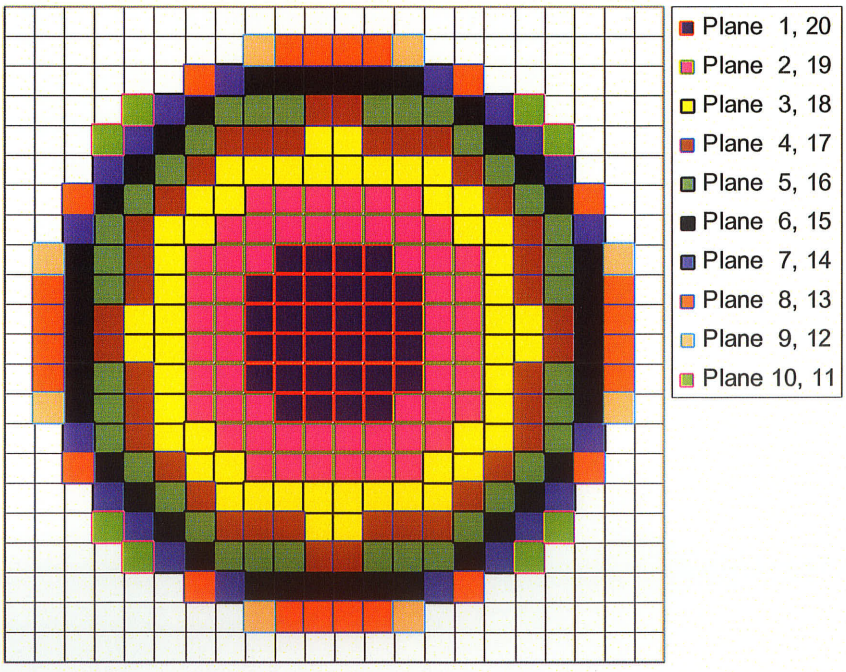

Figure D.2 Front view of the simulated droplet (i.e., *x*-*y* planes)

Figure D.3 shows the front view (x-y projection) for each plane separately. This projection enables figuring out the number of control volumes and surface areas subjected to the flow and hence susceptible to evaporate. For each plane, the number of control volumes and surface areas are listed in Table D.1. This table shows the number of control volumes for each plane and, the total number of the control volumes over all the planes (4224 control volumes) determines the approximated droplet volume. The 4224 control volumes have a total of 25344 surfaces/faces (each control volume has 6 surfaces) but only 1464 surfaces are exposed to the flow and eventually represent the outer surface of the droplet. For example, plane 2 has a total of 88 control volumes (528 surfaces) where 32 control volumes are blocked by plane 1 and the other 56 control volumes are called either interior or exterior. Each one of the interior control volumes has only 1 surface exposed to the flow, whereas each one of the exterior control volumes might have 2 surfaces (if it is not an edge control volume) or 3 surfaces (if it is an edge control volume). In conclusion, the number of surfaces for each plane can be calculated as $N_{surfaces} = n_{inerior} + 2n_{exterior} + n_{edges}$

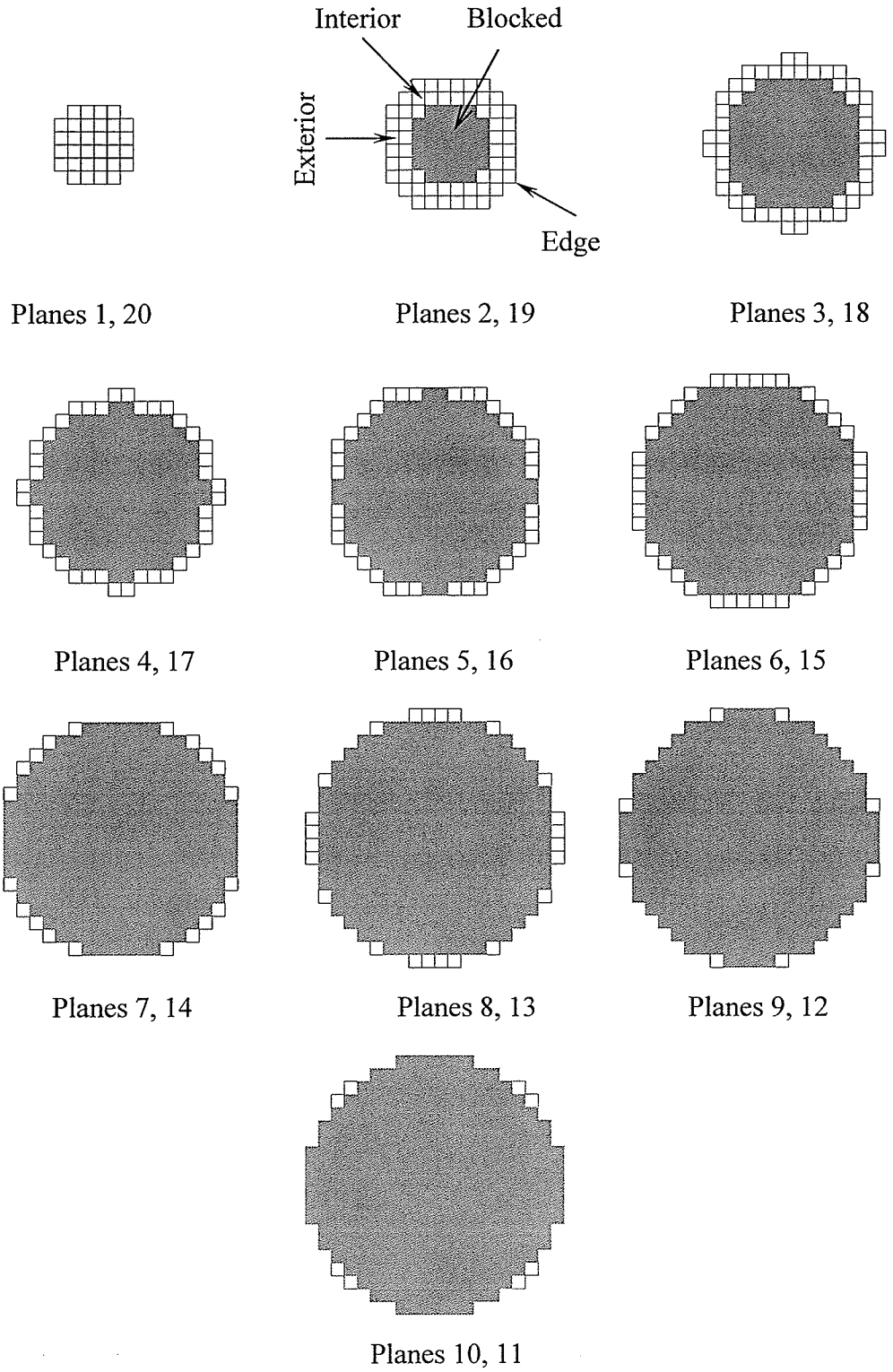

Figure D.3 Control volumes and their corresponding surfaces for each plane of the droplet

Table D.1 Blocked-off technique based calculation of the control volumes and surfaces for each plane of the droplet

	Number of volumes	Surface area				
Plan no.	Total CV's	Blocked CV's	Interior CV's	Exterior CV's	Edges	Total surface areas
1	32	0	16	16	8	56
2	88	32	28	28	12	96
3	140	88	16	36	20	108
4	180	140	0	40	24	104
5	216	180	0	36	20	92
6	256	216	0	40	24	104
7	276	256	0	20	20	60
8	300	276	0	24	16	64
9	308	300	0	8	8	24
10	316	308	0	8	8	24
11	316	316	0	8	8	24
12	308	300	0	8	8	24
13	300	276	0	24	16	64
14	276	256	0	20	20	60
15	256	216	0	40	24	104
16	216	180	0	36	20	92
17	180	140	0	40	24	104
18	140	88	16	36	20	108
19	88	32	28	28	12	96
20	32	0	16	16	8	56
	Total CV= 4224	3600	120	512	320	Total surfaces=1464

Appendix E

EVAPORATION RATE OF *n*-HEPTANE AND *n*-DECANE DROPLETS

This appendix tabulates the evaporation rates of *n*-heptane and *n*-decane droplets under stagnant, laminar and turbulent airstream conditions. These data cover a wide range of flow cnditions. The freestrean (airstream) mean temperature ranges between 300K and 1273K; the freestream mean velocity ranges between 0.6 m/s and 2 m/s and the freestrean turbulence intensity varies between 0% and 60%. Note that the droplet evaporation rate is calculated from the time-history of the normalized steady-state region of the droplet diameter.